Weld Propagation in Ultrasonic Welding of Multi-Layered Dissimilar Metal Sheets

by

Ying Luo

A dissertation proposal submitted in partial fulfillment
of the requirements for the degree of
Doctor of Philosophy
(Mechanical Engineering)
in the University of Michigan
2020

Doctoral Committee:

Professor S. Jack Hu, Co-Chair
Professor Elijah Kannatey-Asibu Jr., Co-Chair
Professor Pingsha Dong
Research Associate Professor Theodor Freiheit
Dr. Teresa Rinker, General Motors

Ying Luo

ylyluo@umich.edu

ORCID ID: 0000-0001-7662-9903

Acknowledgements

I am honored and humbled to have the opportunity to express my sincere gratitude to those who have made this dissertation possible.

First and foremost, my deepest gratitude goes to my advisors, Prof. S. Jack Hu and Prof. Elijah Kannatey-Asibu Jr. for their persistent help and guidance throughout my graduate study. Prof. Hu shared with me his brilliant insight and great vision and Prof. Asibu shared with me his vast knowledge and experience on my research. This work would never have been accomplished without them.

I also deeply appreciate the precious time that Prof. Pingsha Dong, Dr. Theodor Freiheit, and Dr. Teresa Rinker have devoted to serving on my dissertation committee. Their insightful advice has significantly improved the work presented in this dissertation.

I gratefully acknowledge General Motors for the financial and technical support that allowed me to do this work. I particularly want to thank Dr. Wayne Cai, and Dr. Teresa Rinker for their support, guidance, and invaluable comments during my study. Special thanks to Dr. Jeffrey Abell for his invaluable advice on this research.

I would like to thank Dr. Theodor Freiheit for his valuable suggestions and support on my research. I am grateful to Dr. Haseung Chung for his advice and assistance on the difficulties I encountered during my research. I would also like to express my gratitude to Dr. Mihaela Banu for her kind support.

I thank all the Hu Lab members and colleagues that I have worked with for their unconditional support. It has been a great pleasure to work with them. I would also like to thank all my friends at University of Michigan. Their friendship has made my life in Ann Arbor meaningful and blissful.

Finally and most importantly, I would like to thank my family. Their endless love and support gave me confidence to face challenge over the years.

Table of Contents

Acknowledgements ii

List of Figures vii

List of Tables xi

Abstract xii

Chapter 1 Introduction 1

1.1. Background and Motivation 1

1.2. Summary of Literature Review 5

1.3. Research Objectives 6

1.4. Organization of Dissertation 7

References 10

Chapter 2 Literature Review 12

2.1. Ultrasonic Welding Machine and Process 12

2.2. Weld Quality Evaluation and Characterization 13

2.3. Process Parameters 15

2.4. Process Robustness 17

2.5. Bonding Mechanisms 17

2.6. Weld Formation 21

2.7. Mechanical and thermal fundamentals 23

2.8. Multi-layered USW 25

2.9. Summary 26

References 27

Chapter 3 Weld Formation in Multi-Layered Ultrasonic Welding of Similar and Dissimilar Materials 33

3.1. Introduction 34

3.2. Materials and Experimental Setup 36

3.3. Bonding Mechanisms and Weld Formation 41

3.4. Influence of Process Parameters 58

3.5. Conclusions 64

References 66

Chapter 4 Influence of Interfacial Undulations on Weld Formation and Performance 68

4.1. Introduction 69

4.2. Experimental Setup 73

4.3. Comparison of Lap-Shear Performance and Weld Attributes 76

4.4. Finite Element Simulation of Lap-Shear Test 90

4.5. Conclusions 108

References 110

Chapter 5 Enhancement of Process Robustness in Multi-Layered Ultrasonic Welding by Localized Pre-Heating 113

5.1. Introduction 114

5.2. Experimental Study 117

5.3. Finite Element Model 122

5.4. Simulation Results 132

5.5. Conclusion 137

References 139

Chapter 6 Conclusions and Future Work 142

6.1. Conclusions 142

6.2. Future Work 146

List of Figures

Figure 1.1. Lithium-ion battery assemblies in EVs 2

Figure 1.2. Illustration of USW process 4

Figure 2.1. Schematic of a metal ultrasonic welding machine 13

Figure 2.2. Mechanical test method for weld strength measurement 14

Figure 2.3. Weldability lobe with corresponding weld strengths and failure modes 16

Figure 3.1. Experimental setup showing (a) metal USW machine, (b) sonotrode tip and anvil, and (c) side and top views of the multi-layered USW configuration. 38

Figure 3.2. Lap-shear test..... 41

Figure 3.3. Optical microscopic images of samples welded at cross-section A-A at (1) 1200 J, (b) 1400 J, (c) 1600 J, (d) 1800 J, (e) 2000 J, and (f) 2400 J 42

Figure 3.4. Crest region of sample welded at 1600 J..... 43

Figure 3.5. Detailed OM images of crest region in welds made at (a) 600 J, (b) 1200 J, (c) 1200 J with higher magnification, (d) 1400 J, (e) 1800 J, and (f) 2400 J, and OM image of valley in weld made at 2400 J. 45

Figure 3.6. Lap-shear results vs. weld energy for the top and bottom interfaces of 3CC 48

Figure 3.7. Optical microscopic images of samples welded at cross-section A-A..... 50

Figure 3.8. OM images with higher magnification (a) at valley of 164 J sample, (b) crest of 164 J sample, and (c) crest of 836 J sample. 51
Figure 3.9. Grain structure analysis at valley and crest area for samples welded at 164 J and 836 J 53
Figure 3.10. EDX analysis at Al/Cu interface in sample welded at 836 J 55
Figure 3.11. Lap-shear performance results: (a) weld strength vs. weld energy for all interfaces of 3AC, (b) 4 different failure modes. 57
Figure 3.12. Influence of clamping pressure (a) 17 psi, (b) 25 psi, (c) 33 psi, and (d) maximum lap-shear force at different interfaces change with clamping pressure 59
Figure 3.13. Influence of vibration amplitude (a) 32 µm, (b) 40 µm, (c) 48 µm, and (d) maximum lap-shear force at different interfaces change with vibration amplitude 60
Figure 3.14 Main effects plot for weld energy, vibration amplitude, and clamping pressure at (a) the top, (b) the middle, and (c) the bottom interface 63
Figure 4.1 Experimental setup for USW (a) apparatus, and (b) top view of weld configuration schematic 74
Figure 4.2. Tool knurl patterns and dimensions 75
Figure 4.3. Apparatus of lap-shear test: (a) side view, and (b) front view. 76
Figure 4.4 Lap-shear performance. 78
Figure 4.5. Images of sample produced at 500 J using fine anvil 79
Figure 4.6. Schematic diagram of ultrasonic weld at cross-section A-A 80

Figure 4.7. Cross-sectional micrographs of samples made by fine and coarse anvil at 100 J, 500 J and 900 J. 82
Figure 4.8. Fracture surface of samples made by different anvils at different weld energy..... 83
Figure 4.9. Comparison of (a) bond density and (b) post-weld thickness. 84
Figure 4.10. Change of interfacial undulations in samples made at different weld energy using the fine and coarse anvil 86
Figure 4.11. Hardness evaluation of welds for different weld energies and anvils 88
Figure 4.12. Flow chart of the FEM study..... 91
Figure 4.12. FEM for the lap-shear test 93
Figure 4.16. Predicted versus experimental dependencies of bonding strength factor..... 101
Figure 4.17. Comparison of experimental and simulation results in peak lap-shear load for (a) fine anvil and (d) coarse anvil, and load-displacement curve for (b) 200 J with fine anvil, (c) 700 J with fine anvil, (e) 200 J with coarse anvil, and (f) 700 J with coarse anvil 103
Figure 4.18. Comparison of peak lap-shear load between flat and undulated interface..... 104
Figure 4.19. Load-displacement curve for (a) 100 J with interfacial failure, (b) 900 J with circumferential failure..... 105
Figure 4.20. Mechanical behavior evolution at the bonding layer for the cases with interfacial separation 106
Figure 4.21. Equivalent Von Mises stress distribution at the center of the bonding layer for flat and undulated interface with 0.2 mm pull-point displacement..... 107

Figure 4.22. Stress distribution in the weld area in cases with base material failure for (a) undulated interface and (b) flat interface 108
Figure 5.1. USW system setup for preheating showing (a) top view and (b) side view 118
Figure 5.2. Lap-shear results for preheated and non-preheated samples at: (a) bottom interface and (b) top interface 120
Figure 5.3. Microstructural analysis of samples under both ambient and preheated conditions with (a) 1200 J, (b) 1600 J, and (c) 2000 J 121
Figure 5.4. Geometry and mesh of the finite element model 123
Figure 5.5. Schematics showing the effect of strain hardening on the yield locus 127
Figure 5.6. Temperature dependent mechanical properties of Cu 129
Figure 5.7. temperature distribution in the workpieces for different bus-bar initial temperatures: (a) ambient condition, (b) 50 ºC, (c) 100 ºC, and (d) 150 ºC. 133
Figure 5.8. Horizontal displacement of workpieces during ramp up period for (a) ambient condition, (b) 50 ºC, (c) 100 ºC, and (d) 150 ºC. 134
Figure 5.9. Equivalent plastic strain distribution for (a) ambient condition, (b) 50 ºC, (c) 100 ºC, and (d) 150 ºC. 135
Figure 5.10. Maximum principal strain distribution for (a) ambient condition, (b) 50 ºC, (c) 100 ºC, and (d) 150 ºC. 136

List of Tables

Table 1.1 Summary of Different Welding Technologies in Battery Manufacturing 3

Table 3.1 Mechanical Properties of the Metal Sheets 37

Table 3.2 Experimental Design Matrix 39

Table 3.3 Response Surface Analysis of Weld Strength vs. Process Parameters 62

Table 4.1 Welding Factors and Levels 74

Figure 4.13. Stress-strain curves of (a) Al and Cu, and (b) schematic representative uniaxial progress damage model [31]. 95

Table 4.2 General Material Properties of Al and Cu 96

Figure 4.14. Comparison of load-displacement curve for experimental and simulation results for fine anvil at (a) 100 J, (b) 300 J, (c) 500 J, and (d) 900 J. 99

Figure 4.15. Comparison of load-displacement curve for experimental and simulation results for coarse anvil at (a) 100 J, (b) 300 J, (c) 500 J, and (d) 900 J. 100

Table 5.1 Material Properties of Steel and Cu[14] 125

Table 5.2 Constants in Eqns. 5.4 to 5.8 128

Abstract

Growing concerns over the environmental impact of carbon emissions have led to increased interest in electric vehicles (EVs) and hybrid electric vehicles. A reliable and efficient battery system is the key technological element to the development of practical EVs. In a typical EV battery pack, a large number of battery cells are assembled together to provide sufficient voltage and energy capacity to the vehicle. The battery assembly requires good quality joints to ensure system reliability. The challenge in battery joining for EVs is that joints involve multi-layered thin metal sheets of similar and dissimilar materials that have high thermal and electrical conductivity, such as Al and Cu. Ultrasonic welding (USW), as a solid-state process, is a promising method to efficiently produce good-quality welds in battery assembly. However, the process parameter window for making joints in multi-layered USW is narrow and the identification of the parameter window has been based on trial-and-error methods. In addition, it is difficult to make consistent weld quality at different interfaces in the multi-layered joint.

To improve process robustness and the efficiency of process development, a deeper understanding of the underlying physics of USW and advanced techniques for improving the weldability need to be developed. In this dissertation, three topics are addressed:

1. *Understanding weld formation in multi-layered similar and dissimilar metal sheets*: The weld formation mechanisms of two frequently used weld configurations in battery assembly were experimentally studied. The two configurations were 3 layered thin Ni-coated Cu tabs to 1 thick Ni-coated Cu bus bar (3CC) and 3 layered thin Al tabs to 1

thick bare Cu bus bar (3AC). By tracking the evolution of microstructures and the corresponding weld quality subjected to the weld energy, the dominant bonding mechanism for similar material is found to be metallic adhesion accompanied with dynamic recrystallization and interfacial undulations, while the bonding between dissimilar materials is shown to be driven by diffusion. The phenomenological observations also imply parametric dependent weld formation in multi-layered USW.

2. *Influence of interfacial undulations on weld formation and performance*: The influence of interfacial undulations on weld formation were experimentally studied using two anvils with different knurl shapes. Several key weld attributes related to the weld formation were characterized and compared by cross-sectioned weld samples using microscopy. Finite element models were developed to predict the mechanical behavior of samples with different bonding strength and undulation degrees in lap-shear test. The empirical results reveal that interfacial undulations retard the formation of the weld and prevent excessive thinning of the workpiece. Meanwhile, numerical study helps provide insight on influence of interfacial undulations on weld performance with same bonding strength and possible influence on multi-layered USW.
3. *Weld robustness enhancement by preheating*: Localized preheating was investigated as an approach to enhance the weldability in multi-layered USW of four layered Ni-coated Cu. The influence of preheating temperature on mechanical performance of samples welded at different weld energy was investigated. The process robustness is found to be enhanced by increasing weld strength at the preheated interface while keeping performance at the non-preheated interface insignificantly affected. 2D finite element

process models were built to understand thermal-mechanical behavior under different thermal conditions.

This dissertation provides in-depth understanding of joint formation and propagation in multi-layered ultrasonic welding in battery pack manufacturing and develops a practical means to enhance process robustness through pre-heating.

Chapter 1 Introduction

1.1. Background and Motivation

Increasing concerns over the environmental impact of carbon emissions are driving the automotive industry toward more fuel efficient vehicles. Electric vehicles (EVs) use batteries as a major component in the power system, including battery electric vehicles (BEVs) and hybrid electric vehicles (HEVs). EVs are considered a promising solution for the reduction of carbon emissions from transportation systems.

More EVs today are utilizing lithium-ion batteries because of their high power and energy density compared to other types of battery [1-3]. The working voltage of one lithium-ion battery cell is about 4 volts [4], thus a large number of battery cells are connected to ensure the voltage and energy capacity of EVs. As illustrated in Figure 1.1, multiple battery cells are joined together via electrode tabs and those joined cells are connected by a metal bus-bar to form a battery module. Multiple modules are then assembled together to form a battery pack for an EV. Typically, batteries in EVs are exposed to harsh driving environment with vibration, varying load conditions, and severe temperatures [1]. Therefore, it is essential to create reliable connections between battery cells, modules, and battery packs, as well as control units. A reliable connection means quality joints with enough mechanical strength, low electrical resistance, good fatigue behavior, and strong corrosion resistance. Moreover, since multiple similar and dissimilar metal sheets are joined simultaneously in manufacturing the battery packs, uniform and predictable joint quality for all connections is crucial.

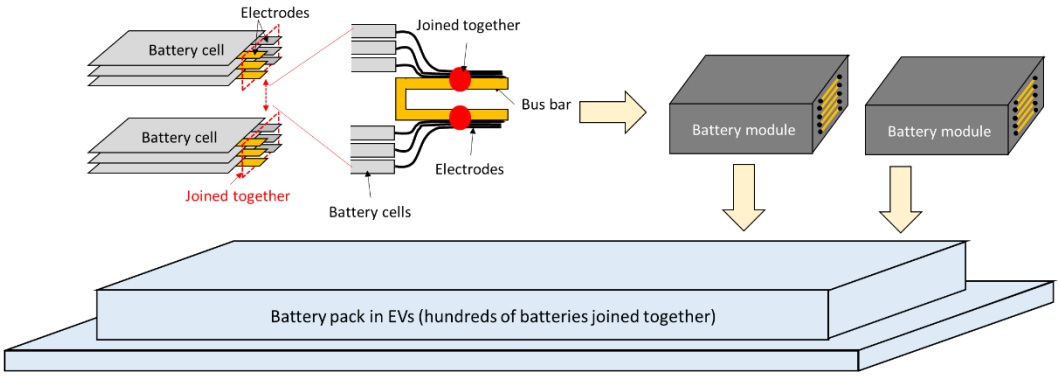

Figure 1.1. Lithium-ion battery assemblies in EVs.

Aluminum (Al) and copper (Cu) sheets are widely used as the lithium-ion battery tabs and bus-bars due to their low electrical resistance, high electrical and thermal conductivities, and relatively attractive prices [5]. The joining of Al and Cu is challenging using traditional fusion welding technologies. Table 1 summarizes the advantages and disadvantages of frequently used welding methods in battery manufacturing [5, 7]. Resistance welding is a thermo-electric process that relies on the interfacial electrical resistance to generate localized heating and subsequent fusion of materials [8]. The high conductivities of Al and Cu makes it difficult to weld using this method. Laser welding, a non-contact process using an intense laser beam, has the advantage of rapidly and precisely heating and melting materials and can be used to weld multiple metal pieces in a very short time. However, the low laser energy absorptivity and high thermal conductivity of Al and Cu negatively impact process efficiency [9]. In addition, porosity, spattering, and brittle intermetallic compounds (IMCs) caused by large misalignment in physical properties and poor metallurgical affinity between dissimilar materials are still significant obstacles in the use of these two fusion welding methods in manufacturing battery packs. In comparison, ultrasonic welding (USW) has several inherent advantages as a solid-state process for welding thin metal sheets with

high electrical and thermal conductivities regardless of the physical and metallurgical property difference. As summarized in Table 1.1, USW is a promising method for joining lithium-ion batteries.

Table 1.1 Summary of Different Welding Technologies in Battery Manufacturing

Welding Method	Advantages	Disadvantages
Ultrasonic welding	• Minimum IMCs • Small heat-affected zone • Suitable for highly conductive materials • Suitable for thin sheets and multi-layered workpieces • Relative low cost	• Possible severe tool perforation • Possible structural vibration • Upper limit in total joint thickness • Difficult for joining hard materials • Double-sided machine makes the equipment design more complex
Resistance welding	• Relative mature technology with established weld quality monitoring methods • Low cost	• Large heat-affected zone • Large amount of IMCs • Difficult for highly conductive materials • Difficult for multi-layered workpieces
Laser welding	• Relatively small heat-affected zone • Single-sided • High throughput	• IMCs for dissimilar materials • Porosity and hot-cracking • High fit-up requirement • High initial cost

Ultrasonic welding (USW) was first introduced in the 1950s and has widespread applications in electrical and electronic connections in industries including electrical, automotive, medical, and aerospace industries [11-12]. During the process, high-frequency oscillations are locally applied to overlapped workpieces clamped together under pressure. The synergy of vibration and pressure produces relative motion at the faying surfaces, removes surface contaminants and oxide layers, leading to intimate metal-to-metal contact. As a result, solid-state bonds form at the interface, as illustrated in Fig. 1.2 [13, 15-16]. The entire area under the electrode

(sonotrode) tip is welded when sufficient welding time, or alternatively, sufficient welding energy is applied. The welding time is typically less than 2 seconds and welding energy is also relatively low [14]. The key process parameters are clamping pressure over the workpiece, vibration amplitude, and welding input energy [5, 14, 16].

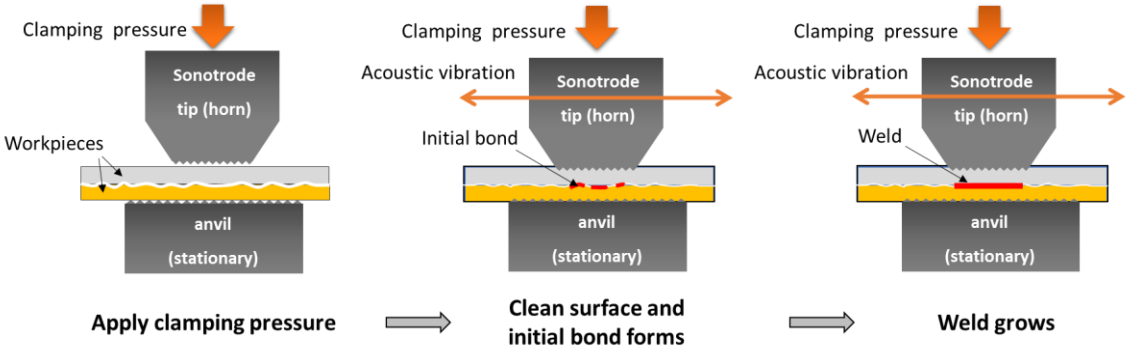

Figure 1.2. Illustration of USW process (adopted from [14]).

While USW is suitable for battery welding, several critical problems still need to be addressed. As mentioned in Table 1.1, USW has an upper limit in total joint thickness, and may introduce severe perforation or fracture at workpiece surfaces that directly contact the weld tool. Moreover, it is difficult for USW to produce consistent weld quality at different interfaces in a multi-layered joint [7,8]. To overcome these challenges and produce good quality joints for multi-layered USW, defining a proper process window, ensuring process robustness, and appropriate weld tools are indispensable. However, the current method for finding the proper process settings is based on trial-and-error, which is both time consuming and expensive. To reduce the process development time and improve process robustness, a deeper understanding of the underlying physics of multi-layered USW and more advanced techniques need to be developed.

1.2. Summary of Literature Review

Numerous studies have been performed on the USW process in past decades. This section provides a summary of the state of the art and the detailed literature review will be presented in Chapter 2.

Weld quality is an important topic of any welding technique. The weld quality of USW is evaluated by mechanical tests and characterized by corresponding weld attributes [7]. Past research has classified the weld quality of USW into three major categories, a cold weld with insufficient weld strength, a good weld with satisfactory weld performance, and an over weld with excessive thinning of the workpieces [14]. The weld attributes such as bond density and post-weld thickness have been investigated and related to different weld qualities [7].

The process robustness including process parameter optimization, tool design, and enhancement by assistant technologies have also been discussed in the literature. Statistical methods have been applied to analyze the effect of different process parameters on weld quality [7, 16][7]. Tool design and material treatment have been investigated through experiments and numerical simulation [17-18]. Process enhancements by changing the vibration path and applying additional thermal assistance have been proposed by different researchers.

The underlying physics of USW has been thoroughly investigated. Four different bonding mechanism including local melting [19], interface diffusion [20], mechanical interlocking [13], and metallurgical adhesion [7] have been proposed. Supporting theories such as dynamic recrystallization [21] and formation of intermetallic compounds (IMCs) have also been discussed [22]. The coupled thermal-mechanical behavior within the workpieces during the process have been studied by numerical methods as well [24].

In recent years, the increasing market for EVs has stimulated demand for battery manufacturing and technologies. Interest in multi-layered USW has been growing. The big challenges in multi-layered USW include inconsistent weld quality at different interfaces and narrow process window. Studies focusing on the process robustness, bonding mechanism, and weld propagation are discussed by some researchers [16].

Though USW has been studied for years, exploring the underlying physics is still important, as new requirements such as new material combinations and new weld configurations emerge to satisfy new market demands. Moreover, the research on multi-layer USW is still at an early stage, and no scientific guidance has been generated for the process robustness.

1.3. Research Objectives

The objective of this research is to investigate the underlying physics of weld formation at individual interfaces and from interface to interface, establishing in-depth understanding of the relation between weld attributes and weld quality, and providing guidance on process parameter selections, tool optimization, and process robustness enhancement. The specific tasks are:

1) To investigate bonding mechanism and weld formation in multi-layered USW for similar and dissimilar metal sheets that are frequently used in lithium-ion battery pack manufacturing.
2) To investigate the influence of interfacial undulations on weld formation by characterizing the weld attributes through cross-sectioned samples welded using different anvils and evaluating the contribution of bonding strength and interfacial undulations on lap-shear performance.

3) To investigate the influence of localized preheating on weld formation and its feasibility on weldability enhancement of multi-layered USW by analyzing different welds made under varying preheating temperatures.

The research is performed based on two hypotheses. The first hypothesis is that all USW processes, regardless of number of stack-up layers, share similar solid-state bonding mechanisms if the local conditions, such as material combination and interfacial thermal-mechanical behaviors, are the same, and knowledge in two-layered USW can be adopted and extrapolated to the study of multi-layered USW. The other hypothesis is that bonds at different interfaces in multi-layered USW form in sequence that is governed by thermodynamics and thermal-mechanical behavior at the interface. Such weld propagation can be estimated by weld attributes as well as weld quality and can be modified by process settings. The fulfillment of the above objectives will verify the hypotheses and help develop an in-depth understanding of the bonding mechanisms and weld propagation in ultrasonic welding of multi-layered thin metal sheets. The results in this dissertation will also present the effects of process variables on the weld formation and weld quality. Moreover, the findings will provide a more scientific guide for process robustness improvement.

1.4. Organization of Dissertation

The rest of this dissertation is organized as follows:

Chapter 2 systematically reviews the state of the art of metal ultrasonic welding process. First, weld quality evaluation and associated weld attribute characterization is presented. Then, the effect of process variables on weld quality is discussed, followed by studies of process robustness. The underlying physics of the process, including bonding mechanisms and thermal-mechanical

behavior analysis are also reviewed. Some studies in multi-layered USW in recent years are also summarized.

Chapter 3 investigates the bonding mechanisms and weld formation in two frequently used weld configurations in lithium-ion battery pack manufacturing, namely joining 3-layers of thin Ni-coated Cu tabs to one thick Ni-coated Cu bus bar (3CC) and joining 3-layers of thin Al tabs to one thick bare Cu bus bar (3AC). Microscopy was used to examine the cross-sectioned samples produced over a range of weld energies, including optical microscope (OM) and scanning electron microscope (SEM), energy-dispersive X-ray spectroscopy (EDX), and electron backscatter diffraction (EBSD). The evolution of the interfacial bonding and metallurgical features were correlated to weld lap-shear performance to identify different stages of the weld formation. Design of experiment (DOE) and analysis of variance (ANOVA) were applied to investigate the parametric influence on weld formation and associated weld quality.

Chapter 4 discusses the effect of interfacial undulations on weld formation and lap-shear performance by using two anvils with different shapes. The undulations generated due to the two tool geometries were characterized by undulation size and amplitude. Several key weld attributes, including bond density and post-weld thickness were also compared under a series of weld energies. Finite element models were built based on the information of undulation and weld attributes to simulate and predict the lap-shear performance under different undulation and bonding conditions. The impact of the degree of undulation and the bonding condition contribution to interfacial undulations on the lap-shear behavior was analyzed. An insight of tool geometry design guide was summarized in terms of lap-shear performance with various interfacial undulations.

Chapter 5 proposes localized preheating of the thick bus-bar side as a method to enhance the weldability of multi-layered USW in battery pack manufacturing. Welds joining 3-layers of thin Ni-coated Cu tabs to one thick Ni-coated Cu bus bar (3CC) were used to investigate the influence of preheating temperature on weld performance at different weld stages. The evolution of the microstructure and bonding conditions under the effect of preheating were studied. Temperature and stress-strain history during the process under both ambient and preheated conditions were also analyzed using simplified 2D thermo-mechanical simulations.

Chapter 6 summarizes the findings and expected contributions of this dissertation and proposes future work.

References

[1] Andrea, D., 2010. Battery management systems for large lithium ion battery packs. Artech house.

[2] Armand, M. and Tarascon, J.M., 2008. Building better batteries. Nature, 451(7179), p.652.

[3] Lu, L., Han, X., Li, J., Hua, J. and Ouyang, M., 2013. A review on the key issues for lithium-ion battery management in electric vehicles. Journal of Power Sources, 226, pp.272-288.

[4] Goodenough, J.B. and Park, K.S., 2013. The Li-ion rechargeable battery: a perspective. Journal of the American Chemical Society, 135(4), pp.1167-1176.

[5] Lee, S.S., Kim, T.H., Hu, S.J., Cai, W.W. and Abell, J.A., 2010, January. Joining technologies for automotive lithium-ion battery manufacturing: A review. In ASME 2010 international manufacturing science and engineering conference (pp. 541-549). American Society of Mechanical Engineers.

[6] Cai, W., Daehn, G., Vivek, A., Li, J., Khan, H., Mishra, R.S. and Komarasamy, M., 2019. A state-of-the-art review on solid-state metal joining. Journal of Manufacturing Science and Engineering, 141(3), p.031012.

[7] Lee, S.S., Kim, T.H., Hu, S.J., Cai, W.W., Abell, J.A. and Li, J., 2013. Characterization of joint quality in ultrasonic welding of battery tabs. Journal of Manufacturing Science and Engineering, 135(2), p.021004.

[8] Zhang, H., and Senkara J., 2011. Resistance welding: fundamentals and applications. CRC press.

[9] Auwal, S.T., Ramesh, S., Yusof, F. and Manladan, S.M., 2018. A review on laser beam welding of copper alloys. The International Journal of Advanced Manufacturing Technology, 96(1-4), pp.475-490.

[10] Wu, X., Liu, T. and Cai, W., 2015. Microstructure, welding mechanism, and failure of Al/Cu ultrasonic welds. Journal of Manufacturing Processes, 20, pp.321-331.

[11] De Vries, E., 2004. Mechanics and mechanisms of ultrasonic metal welding (Doctoral dissertation, The Ohio State University).

[12] Graff, K., 2005. Ultrasonic metal welding. In New developments in advanced welding (pp. 241-269). Woodhead Publishing.

[13] Bakavos, D. and Prangnell, P.B., 2010. Mechanisms of joint and microstructure formation in high power ultrasonic spot welding 6111 aluminium automotive sheet. Materials Science and Engineering: A, 527(23), pp.6320-6334.

[14] Kim, T.H., Yum, J., Hu, S.J., Spicer, J.P. and Abell, J.A., 2011. Process robustness of single lap ultrasonic welding of thin, dissimilar materials. CIRP annals, 60(1), pp.17-20.

[15] Patel, V.K., Bhole, S.D. and Chen, D.L., 2012. Microstructure and mechanical properties of dissimilar welded Mg–Al joints by ultrasonic spot welding technique. Science and Technology of Welding and Joining, 17(3), pp.202-206.

[16] Das, A., Li, D., Williams, D. and Greenwood, D., 2019. Weldability and shear strength feasibility study for automotive electric vehicle battery tab interconnects. Journal of the Brazilian Society of Mechanical Sciences and Engineering, 41(1), p.54.

[17] Lee, D. and Cai, W., 2017. The effect of horn knurl geometry on battery tab ultrasonic welding quality: 2D finite element simulations. Journal of Manufacturing Processes, 28, pp.428-441.

[18] Li, H., Cao, B., Yang, J.W. and Liu, J., 2018. Modeling of resistance heat assisted ultrasonic welding of Cu-Al joint. Journal of Materials Processing Technology, 256, pp.121-130.

[19] Kreye, H., 1977. Melting phenomena in solid state welding processes. Weld. J, 56(5), pp.154-158.

[20] Li, J., Han, L. and Zhong, J., 2008. Short‐circuit diffusion of ultrasonic bonding interfaces in microelectronic packaging. Surface and Interface Analysis: An International Journal devoted to the development and application of techniques for the analysis of surfaces, interfaces and thin films, 40(5), pp.953-957.

[21] Lu, Y., Song, H., Taber, G.A., Foster, D.R., Daehn, G.S. and Zhang, W., 2016. In-situ measurement of relative motion during ultrasonic spot welding of aluminum alloy using Photonic Doppler Velocimetry. Journal of Materials Processing Technology, 231, pp.431-440.

[22] Yang, J. and Cao, B., 2015. Investigation of resistance heat assisted ultrasonic welding of 6061 aluminum alloys to pure copper. Materials & Design, 74, pp.19-24.

[23] Lu, Y., Song, H., Taber, G.A., Foster, D.R., Daehn, G.S. and Zhang, W., 2016. In-situ measurement of relative motion during ultrasonic spot welding of aluminum alloy using Photonic Doppler Velocimetry. Journal of Materials Processing Technology, 231, pp.431-440.

[24] Li, H., Cao, B., Liu, J. and Yang, J., 2018. Modeling of high-power ultrasonic welding of Cu/Al joint. The International Journal of Advanced Manufacturing Technology, 97(1-4), pp.833-844.

Chapter 2 Literature Review

This chapter provides a review of the state of the art of the ultrasonic welding (USW) process and relevant research literature. In the past decades, extensive studies have been performed on the USW process to evaluate weld attributes and quality, investigate the influence of process parameters on weld quality, improve process robustness, and reveal the underlying physics including bonding mechanisms and thermo-mechanical fundamentals. Multi-layered USW is attracting more attention in recent years because of the increasing demands for EV batteries.

2.1. Ultrasonic Welding Machine and Process

Ultrasonic welding creates joints using high frequency vibration (e.g. 20 kHz). A USW machine consists of the controller, transducer, booster, sonotrode, and set of components. A schematic showing the configuration of a USW machine is shown in Fig. 2.1. During the welding process, a set of piezoelectric disks monitored by the controller generates longitudinal vibrations. The vibration is amplified through the booster system and transfers to the sonotrode and the horn tip. A clamping force is applied to the horn to hold the workpieces between the tip and the stationary anvil. A full weld cycle has four steps: clamping, welding, holding, and unloading. The clamping load is applied in the first step, while vibration only occurs during the welding step. Sometimes a pre-vibration of a smaller amplitude is generated before the welding step to facilitate welding of harder materials. Generally, workpieces are first clamped between the tip and the anvil, and then forced to vibrate by the vibrating tip. A combination of normal and tangential force is

applied during the welding step, resulting in weld formation at the workpiece interface. After the welding step, the workpiece is held for a short time for cooling. The process finishes once the clamping force is released.

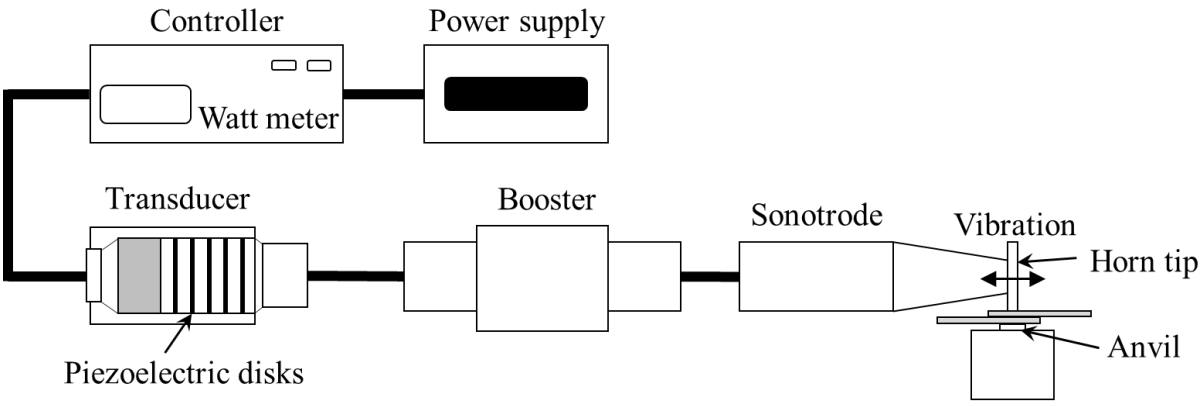

Figure 2.1. Schematic of a metal ultrasonic welding machine.

2.2. Weld Quality Evaluation and Characterization

Weld quality is one of the essential topics in studying ultrasonic welding. Different mechanical tests have been used to evaluate weld strength, and many weld attributes associated with weld strength have been used to determine weld quality. Weld strength is the maximum load carrying capacity of a weld before failure, typically measuring the normal strength [1] using a U-tensile test, and the shear strength [2-3] using the lap-shear test, or the T-peel test for its mix-mode strength [4], as shown in Fig. 2.2. Sometimes different mechanical testing methods are correlated to provide additional information on weld strength characterization [5].

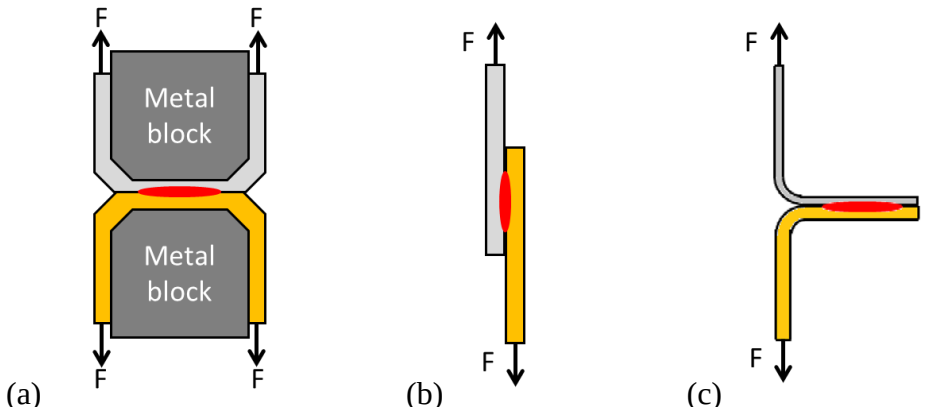

Figure 2.2. Mechanical test method for weld strength measurement: (a) U-tensile test, (b) lap-shear test, and (c) T-peel test.

During mechanical tests, three major failure modes with respect to different weld strengths can be observed and are used to classify the weld quality in general. Interfacial failure typically occurs with relatively low weld strength and a weld with such a failure is typically called a "cold weld". Partial failure or even pull out of the base material indicates a strong interfacial bonding. A weld of this type has relatively high weld strength and is generally defined as a "good weld". Circumferential fracture at the base material with relatively low weld strength generally implies extreme thinning and cracks, and a weld with such a failure mode is called an "over weld". The example of different weld qualities with corresponding failure mode is presented in Fig. 2.3. Sometimes, the transition from different weld failure modes is not very clear, and more detailed classifications are employed. Kim *et al.* [6] proposed a five-level systematic weld quality classification based on T-peel test. Lee *et al.* [7] identified four quality levels based on U-tensile tests.

Identifying weld attributes that have a strong relationship with the weld strength can help determine the weld quality. One frequently discussed weld attribute is bond density, which is typically proportional to weld strength at the early stage of the process. Bond density has less

influence on weld strength when the entire weld zone is bonded. Kong's group [8-9] proposed a direct way to measure the percentage of contact points showing diffusion, which they call "linear weld density". Hardness is also a widely used attribute as an indicator for weld strength [10-11] because it is related to material strength [12-13]. Lee *et al.* [7] proposed four critical weld attributes to describe the weld conditions and correlate them to weld quality: bond density, post weld thickness, size of the weld region, and size of the thermal affected zone. This study shows that the weld strength is affected by a combination of bond density and post weld thickness. Well defined weld attributes link weld quality with metallurgical characteristics and help to better understand the underlying mechanisms of the process.

In addition to weld strength, fatigue behavior [14] and corrosion resistance [15-16] have also been associated with the prediction of the life length and reliability of a weld, especially for battery tab joining.

2.3. Process Parameters

Three primary process parameters in USW are clamping pressure, vibration amplitude, and welding time/energy. There is an optimal combination of the parameter levels to achieve a weld with highest strength as they interact when forming the joint [17]. Insufficient clamping pressure cannot guarantee close surface-to-surface contact, while excessive pressure prohibits the relative motion at the faying surfaces [18]. Similarly, sufficient welding time/energy is required to ensure sufficient development of the bond, but over welding may occur if welding time is too long or too much welding energy is used [19]. Large enough vibration amplitude enables relative motion between workpieces, yet vibration fatigue may occur if the amplitude is too large [20]. Researchers have also found strong interactions among these parameters. Elangovan *et al.* [21]

found a strong interaction between clamping pressure and welding time, and clamping pressure and vibration amplitude in USW of copper sheets. Kim *et al.* [6] found interactions between welding time and clamping pressure in process optimization of Ni-coated Cu welding, and provided a weldability lobe under the proposed weld quality criterion, as shown in Fig. 2.3.

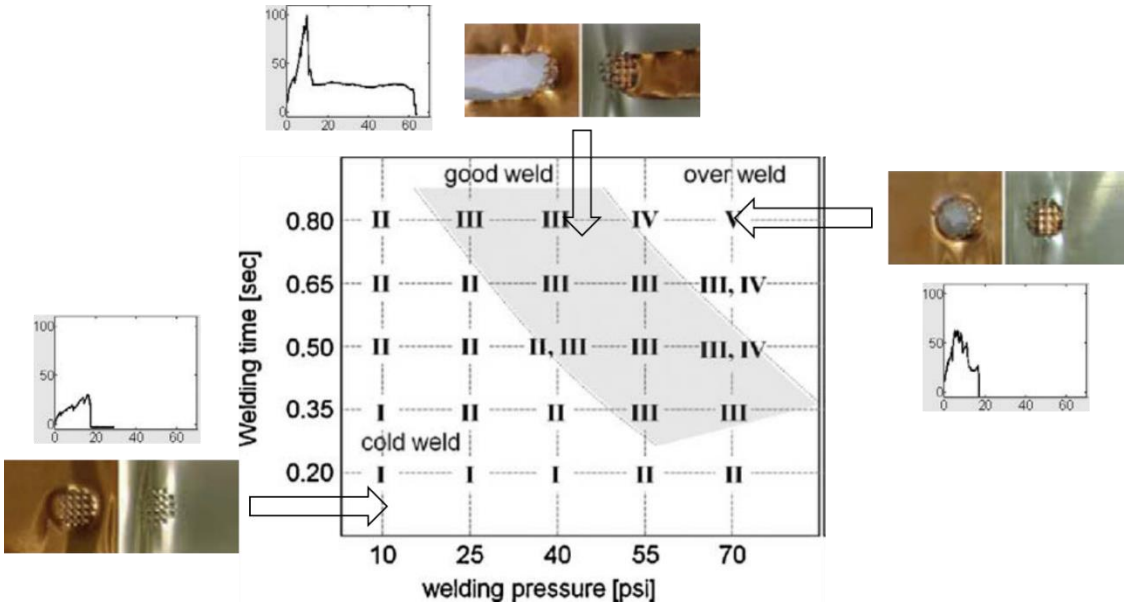

Figure 2.3. Weldability lobe with corresponding weld strengths and failure modes (adopted from Kim et al. [6]).

Other crucial parameters that noticeably influence the USW process include tool geometry [22-28], surface conditions of the workpieces [29-31], and workpiece size [32]. Of these parameters, the influence of tool geometry has attracted more attention in recent years because the tool geometry influences the stress distribution in workpiece [28], capability of gripping workpieces [27], and interfacial contact geometries [26]. Well-designed tool geometries will not only help increase weld strength but also enhance the weldability and tool life.

Process parameters significantly affect weld formation and performance in USW. Optimization of the process parameters is essential to weld production and quality control.

Parametric studies provide guidelines for process robustness. But to reduce the development time of the process optimization, a deeper understanding of the underlying physics needs to be developed.

.

2.4. Process Robustness

The process robustness is one of the core topics in USW. Researchers continuously explore methods to improve the weldability and increase weld strength. Tsujino's group [10, 20, 33] spent years studying the feasibility of complex vibration such as moving the sonotrode in an elliptical path instead of straight back-and-forward. They found a better weld with higher strength and smaller vibration damage can be achieved with much smaller amplitude using this complex vibration pattern. Lee and Cai [34] tried to optimize the pattern of the sonotrode tip using 2D FEM. Yang and Cao experimentally and computationally investigated USW of Cu-Al with resistance heat assistance [36] [35]. They claimed an enhanced weld with shorter welding time and thinner IMC layer can be achieved with properly selected current.

2.5. Bonding Mechanisms

Extensive studies have focused on the bonding mechanisms in USW to develop an in-depth understanding of the joining mechanisms for process design, monitoring, and robustness. Based on microstructural analysis, four major theories have been proposed, as set forth below:

1) *Local melting with rapid cooling*: Some researchers found phenomena that can be referred as local melting with rapid cooling and solidification [37-39]. Kreye [40] observed extremely fined grains in USW of Al-to-Cu via transmission electronic microscopy (TEM) and interpreted the observation as short time melting and rapid solidification. Gunduz *et*

al. [38] hypothesized local melting occurred in thermally enhanced USW of Al-to-Zn at a temperature below the equilibrium liquidus because of high strain-induced vacancy at the interface. Macwan and Chen [[39] observed squeezed-out eutectic liquid at the edge of the nugget in USW of Cu-to-Mg at high welding energy, and suggested local melting occurs in the process. De Vries [11] summarized that most melting phenomena in USW occur in welding dissimilar material with significantly different melting temperatures. Although several studies reported local melting, as a solid-state welding process the overall temperature in USW is below the melting temperature. In addition, diffusion typically accompanies local melting and is generally predominant in those processes.

2) *Diffusion across weld interface*: Interfacial diffusion is a widely agreed bonding mechanism in USW, especially in welding dissimilar materials [40-49]. Studies already show that diffusion is a primary bonding mechanism in USW with local melting [39-40]. As a solid-state welding process, most bonds are formed by diffusion without local melting [41-49]. During the process, diffusion is induced by both elevated temperature and increased vacancies under high strain rate caused by ultrasonic vibration. Ji *et al.*[41] and Li *et al.* [42] both proposed short circuit diffusion as the prominent diffusion mechanism in USW by studying USW of Ni-to-Al and Al-to-Au. Both research groups found large numbers of micro-defects such as vacancies and dislocations at the welding interface, which provides a fast diffusion path that allows diffusion in a short period at relatively low temperature.

The direction of interfacial diffusion depends on the mutual solubility of the welded materials, and sometimes intermetallic compounds (IMCs) form [43-49]. Zhang *et al.* [43] studied the USW of Al-to-Cu and discovered a thin transition layer composed of

amorphous phase and nanocrystallites rather than Al-Cu IMCs in the bonding area. Yang and Cao [36] found large amount of IMCs from an analysis of the element distribution via energy-dispersive X-ray (EDX) in thermal enhanced USW of A6061-to-Cu. Zhang *et al*. [45] studied USW of Al 6111–TiAl6V4 and found no IMCs at the interface. By comparing the metallurgical features in USW of Al-to-Ti, Al-to-Fe, and Al-to-Mg, they argued that interfacial reactions in dissimilar USW depend on mutual solid solubility, diffusion, temperature, and energy barrier for nucleating IMC.

3) *Mechanical interlocking*: another frequently discussed bonding mechanism is macro-level mechanical interlocking [1, 2, 23, 49]. Severe plastic deformation and material softening due to thermal and acoustic effects enables the formation of mechanical interlocking at the weld interface. Joshi [23] found that mechanical interlocking or mixing plays an important role in bond formation in addition to plastic deformation in USW of Al-to-Au. Jahn *et al*. [23] studied the influence of welding energy and anvil geometry on microstructures in USW of Al 6111-T4, and pointed out that the interface changes from planar to wavy morphology as welding energy increases. They also found that the geometry of anvil affects the formation of mechanical interlocking, but the influence decays with increasing welding energy. Bakavos and Prangnell [13] further developed the theory of mechanical interlocking in USW of 6111 Al alloys. They concluded that the wave-like displacement has three length scales, ranging from ~ 5 μm in the early weld stage, when micro asperities at the mating surfaces fold, deform, and form microbonds; to ~20 to 50 μm when microbonded planes appear to rotate out of plane; and finally to ~ 1 mm, when the interfacial wave line displays a shape associated with the pitch of the sonotrode tip pattern. Lee *et al.* [7] showed the coexistence of metallurgical adhesion and mechanical

interlocking in USW of Cu-to-Cu. Wu *et al.* [10] found that the primary welding mechanism among Al tabs is mechanical mixing in multi-layered USW of 3-layered Al tabs to a Cu bus bar.

Mechanical interlocking arises from both cyclic shear plastic motion and tool geometry, and typically appears in welding of soft materials concomitantly with other bonding mechanisms such as metallic bonding in particular, as described below.

4) *Metallic bonding across nascent metal contacts*: a bonding mechanism universally present in ultrasonic welding is the atomic attraction forces across nascent metal contacts. Due to the inherent characteristics of metallic bonding, metals can form a bond under the electrostatic attractive force between the negative electron sea and positive metal ions, no matter whether the metals are similar or dissimilar [51]. To form metallic bonding at the mating surfaces, two conditions must be fulfilled. First, the surfaces must be clean and free of an oxide layer or contaminant. Second is that the surfaces must have intimate contact. These two conditions can be automatically achieved in USW. The friction-like motion helps abrade away the oxide layers and contaminants, leading to exposure of clean surfaces. The clamping pressure facilitates plastic deformation of asperities at the interface and ensures the intimate contact at the weld interface. Zhang and Li [52] studied this phenomenon by establishing a thermal-mechanical model for USW of Al foils. Both Ram's team [53-54] and Prangnell's team [13] pointed out that the microbonds initiate at contact asperities, and grow along the interface as those asperities deform under simultaneous application of normal and oscillating shear stress. Researchers [55-57] found recrystallization and grain growth induced by severe localized plastic deformation also play an important role in bond formation in USW of Al alloys.

To summarize, the bond formation in ultrasonic welding has complex mechanisms that have been studied by various researchers for decades. Four major bonding mechanisms have been proposed and discussed by analyzing the metallurgical features of a weld via microscopy, such as optical microscopy, scanning electron microscopy (SEM), transmission electron microscopy (TEM), and energy dispersive X-ray (EDS). The occurrence of different bonding mechanisms depends on material combinations, properties, and thermal-mechanical behaviors under the effect of various process conditions. Sometimes multiple bonding mechanisms coexist in a single weld. The driving force of bond formation and the relationship between bonding mechanisms and process parameters are not yet fully understood.

2.6. Weld Formation

Previous studies indicate a similar thermal-mechanical behavior during the USW process regardless of the bonding mechanisms [57-60]. By tracking the motion of the tool and workpieces, and correlating the relative motion to the microstructural evolution of the joint, as well as its welding strength, researchers have divided the welding process into different stages. Li *et al*. [60] and Sasaki *et al*. [59] tracked the motion of tool and workpieces in two-layered USW. Lee *et al*. [61] and Arimoto *et al*. [62] conducted similar studies in multi-layered USW. All researchers found similar major stages during the welding process.

At the beginning of the weld process, stress in the workpiece concentrates at the peaks of the patterned horn and anvil tools and increases under clamping pressure and oscillating lateral shear motion. The tools penetrate into workpieces once the yield strength is reached. The top workpiece is then gripped and moves together with the sonotrode tip. Considerable relative motion thus emerges at the faying interface of the workpiece, which helps break and disperse oxide layers

and surface contaminants. Li *et al*. [60] recorded the temperature history at different points of a weld and interpreted that heat is generated due to interfacial friction at this stage. Microstructural analysis at early stage of Cu-to-Cu USW by Lee *et al*. [1] showed finer grains, which implies work hardening at workpieces, especially at the stress concentration of the tool/workpiece interface.

As the welding process proceeds, intimate metal-to-metal contact initiates, resulting in localized microbonds at some asperities. These microbonds are torn apart due to the relative motion at the interfacial, but progressively expand as the asperities soften and collapse under the effect of plastic deformation and increasing temperature. The growth of the bonds enhances the coupling of the workpiece and inhibits their relative motion. . The vibration of the workpieces eventually synchronizes, and the relative motion between tool and workpieces increases [57, 59]. During this stage, shearing forces in the opposite directions on the two sides of workpiece increase, introducing more severe plastic deformation that contributes to heat generation. Meanwhile, friction at the tool/workpiece interface increases and generates heat at the contact regions. The generated heat is conducted over the entire weld region, raising the bulk temperature and further softening the materials.

A strong bond forms during the stage when workpieces vibrate simultaneously with small relative motion. During this stage, most asperities are flattened, voids are closed, bonding expands over the entire weld zone, and the sonotrode tip, workpieces, and anvil are vibrating at their own amplitudes. Consequently, a relatively stable dynamic condition is achieved [60, 62]. Concurrently, shearing forces at the sonotorde/top layer interface, the welding interface, and the anvil/bottom layer interface are out of phase, resulting in significant plastic deformation and ultrahigh strain rate in the materials. A large amount of heat is generated by both interfacial friction and plastic deformation. These coupled thermal-mechanical effects facilitate the evolution of the

interfacial bond through different bonding mechanisms including diffusion, recrystallization, interlocking, and even local melting.

Finally, an over-welding occurs if too much energy is applied. The materials are extremely softened with continuously rising temperature, allowing deeper penetration of tool into the workpiece. The workpiece may therefore become extremely thinned, leading to a reduction in cross sectional area and consequently lower load carrying capacity. Meanwhile overheating may occur at the tool/workpiece interface, causing sticking [9]. Moreover, excessive deformation may introduce brittle ultra-fine grains, and overheating may result in undesired brittle IMCs at the welding interface.

2.7. Mechanical and thermal fundamentals

The bond evolution in USW indicates significant contributions form mechanical and thermal influences, as seen in the following three aspects discussed below.

1) *Material hardening and softening*: during USW process, the material undergoes both work hardening and softening effect. Lee *et al.* [63] indicated that the evolution of stress is a combination of isotropic and kinematic hardening. The isotropic hardening is due to flow rules, where the material yields and the surface remains the same shape but expands with increasing stress. Whereas kinematic hardening is caused by cyclical loading and back stresses, where the yielded surface shifts with constant size and the Bauschinger effect applies [64-65]. At the same time, material is softened under superimposed elevated temperature and acoustic effects [68-70]. It is well-known that the yield strength decreases with higher temperature. An early study by Langenecker [68] claimed that highly localized regions, such as dislocations, voids, and grain boundaries, move faster and more freely

after absorbing acoustic energy. The plastic limit of the material then proportionally decreases with increasing ultrasonic intensity without the aid of thermal activities. Siddiq and colleagues [65-66] performed a series of studies of thermal-mechanical modeling in USW, and found that the acoustic effect plays an indispensable role in material softening.

2) *Heat generation*: there are two heat sources in USW. The first is the interfacial friction. The frictional heat generated is proportional to the frictional force and interfacial relative motion rate [63, 69]. The other heat source is plastic deformation, which is a function of yield stress and relative motion [24]. Simulation results [70-72] show the maximum temperature is below the melting temperature of the base material and occurs at the center of the weld area, either at weld interface or tool/workpiece interface, where it is subjected to more plastic deformation and friction.

3) *Interfacial thermal dynamics*: where the bonding mechanisms depends on the thermal dynamic properties of the material and local thermal-mechanical behaviors. Computational methods have been employed to predict the interfacial thermal dynamic evolutions in recent years. Robson *et al*. [73] simulated the IMC formation in USW of Al-Mg and found that IMCs formed quickly at local microbonds in the initial stages of the welding process, and grow slowly once local bonds impinge. Shen *et al.* [74] modeled the interfacial grain evolution in USW of Cu tabs, and observed three predominant microstructural evolutions from the beginning to the end of the process, which are severe plastic deformation, dynamic recrystallization, and subsequent grain growth. Ward *et al.* [75] predicted grain growth because of frictional heating in USW of Ag-Cu.

2.8. Multi-layered USW

A number of studies have focused on two-layer USW, and only in recent years has multi-layered USW started to receive more attention because of the increasing demand for battery tab joining. The bonding mechanisms and underlying thermal-mechanical physics in multi-layered USW are similar to those in two-layered welds. The primary difference is the non-uniform interfacial conditions in multi-layered process, which makes weld quality inconsistent and more difficult to control. Lee *et al*. [63] investigated the thermal-mechanical behavior in USW of three-layered Al tabs to a Cu bus bar using FEM. The simulation results showed more heat and a larger vibration amplitude is generated at the top workpiece. Lee *et al*. [61] used a high-speed camera to trace the vibration of individual layers in welding multiple layers of the same material, and studied the influence of different anvil geometry on the vibration transmissions. The study showed with finer anvil the largest relative motion occurs at the top interface and monotonically decreases to the bottom. With a coarser anvil, the largest relative motion occurs at the top interface and smallest relative motion at middle interface. Wu *et al*. [10] experimentally studied the joint formation in USW of three-layered Al tabs to a Cu bus bar and three-layered Cu tabs to a Cu bus bar, and found different bonding mechanisms at different interfaces in the welding process with dissimilar materials. Das *et al.* [76] conducted a full factorial experiment on multi-layered USW of Al-Cu. They observed a complex relation between weld strength and the main effects and interactions of the process parameters. They proposed a third-order polynomial regression model of the process parameters to determine the maximum weld strength in lap shear and T-peel tests.

To summarize, the study of multi-layered USW is still in an early stage and joint formation at mating interfaces and its propagation through different interfaces is still unclear. To improve weld quality and provide better guidelines for the development of robust processes for multi-

layered USW, a deeper understanding needs to be developed on the joint formation at the mating surfaces and the joint propagation through different interfaces.

2.9. Summary

Ultrasonic welding has been studied for years. USW weld quality is defined by mechanical performance and the associated weld attributes. The influence of process parameters on weld performance has been evaluated and process optimization based on parametric studies has been discussed. Theories of four major bonding mechanisms, including local melting, diffusion, mechanical interlocking, and metallic bonding, have been developed. The joint evolution and the underlying thermal-mechanical fundamentals have been studied. Process robustness has been investigated based on a better understanding primarily of the process for single interface joints. More attention to multi-layered USW has arisen in the last decade. Nevertheless, the understanding in multi-layered USW is still limited. There is a lack of knowledge on joint formation at individual interfaces and the propagation of the weld as it evolves through the different interfaces.

References

[1] Lee, S.S., Kim, T.H., Hu, S.J., Cai, W.W., Abell, J.A. and Li, J., 2013. Characterization of joint quality in ultrasonic welding of battery tabs. Journal of Manufacturing Science and Engineering, 135(2), p.021004.

[2] Bakavos, D. and Prangnell, P.B., 2010. Mechanisms of joint and microstructure formation in high power ultrasonic spot welding 6111 aluminium automotive sheet. Materials Science and Engineering: A, 527(23), pp.6320-6334.

[3] Patel, V.K., Bhole, S.D. and Chen, D.L., 2012. Microstructure and mechanical properties of dissimilar welded Mg–Al joints by ultrasonic spot welding technique. Science and Technology of Welding and Joining, 17(3), pp.202-206.

[4] Lee, S.S., Kim, T.H., Hu, S.J., Cai, W.W. and Abell, J.A., 2010, January. Joining technologies for automotive lithium-ion battery manufacturing: A review. In ASME 2010 international manufacturing science and engineering conference (pp. 541-549). American Society of Mechanical Engineers.

[5] Das, A., Li, D., Williams, D. and Greenwood, D., 2019. Weldability and shear strength feasibility study for automotive electric vehicle battery tab interconnects. Journal of the Brazilian Society of Mechanical Sciences and Engineering, 41(1), p.54.

[6] Kim, T.H., Yum, J., Hu, S.J., Spicer, J.P. and Abell, J.A., 2011. Process robustness of single lap ultrasonic welding of thin, dissimilar materials. CIRP annals, 60(1), pp.17-20.

[7] Andrea, D., 2010. Battery management systems for large lithium ion battery packs. Artech house.

[8] Kong, C.Y., Soar, R.C. and Dickens, P.M., 2003. Characterisation of aluminium alloy 6061 for the ultrasonic consolidation process. Materials Science and Engineering: A, 363(1-2), pp.99-106.

[9] Kong, C.Y., Soar, R.C. and Dickens, P.M., 2004. Optimum process parameters for ultrasonic consolidation of 3003 aluminium. Journal of materials processing technology, 146(2), pp.181-187.

[10] Tsujino, J., Hidai, K., Hasegawa, A., Kanai, R., Matsuura, H., Matsushima, K. and Ueoka, T., 2002. Ultrasonic butt welding of aluminum, aluminum alloy and stainless steel plate specimens. Ultrasonics, 40(1-8), pp.371-374.

[11] Shakil, M., Tariq, N.H., Ahmad, M., Choudhary, M.A., Akhter, J.I. and Babu, S.S., 2014. Effect of ultrasonic welding parameters on microstructure and mechanical properties of dissimilar joints. Materials & Design, 55, pp.263-273.

[12] Zhou, M., Hu, S.J. and Zhang, H., 1999. Critical specimen sizes for tensile-shear testing of steel sheets. WELDING JOURNAL-NEW YORK-, 78, pp.305-s.

[13] Pavlina, E.J. and Van Tyne, C.J., 2008. Correlation of yield strength and tensile strength with hardness for steels. Journal of Materials Engineering and Performance, 17(6), pp.888-893.

[14] Rinker, T.J., Pan, J., Santella, M. and Pan, T.Y., 2018. Fatigue behavior of dissimilar ultrasonic welds in lap-shear specimens of AZ31 and steel sheets. Engineering Fracture Mechanics, 189, pp.405-426.

[15] Hyams, T.C., Go, J. and Devine, T.M., 2007. Corrosion of aluminum current collectors in high-power lithium-ion batteries for use in hybrid electric vehicles. Journal of The Electrochemical Society, 154(8), pp.C390-C396.

[16] Pan, T.Y., Feng, Z., Santella, M. and Chen, J., 2013. Corrosion behavior of mixed-metal joint of magnesium to mild steel by ultrasonic spot welding with and without adhesives. SAE International Journal of Materials and Manufacturing, 6(2), pp.271-278.

[17] Graff, K., 2005. Ultrasonic metal welding. In New developments in advanced welding (pp. 241-269). Woodhead Publishing.

[18] Bakavos, D., Chen, Y.C. and Prangnell, P.B., 2011. Mechanisms of Joint Formation in Ultrasonic Spot Welding Aluminium Automotive Sheet. Supplemental Proceedings: Materials Processing and Energy Materials, 1, pp.735-742.

[19] Yang, J., Cao, B. and Lu, Q., 2017. The effect of welding energy on the microstructural and mechanical properties of ultrasonic-welded copper joints. Materials, 10(2), p.193.

[20] Tsujino, J., Yokozuka, T., Suga, S. and Sugimoto, E., 2010, October. Welding characteristics of bi-metal, braided wires, aluminum and copper foils using 20 kHz ultrasonic complex vibration welding equipments. In 2010 IEEE International Ultrasonics Symposium (pp. 1420-1423). IEEE.

[21] Elangovan, S., Prakasan, K. and Jaiganesh, V., 2010. Optimization of ultrasonic welding parameters for copper to copper joints using design of experiments. The International Journal of Advanced Manufacturing Technology, 51(1-4), pp.163-171.

[22] Elangovan, S., Anand, K. and Prakasan, K., 2012. Parametric optimization of ultrasonic metal welding using response surface methodology and genetic algorithm. The International Journal of Advanced Manufacturing Technology, 63(5-8), pp.561-572.

[23] Jahn, R., Cooper, R. and Wilkosz, D., 2007. The effect of anvil geometry and welding energy on microstructures in ultrasonic spot welds of AA6111-T4. Metallurgical and Materials Transactions A, 38(3), pp.570-583.

[24] Chen, K. and Zhang, Y., 2015. Mechanical analysis of ultrasonic welding considering knurl pattern of sonotrode tip. Materials & Design, 87, pp.393-404.

[25] Shin, H.S. and de Leon, M., 2015. Parametric study in similar ultrasonic spot welding of A5052-H32 alloy sheets. Journal of Materials Processing Technology, 224, pp.222-232.

[26] Satpathy, M.P. and Sahoo, S.K., 2017. Parametric analysis on plastic deformation of materials during ultrasonic spot welding with different anvil geometries. International Journal of Manufacturing Technology and Management, 31(4), pp.344-361.

[27] Feng, M.N. and Luo, Z., 2019. Interface morphology and microstructure of high-power ultrasonic spot welded Mg/Al dissimilar joint. Science and Technology of Welding and Joining, 24(1), pp.63-78.

[28] Sasaki, T., Komiyama, K. and Pramudita, J.A., 2018. Influence of tool edge angle on the bondability of aluminum in ultrasonic bonding. Journal of Materials Processing Technology, 252, pp.167-175.

[29] Haddadi, F., Strong, D. and Prangnell, P.B., 2012. Effect of zinc coatings on joint properties and interfacial reactions in aluminum to steel ultrasonic spot welding. JOM, 64(3), pp.407-413.

[30] Al-Sarraf, Z. and Lucas, M., 2012. A study of weld quality in ultrasonic spot welding of similar and dissimilar metals. In Journal of Physics: Conference Series (Vol. 382, No. 1, p. 012013). IOP Publishing.

[31] Hetrick, E.T., Baer, J.R., Zhu, W., Reatherford, L.V., Grima, A.J., Scholl, D.J., Wilkosz, D.E., Fatima, S. and Ward, S.M., 2009. Ultrasonic metal welding process robustness in aluminum automotive body construction applications. Weld. J, 88(7), pp.149-158.

[32] Wright, N.W., Robson, J.D. and Prangnell, P.B., 2009. Effects of Thickness Combinations on Joint Properties and Process Windows in Ultrasonic Metal Welding (No. 2009-01-0027). SAE Technical Paper.

[33] Tsujino, J., Ueoka, T., Kashino, T. and Sugahara, F., 2000. Transverse and torsional complex vibration systems for ultrasonic seam welding of metal plates. Ultrasonics, 38(1-8), pp.67-71.

[34] Lee, D. and Cai, W., 2017. The effect of horn knurl geometry on battery tab ultrasonic welding quality: 2D finite element simulations. Journal of Manufacturing Processes, 28, pp.428-441.

[35] Li, H., Cao, B., Yang, J.W. and Liu, J., 2018. Modeling of resistance heat assisted ultrasonic welding of Cu-Al joint. Journal of Materials Processing Technology, 256, pp.121-130.

[36] Yang, J. and Cao, B., 2015. Investigation of resistance heat assisted ultrasonic welding of 6061 aluminum alloys to pure copper. Materials & Design, 74, pp.19-24.

[37] De Vries, E., 2004. Mechanics and mechanisms of ultrasonic metal welding (Doctoral dissertation, The Ohio State University).

[38] Gunduz, I.E., Ando, T., Shattuck, E., Wong, P.Y. and Doumanidis, C.C., 2005. Enhanced diffusion and phase transformations during ultrasonic welding of zinc and aluminum. Scripta materialia, 52(9), pp.939-943.

[39] Macwan, A. and Chen, D.L., 2015. Microstructure and mechanical properties of ultrasonic spot welded copper-to-magnesium alloy joints. Materials & Design, 84, pp.261-269.

[40] Kreye, H., 1977. Melting phenomena in solid state welding processes. Weld. J, 56(5), pp.154-158.

[41] Ji, H., Li, M., Kung, A.T., Wang, C. and Li, D., 2005. The diffusion of Ni into Al wire at the interface of ultrasonic wire bond during high temperature storage. In 2005 6th International Conference on Electronic Packaging Technology (pp. 377-381). IEEE.

[42] Li, J., Han, L. and Zhong, J., 2008. Short‐circuit diffusion of ultrasonic bonding interfaces in microelectronic packaging. Surface and Interface Analysis: An International Journal devoted to the development and application of techniques for the analysis of surfaces, interfaces and thin films, 40(5), pp.953-957.

[43] Zhang, Z., Wang, K., Li, J., Yu, Q. and Cai, W., 2017. Investigation of interfacial layer for ultrasonic spot welded aluminum to copper joints. Scientific reports, 7(1), p.12505.

[44] Yang, J. and Cao, B., 2015. Investigation of resistance heat assisted ultrasonic welding of 6061 aluminum alloys to pure copper. Materials & Design, 74, pp.19-24.

[45] Zhang, C.Q., Robson, J.D., Ciuca, O. and Prangnell, P.B., 2014. Microstructural characterization and mechanical properties of high power ultrasonic spot welded aluminum alloy AA6111–TiAl6V4 dissimilar joints. Materials characterization, 97, pp.83-91.

[46] Prangnell, P., Haddadi, F. and Chen, Y.C., 2011. Ultrasonic spot welding of aluminium to steel for automotive applications—microstructure and optimisation. Materials Science and Technology, 27(3), pp.617-624.

[47] Panteli, A., Robson, J.D., Brough, I. and Prangnell, P.B., 2012. The effect of high strain rate deformation on intermetallic reaction during ultrasonic welding aluminium to magnesium. Materials Science and Engineering: A, 556, pp.31-42.

[48] Panteli, A., Chen, Y.C., Strong, D., Zhang, X. and Prangnell, P.B., 2012. Optimization of aluminium-to-magnesium ultrasonic spot welding. Jom, 64(3), pp.414-420.

[49] Haddadi, F., 2015. Rapid intermetallic growth under high strain rate deformation during high power ultrasonic spot welding of aluminium to steel. Materials & Design, 66, pp.459-472.

[50] Wu, X., Liu, T. and Cai, W., 2015. Microstructure, welding mechanism, and failure of Al/Cu ultrasonic welds. Journal of Manufacturing Processes, 20, pp.321-331.

[51] Grigorovich, V.K., 1989. The metallic bond and the structure of metals.

[52] Zhang, C.S. and Li, L., 2009. A coupled thermal-mechanical analysis of ultrasonic bonding mechanism. Metallurgical and Materials Transactions B, 40(2), pp.196-207.

[53] Janaki Ram, G.D., Robinson, C., Yang, Y. and Stucker, B.E., 2007. Use of ultrasonic consolidation for fabrication of multi-material structures. Rapid Prototyping Journal, 13(4), pp.226-235.

[54] Yang, Y., Ram, G.J. and Stucker, B.E., 2009. Bond formation and fiber embedment during ultrasonic consolidation. Journal of Materials Processing Technology, 209(10), pp.4915-4924.

[55] Ji, H., Wang, J. and Li, M., 2014. Evolution of the bulk microstructure in 1100 aluminum builds fabricated by ultrasonic metal welding. Journal of Materials Processing Technology, 214(2), pp.175-182.

[56] Dehoff, R.R. and Babu, S.S., 2010. Characterization of interfacial microstructures in 3003 aluminum alloy blocks fabricated by ultrasonic additive manufacturing. Acta Materialia, 58(13), pp.4305-4315.

[57] Lu, Y., Song, H., Taber, G.A., Foster, D.R., Daehn, G.S. and Zhang, W., 2016. In-situ measurement of relative motion during ultrasonic spot welding of aluminum alloy using Photonic Doppler Velocimetry. Journal of Materials Processing Technology, 231, pp.431-440.

[58] Mariani, E. and Ghassemieh, E., 2010. Microstructure evolution of 6061 O Al alloy during ultrasonic consolidation: an insight from electron backscatter diffraction. Acta Materialia, 58(7), pp.2492-2503.

[59] Sasaki, T., Watanabe, T., Hosokawa, Y. and Yanagisawa, A., 2013. Analysis for relative motion in ultrasonic welding of aluminium sheet. Science and Technology of Welding and Joining, 18(1), pp.19-24.

[60] Li, H., Choi, H., Ma, C., Zhao, J., Jiang, H., Cai, W., Abell, J.A. and Li, X., 2013. Transient temperature and heat flux measurement in ultrasonic joining of battery tabs using thin-film microsensors. Journal of Manufacturing Science and Engineering, 135(5), p.051015.

[61] Lee, S.S., Kim, T.H., Hu, S.J., Cai, W.W. and Abell, J.A., 2015. Analysis of weld formation in multilayer ultrasonic metal welding using high-speed images. Journal of Manufacturing Science and Engineering, 137(3), p.031016.

[62] Arimoto, K., Sasaki, T. and Kim, T., 2019. Ultrasonic Bonding of Multi-Layered Foil Using a Cylindrical Surface Tool. Metals, 9(5), p.505.

[63] Lee, D., Kannatey-Asibu, E. and Cai, W., 2013. Ultrasonic welding simulations for multiple layers of lithium-ion battery tabs. Journal of Manufacturing Science and Engineering, 135(6), p.061011.

[64] Chun, B.K., Jinn, J.T. and Lee, J.K., 2002. Modeling the Bauschinger effect for sheet metals, part I: theory. International Journal of Plasticity, 18(5-6), pp.571-595.

[65] Siddiq, A. and Ghassemieh, E., 2008. Thermomechanical analyses of ultrasonic welding process using thermal and acoustic softening effects. Mechanics of Materials, 40(12), pp.982-1000.

[66] Siddiq, A. and El Sayed, T., 2011. Acoustic softening in metals during ultrasonic assisted deformation via CP-FEM. Materials Letters, 65(2), pp.356-359.

[67] Kelly, G.S., Advani, S.G., Gillespie Jr, J.W. and Bogetti, T.A., 2013. A model to characterize acoustic softening during ultrasonic consolidation. Journal of Materials Processing Technology, 213(11), pp.1835-1845.

[68] Langenecker, B., 1966. Effects of ultrasound on deformation characteristics of metals. IEEE Transactions on Sonics and Ultrasonics, 13(1), pp.1-8.

[69] Li, H., Cao, B., Liu, J. and Yang, J., 2018. Modeling of high-power ultrasonic welding of Cu/Al joint. The International Journal of Advanced Manufacturing Technology, 97(1-4), pp.833-844.

[70] Elangovan, S., Semeer, S. and Prakasan, K., 2009. Temperature and stress distribution in ultrasonic metal welding—An FEA-based study. Journal of materials processing technology, 209(3), pp.1143-1150.

[71] Chen, K. and Zhang, Y., 2015. Mechanical analysis of ultrasonic welding considering knurl pattern of sonotrode tip. Materials & Design, 87, pp.393-404.

[72] Jedrasiak, P. and Shercliff, H.R., 2018. Finite element analysis of heat generation in dissimilar alloy ultrasonic welding. Materials & Design, 158, pp.184-197.

[73] Robson, J., Panteli, A. and Prangnell, P.B., 2012. Modelling intermetallic phase formation in dissimilar metal ultrasonic welding of aluminium and magnesium alloys. Science and Technology of Welding and Joining, 17(6), pp.447-453.

[74] Shen, N., Samanta, A., Ding, H. and Cai, W.W., 2016. Simulating microstructure evolution of battery tabs during ultrasonic welding. Journal of Manufacturing Processes, 23, pp.306-314.

[75] Ward, A.A., French, M.R., Leonard, D.N. and Cordero, Z.C., 2018. Grain growth during ultrasonic welding of nanocrystalline alloys. Journal of Materials Processing Technology, 254, pp.373-382.

[76] Das, A., Masters, I. and Williams, D., 2019. Process robustness and strength analysis of multi-layered dissimilar joints using ultrasonic metal welding. The International Journal of Advanced Manufacturing Technology, 101(1-4), pp.881-900.

Chapter 3 Weld Formation in Multi-Layered Ultrasonic Welding of Similar and Dissimilar Materials

Abstract

Ultrasonic metal welding has inherent advantages as a solid state welding process and has been widely applied in the joining of battery cell tabs (typically made of Al/Cu) to bus-bar (typically made of Cu). However, the bonding mechanisms and weld formation in such multi-layered welds are still not well understood. The approach to determining proper joining process variables are still largely based on trial-and-error. This chapter investigates the weld formation in two frequently used weld configurations by analyzing the microstructure and interfacial bonding evolution via microscopy and the corresponding weld quality. The two configurations include welds of three-layered Al tabs to bare Cu bus-bar and welds of three-layered Ni-coated Cu tabs to Ni-coated Cu bus-bar. The results show that bonding among Ni-coated Cu sheets consists of metal mixture and mechanical interlocking, and the weld forms from the sonotrode side to the anvil side. In comparison, the bonding among Al tabs is achieved by dynamic recrystallization under severe plastic deformation, and the bonding between Al and Cu is dominated by interfacial diffusion, which requires more input energy to accomplish. Statistical methods are also applied to investigate the influence of process parameters on weld quality.

---

* Part of the content of this chapter has been published in *ASME Journal of Manufacturing Science and Engineering*, under "Joint Formation in Multilayered Ultrasonic Welding of Ni-Coated Cu and the Effect of Preheating.", 2018, 140(1s). The content in Section 3.3.2 has been submitted as a conference paper to *CIRP CATS 2020.*

3.1. Introduction

In assembling batteries for electric vehicles (EVs), multi-layered battery tabs made of Al or Cu are welded to a bus-bar that links multiple battery cells to form a battery module. Multiple modules are then assembled together to form a battery pack to ensure sufficient working voltage and energy capacity. The high thermal and electrical conductivity of Al and Cu make it difficult to achieve good-quality welds using conventional welding technologies. Ultrasonic welding (USW), as a solid-sate welding process, has attracted tremendous interest in welding within and between battery cells. In USW, high frequency oscillation produces tangential motion among workpieces clamped between a sonotrode and an anvil. The reciprocating sliding motion under pressure disperses oxide layers and contaminants, generates heat, induces plastic deformation, produces direct metal-to-metal contact, and as a result, creates a joint at the metal interface. During the process, the temperature is relatively low [1-2], and plastic deformation, rather than melting and solidification, plays a vital role in joint formation [2-4]. Therefore, materials with different properties can be joined with minimal intermetallic compound formation. These inherent characteristics of USW make it well-suited for joining pouch-type prismatic lithium-ion battery cells.

In spite of the advantages of USW, a big challenge in efficiently applying USW in automotive lithium-ion battery welding is to achieve consistent weld quality in multi-layered welds. The current approach to achieving an acceptable multi-layered weld for various processing conditions and material combinations is based largely on trial-and-error methods. To improve the process robustness and weld quality, a better understanding of joint formation in multi-layered USW is highly desirable.

Two primary elements need to be considered to improve the understanding of the welding process in multi-layered USW. One is the weld formation at the interface between two layers, including interfacial bonding and mechanical interlocking, and the other is joint propagation between the different interfaces in multi-layered welding. The weld formation between two sheets in USW has been investigated by many researchers. Bakavos and Prangnell [5], Lee et al. [6], and Zhang et al. [7] studied USW of similar metals and indicated that the work pieces were bonded by metallurgical adhesion with mechanical interlocking. Watanabe et al. [8] and Haddadi [9] observed diffusion bonding in USW of dissimilar materials. Kreye [10] and Gunduz et al. [11] discussed local melting in USW, but the phenomenon was rarely observed by others.

When considering weld propagation from one interface to another, several studies have shown that multi-layered welds are not forming uniformly at the different interfaces resulting in inconsistent interfacial weld performance. Lee *et al.* [12] tracked the vibration of each interface in ultrasonic welds of 4-layered Cu welding and found that different layers vibrate in-phase with different amplitudes, and the relative displacement at different interfaces varies in early stages of the process. The study also shows that the weld formation is notably affected by the shape of the anvil. Temperature distribution and history were analyzed by Lee *et al.* [13] through simulation of the welding process between 3-layered Al tabs and 1 Cu bus-bar. The results imply a non-uniform temperature distribution at different interfaces. Shin and Leon [14] studied different combinations of multi-layered Al-Cu USW welds, and found different weld strength and failure mode at different interfaces. Moreover, the researchers also found that different weld stack-up configurations resulted in different electrical resistance of the weld. Das *et al.* [15] performed systematic study on process robustness and weld strength using statistical methods, and established empirical models predicting the lap-shear and T-peel strength of the interface closer to the anvil side. A T-

peel test at different interfaces from this study also illustrates significant strength difference from interface to interface. In addition, bonding mechanisms vary in different material combinations as indicated by Wu *et al.* [16] in a study of multi-layered Al-to-Cu and Cu-to-Cu ultrasonic welds. In summary, all prior studies in multi-layered USW provide an insight showing inconsistent weld formation and performance due to discrepancies in dynamic, thermo-mechanical, and structural behavior at different interfaces. However, the bonding mechanisms, weld propagation, and influence of process variables are still not very clear.

This chapter aims at developing an in-depth understanding in the bonding mechanisms and weld formation in multi-layered USW of Al-to-Cu and Cu-to-Cu that are frequently used in battery pack manufacturing. The remainder of this chapter is organized as follows: Section 3.2 describes the materials and experimental procedures; Section 3.3 discusses the observations of weld formation and the corresponding weld quality; Section 3.4 investigates the influence of process parameters on weld formation and presents a statistical study showing important variables on weld quality; Section 3.5 summarizes and concludes the findings in this chapter.

3.2. Materials and Experimental Setup

In this research, two weld stack-up configurations, widely seen in lithium-ion battery manufacturing, were investigated. The first was a three-layered pure Ni-coated Cu tabs (0.2 mm, ≥ 99.9% Cu) to one-layer Ni-coated Cu bus-bar (0.9 mm, ≥ 99.9% Cu), designated as '3CC', and the other was a three-layered pure Al (0.2 mm, ≥ 99% Al, ≤ 0.95 % Fe, 0.05-0.2% Cu) to one-layer bare Cu bus-bar (0.5 mm, ≥ 99.9% Cu), designated as '3AC'. The width and length of all studied metal sheets are 41 mm and 45 mm, respectively. The nickel coating on the Ni-coated Cu tab and bus-bar are 2.4 μm and 1.5 μm, respectively. Table 3.1 lists the mechanical properties of

all materials. No special pre and post treatments such as heat treatment or surface cleansing were used on the materials.

Table 3.1 Mechanical Properties of the Metal Sheets

Material		series	Yield Strength (MPa)	Tensile Strength (MPa)	Hardness (Hv)
Tabs	Al	1100	30.7	99.2	35.5
	Ni-coated Cu	110	111	335	91
Bus-bars	Bare Cu	110	70.5	327	92
	Ni-coated Cu	110	255	313	101

The experimental procedure is as follows: 1) three-layered tabs (Al/Cu) were ultrasonically welded to bus-bar (bare/Ni-coated Cu) at different process setting levels; 2) weld zones were characterized by microscopy; 3) weld attributes were characterized and correlated to weld quality assessed by a lap-shear test to evaluate the weld development; and 4) the variation of weld quality and performance subjected to different process parameters was statistically studied.

3.2.1 Ultrasonic Weld Configuration and Procedures

The USW experiments were performed using a Branson^{TM} USW machine (series L20, 5000W maximum power, 20 kHz frequency) with energy-control mode. Figure 3.1 shows the ultrasonic welding machine and the stack-up configurations. A specifically designed jig was mounted on the welder to locate and prevent the metals sheets from undesired motion, as shown in Fig. 3.1 (a). A tip with 3-by-3 hemi-spherical knurls and an anvil with 4-by-5 pyramid knurls were used in this study. The hemi-spherical knurls were perfectly aligned with the 4 pyramid knurls, as illustrated in Fig. 3.1 (b). As described in the schematic picture in Fig. 3.1 (c), the Cu bus-bar was placed on the stationary anvil with three-layered Al tabs put on top of the bus-bar.

The metal sheets from the sonotrode tip (top) to the anvil (bottom) were marked as layer 1st to 4th sequentially, and the interface between layer 1st and 2nd, 2nd and 3rd, and 3rd and 4th were defined as the top, middle, and bottom interface, respectively. The shorter side of the metal sheets was parallel to the direction of the anvil with 5 pyramids in a row, which was also the vibration direction, as shown in Figs. 3.1 (b) and (c). The weld was made at the center of the stack. The areas with tip knurl indentation were defined as valleys, and the protrusions among those indentations were defined as crests.

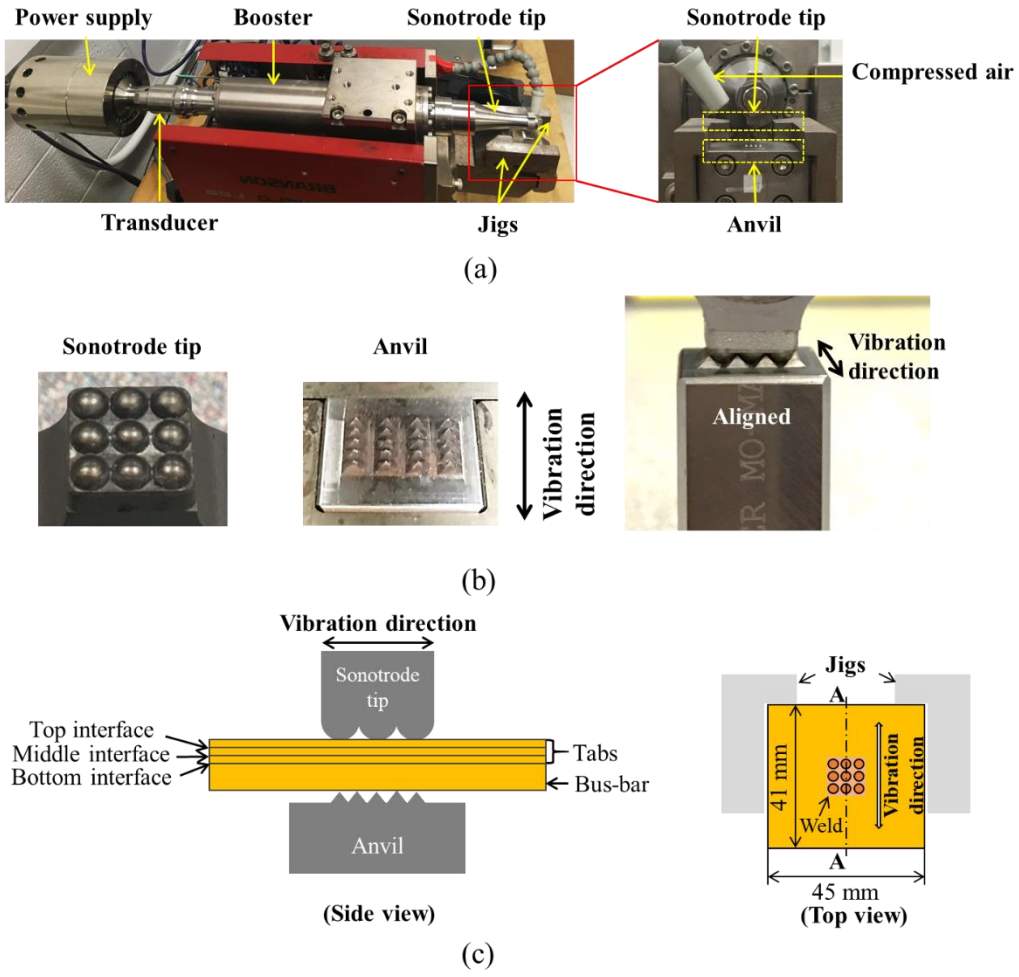

Figure 3.1. Experimental setup showing (a) metal USW machine, (b) sonotrode tip and anvil, and (c) side and top views of the multi-layered USW configuration.

Weld energy was selected as the input variable for the study of weld formation from screening tests performed prior to this research. For welds of 3CC, weld energy ranged from 1200 J to 2800 J with an increment of 200 J, while clamping pressure and vibration amplitude was set as 20 psi and 65 µm, respectively. A set of samples welded at 600 J was produced to investigate early stages of the process when not all interfaces were bonded. In the 3CC study, all settings were repeated 3 times. For 3AC welds, the influence of process parameters was investigated, and therefore three process parameters were varied in this study. To reduce the number experiments for the parametric study, a central composite design (CCD) was applied. The process conditions investigated are summarized in Table 3.2. The setting with clamping pressure as 25 psi, vibration amplitude as 40 µm, and weld energy as 500 J was selected as the center point. All interfaces of the 3AC were tested individually, and 9 replicates were made at each setting for USW. To avoid the effects of experimental sequence, the weld sequence was randomized.

Table 3.2 Experimental Design Matrix

Test Number	Weld Energy (J)	Clamping pressure (psi)	Vibration Amplitude (µm)
1	164	40	25
2	300	35	20
3	300	35	30
4	300	45	20
5	300	45	30
6	500	32	25
7	500	40	17
8	500	40	25
9	500	40	33
10	500	48	25
11	700	35	20
12	700	35	30
13	700	45	20
14	700	45	30
15	836	40	25

3.2.2 Sample Preparation and Microscopy

The development of the weld as a function of weld energy was investigated in samples cross-sectioned at A-A, as shown in Fig. 3.1 (c). Microscopy, including optical microscopy (OM), scanning electron microscope (SEM), energy-dispersive X-ray spectroscopy (EDX), and electron backscatter diffraction (EBSD) were employed to inspect the interfacial bonding conditions and microstructures. The microscopic characterizations were correlated to the weld quality, which was described by lap-shear load carrying capacity and the failure mode of each interface, thus permitting the assessment of the joint at different stages during the weld formation.

3.2.3 Weld Performance Evaluation

Lap-shear tests were used to evaluate the weld quality. The load carrying capacity was used to describe the weld strength. The test was performed using an MTS Instron testing machine with a 5 kN load cell. During the test, a welded sample was mounted between a fixed lower grip and a movable upper grip, as shown in Fig. 3.2. The cross-head speed was set to 2 mm/min. Each interface was measured individually, as detailed in Figs. 3.2 (b) to (d). The top and bottom interface were tested in USW of 3CC and all interfaces were tested in USW of 3AC. During the test, the neutral axis was not perfectly aligned through the interface, but the influence of the eccentricity caused by the misalignment was not significant because the workpieces were thin, and comparisons were only made between same interface. Each measurement had 3 replicates.

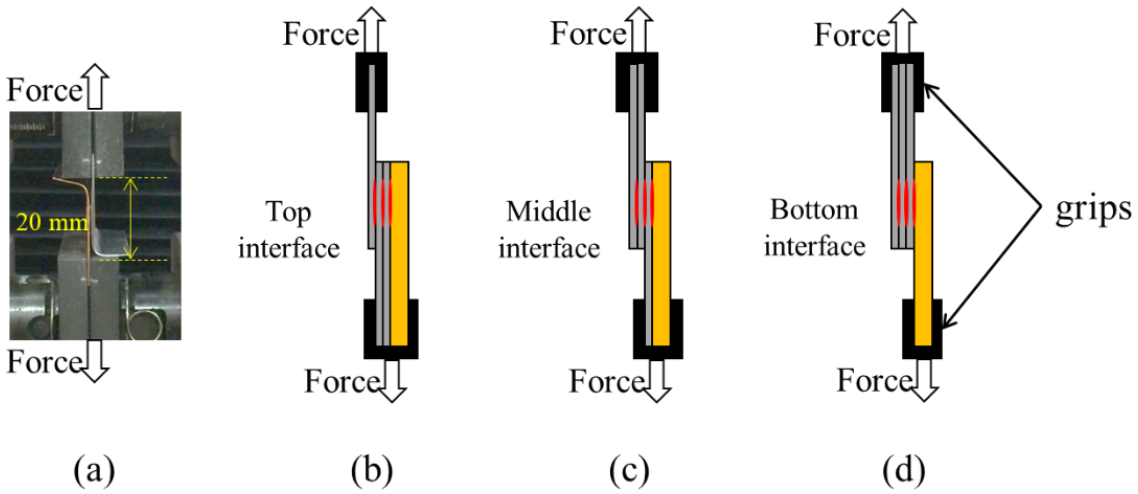

Figure 3.2. Lap-shear test: (a) photo image and schematics for (b) top interface, (c) middle interface, and (d) bottom interface.

3.3. Bonding Mechanisms and Weld Formation

This section presents the study of the bonding mechanisms and weld formation at individual interfaces, as well as from interface-to-interface in ultrasonically welded 3AC and 3CC configurations. The samples produced at different weld energies were cross-sectioned and examined using microscopy. To investigate the microstructures, some sample were etched using Keller's reagent [12], while other samples were polished using Focused ion beam (FIB) in SEM. The metallurgical characteristics and corresponding weld strength are discussed.

3.3.1 Microstructural analysis and mechanical tests of 3CC

Weld samples produced at weld energies ranging from 1200 J to 2400 J were cross-sectioned at A-A, as illustrated in Fig. 3.1 (c). Representative OM images of these samples are presented in Fig. 3.3. The crest and valley regions described in Section 3.2.1 are marked in Fig. 3.3 (b). As shown in Fig. 3.3 (a), a clear non-bonded gap can be observed at the bottom interface

in samples produced at 1200 J. As weld energy increases, the visible gap diminishes and closes from the center to the edges of the weld zone, as shown in Figs. 3.3 (b) and (c). When the weld energy is over 1600 J, there is no visible gap at the bottom interface, and the size of the bond area remains almost unchanged, shown in Figs. 3.3 (d) to (f). In comparison, no visible gaps can be observed at the top and the middle interface in all studied conditions. The bonding conditions in Fig. 3.3 indicate that the top and middle interfaces form bonds prior to the bottom interface in this study.

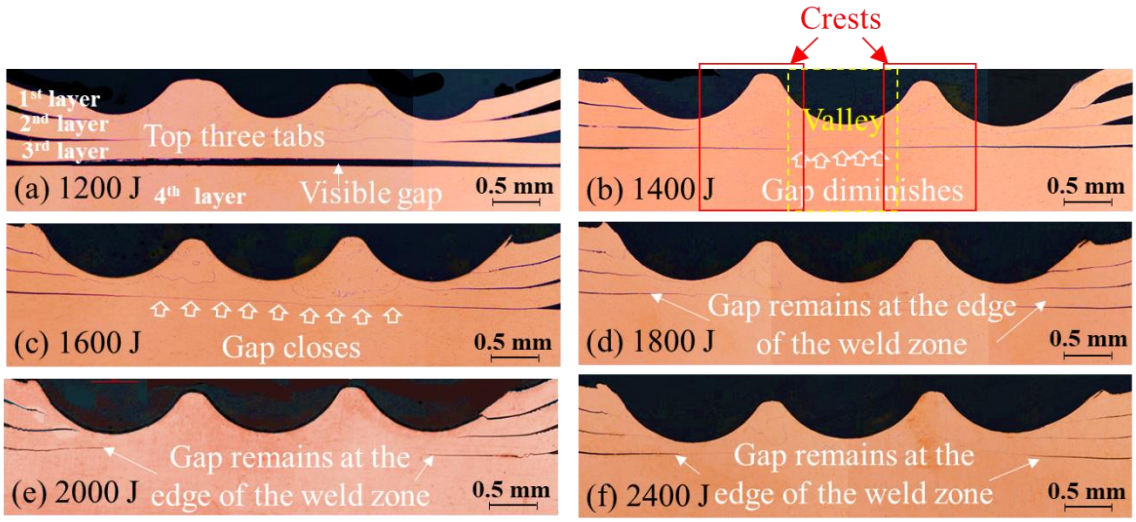

Figure 3.3. Optical microscopic images of samples welded at cross-section A-A at (1) 1200 J, (b) 1400 J, (c) 1600 J, (d) 1800 J, (e) 2000 J, and (f) 2400 J.

Bonding Mechanisms of 3CC Ultrasonic Weld

The micro-level bonding conditions were studied using OM and SEM in the crest region. The results of a sample welded at 1600 J are shown in Fig. 3.4. The OM image of the entire region is presented in Fig. 3.4 (a). The Ni-coating is marked as dashed black line in the figure. A clear line with minimal undulations and a line with severe undulations can be seen at the bottom and the middle interface, respectively. No visible continuous bonding line can be found at the top interface.

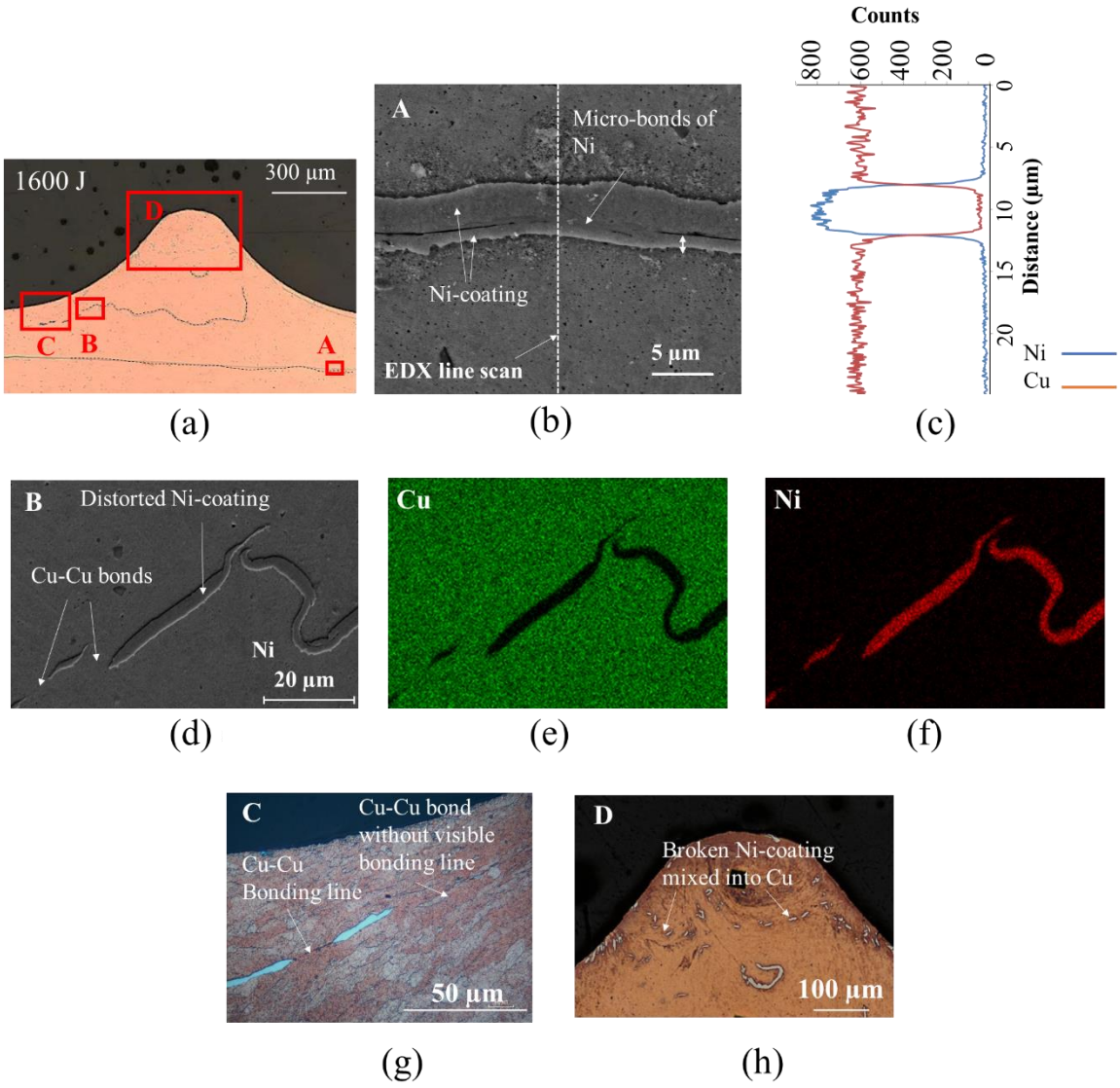

Figure 3.4. Crest region of sample welded at 1600 J, with (a) OM image, (b) SEM image at area A, (b) EDX composition scan along dashed line in area A; (d) SEM image at area B, (e) EDX composition mapping of Cu in area B, (f) EDX composition mapping of Ni in area B, (g) bonding details at etched area C, and (h) bonding details at area D.

The SEM image at area A is presented in Fig. 3.4 (b) and shows that local bonds are formed. An EDX composition scan was performed along the dashed line, and the results are presented in Fig. 3.4 (c). The elemental spectrum analysis along the scanning line in Fig. 3.4 (c) confirms that

the bonds are formed between Ni-coatings at the faying surfaces. The details of bonding at the middle interface are studied in areas B and C. The SEM image of area B in Fig. 3.4 (d) shows co-existence of Cu-Cu bonds and severely distorted Ni-Ni bonds. Mechanical interlocking forms at the severely distorted Ni-Ni bonding lines. No obvious diffusion between Cu and Ni can be found in the studied area according to the EDX mapping shown in Figs. 3.4 (e) and (f). Figure 3.4 (e) shows the bonding details at the etched area C. A visible Cu-Cu bonding line can be observed between two pieces of discontinuous Ni-coatings, and further mixture in Cu without clear bonding lines is observed in larger Cu-Cu bonding area. A study of area D in Fig. 3.4 (h) implies that the broken Ni-coatings are mixed into the 1st and 2nd Cu layers, the bonding line at the top interface is thus difficult to discern. The information provided by Fig. 3.4 indicates that bonding among Ni-coated Cu sheets consists of metallurgical adhesion, interlocking and material mixture.

Interfacial Weld Formation in 3CC

The development of bonding at all interfaces with varying weld energy are shown in Fig. 3.5. The results imply that all interfaces experience similar weld development at different weld energies. At the top interface, an undulated Ni-Ni bond starts to form at 600 J, as shown in Fig. 3.5 (a). As weld energy increases, the Ni-Ni bond distorts and breaks. The broken Ni-Ni bonds develop into small segments and mix into the base material at the end of the Ni-Ni bonding line, as shown in Figs. 3.5 (b) and (c). When weld energy is over 1400 J, most Ni-Ni bond segments are mixed into the base material forming second phase particles, and no obvious interface line can be identified, as shown in Fig. 3.5 (d). In comparison, a Ni-Ni bonding line with minimum undulations is found at the middle interface in sample welded at 600 J, as illustrated in Fig. 3.5 (a). The degree of undulation of the Ni-Ni bonding line increases at higher weld energy levels, as

shown in Fig. 3.5 (b). The bonding line further distorts and breaks as weld energy increases, as shown in Figs. 3.5 (d) to (f). Similarly, the bottom interface initiates bonding at 1400 J, starting with minimum undulated Ni-Ni bond, then develops into an undulated Ni-Ni bond at higher weld energies, as presented in Figs. 3.5 (d) to (f). A higher degree of undulation in the Ni-Ni bond and even the Cu-Cu bond can be found in the valley region at the bottom interface in the sample welded at 2400 J, as shown in Fig. 3.5 (g). The figure also indicates broken Ni-Ni bonds of the three top tabs mix and diminish into the base material in the valley region.

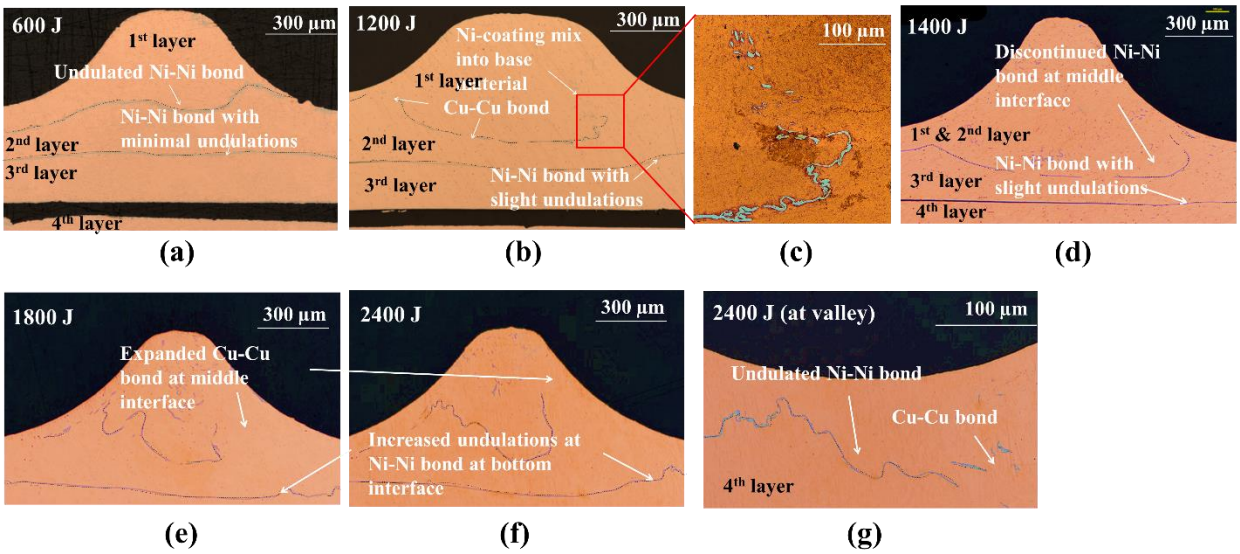

Figure 3.5. Detailed OM images of crest region in welds made at (a) 600 J, (b) 1200 J, (c) 1200 J with higher magnification, (d) 1400 J, (e) 1800 J, and (f) 2400 J, and OM image of valley in weld made at 2400 J.

In summary, all interfaces in USW of a 3CC joint develop the interfacial bonding in the same manner but at different times. Four stages can be summarized in the weld formation of Ni-coated Cu sheets. In the first stage, Ni-coatings of the faying surfaces metallurgically bond as the contaminants of the surface are dissipated, surface asperities flattened, and intimate metal-to-metal contact forms under pressure. Minimum interfacial undulations form in this stage because of the relatively low temperature and work hardening of the material [6]. In the second stage, temperature

elevates and reduces the flow stress of the material. Obvious interfacial undulations at the Ni-Ni bonding line initiate and develop under the synergy of normal and oscillating shear stress. As the process proceeds, in the third stage, the Ni-Ni bonding line experiences extreme distortion and breaks, allowing direct intimate contact of Cu surfaces and formation of Cu-Cu bonds. In this stage, the interfacial joint is a combination of undulated Ni-Ni bonds and Cu-Cu bonds. As the process further develops to the fourth stage, the segmented Ni-Ni bonding lines break into small particles and mixed into the base material. The top interface quickly develops from the second stage to the fourth stage from 600 J to 1400 J according to the studied samples and remains at the fourth stage at higher weld energy levels. The middle interface develops from the first stage at 600 J, develops to the third stage at 1400 J, and maintains the third stage in the crest regions while it changes to the fourth stage in the valley regions for higher weld energy levels. The bottom interface slowly initiates the first stage at 1400 J and develops to the second stage in the crest region and third stage in the valley regions as weld energy increases. Such formation sequence indicates that the top interface is bonded prior to the other interfaces, and the bottom interface forms the bond last.

Lap-Shear Performance of 3CC

A lap-shear test was performed on the top and bottom interfaces of ultrasonically welded 3CC joints. The maximum shear load carrying capacity (i.e. weld strength) for a given weld energy is presented in Fig. 3.6. The results indicate that weld strength at the top interface slightly increases from 300 N to 400 N as weld energy changes from 1200 J to 2800 J. The failure mode at the top interface is circumferential failure for all studied conditions, as shown in the samples welded at 1400 J and 2400 J. Within the tested energy range the top interface changes from the third to the

fourth stage of the weld formation. In comparison, the weld strength at the bottom interface is much more sensitive to the change of weld energy and can be classified by three different parts. The first part shows a rapid increase in weld strength from 1200 J to 1600 J, where Ni-Ni bond with minimum undulations form and expand over the weld zone. The second part finds a gradual increase of the weld strength from 1600 J to 2000 J, where the interfacial gap diminishes in the weld zone and slight undulation initiates in Ni-Ni bond line. The failure mode in the first two stages is interfacial separation. The third part, when weld energy is over 2000 J, there is a minor increase in weld strength and pull-out from the base material dominates the failure mode. According to the OM images in Fig. 3.5, more severe undulations of the Ni-Ni bond develop, with mechanical interlocking formation and Cu-Cu bonds formation where the Ni-Ni bonding line breaks. The three parts of the lap-shear performance of the bottom interface matches with the weld formation stages the bottom interface experiences as weld energy increases. The results imply that weld strength rapidly increases in the first stage of the weld formation, gradually increases in the second stage, and tends to be more constant in the last two stages when failure mode transfers to base material tear or circumferential failure.

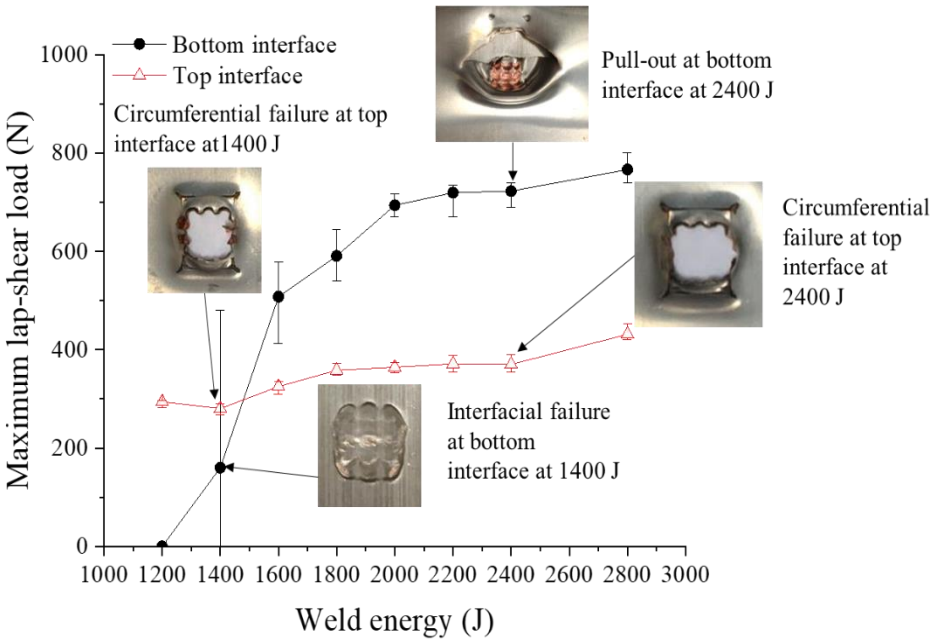

Figure 3.6. Lap-shear results vs. weld energy for the top and bottom interfaces of 3CC.

Summary

The analysis of the microstructures and the corresponding weld strength shows that the weld among Ni-coated Cu sheets consists of Ni-Ni bonds, mechanical interlocking, Cu-Cu bonds, and material mixture, regardless of the layer thickness and interface location. Four weld formation stages can be characterized as the weld proceeds: 1) In the first stage, the Ni-coating at the contacted surface initiate bonds and forms a bonding line with minimum undulations, and weld strength rapidly increases. 2) In the second stage, the bonded Ni-coating distorts under the influence of clamping pressure and oscillatory shearing, moderate undulations form, and weld strength gradually increases. 3) In the third stage, excessive plastic deformation breaks the Ni-Ni bond, allowing bond formation between Cu at the interface, and the segmented Ni-Ni bonds move with the material flow, which forms macro-level mechanical interlocking. 4) In the fourth stage,

as the process continues, Cu-Cu bonds grow with more material mixture, and Ni-Ni bonds break into tiny pieces that mix into Cu, forming second phase particles.

Although experiencing a similar weld formation process, different interfaces reach each stage at a different weld energy level. In this study, the weld develops first at the top interface, and may even skip the first stage due to the plastic deformation of the metal sheet. Then the middle interface develops a weld, followed by weld formation at bottom interface at higher weld energy. A monotonically sequential weld propagation from the top interface to the bottom interface can be observed in USW of 3CC.

3.3.2 Microstructural analysis and mechanical tests of 3AC

Samples of the 3AC joint were ultrasonically welded at 164 J, 500 J, and 836 J with clamping pressure at 25 psi and vibration amplitude at 40 μm. The samples were cross-sectioned and etched at A-A (in Fig. 3.1 (c)). The OM images of these samples are shown in Fig. 3.7. Macro-level undulations are observed in all interfaces, as both pure Al and Cu are malleable materials. The level of interfacial undulations among the Al tabs increases as the weld proceeds and becomes difficult to identify visually in the sample welded at 836 J. Visible gaps at the Al/Cu interface can be found in samples produced at 164 J and 500 J, which diminishes when higher weld energy is used. Gaps can also be found at the top and the middle interface at crest regions in the samples welded at 164 J and 500 J, as indicated in Figs. 3.7 (a) and (b). No visible gap is observed in the sample welded at 836 J, but the Al tabs are extremely thinned and even penetrated at valleys, as shown in Fig. 3.7 (c). Details of local bonding conditions in areas A to D are discussed in the following sections.

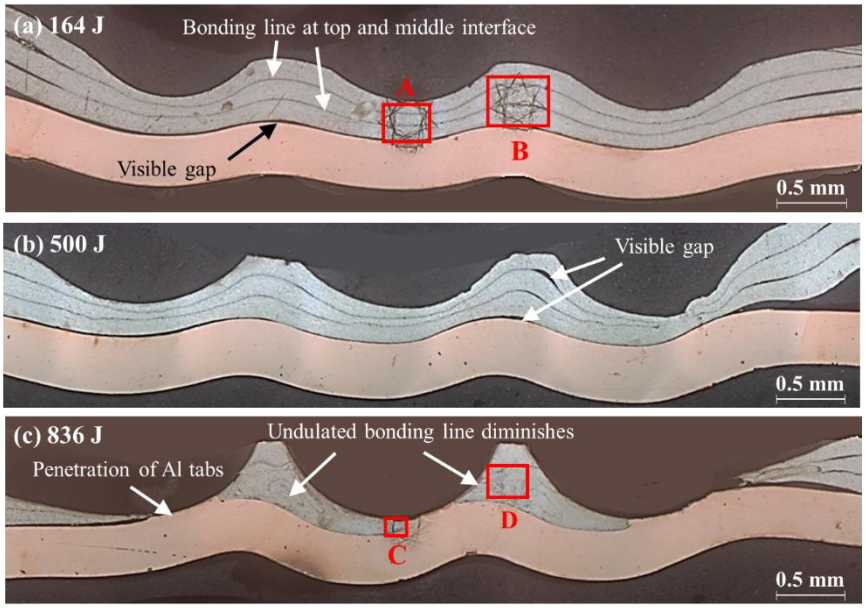

Figure 3.7. Optical microscopic images of samples welded at cross-section: A-A at (1) 164 J, (b) 500 J, and (c) 836 J.

Bonding Mechanisms in Al Tabs

The bonding mechanisms in the 3AC joint, including bonding between Al and Cu, and Al-to-Al will be discussed in this section. OM images with higher magnification are shown in Fig. 3.8. Figures 3.8 (a) and (b) show the valley and crest region of the sample welded at 164 J. Segmented Al-Al bonding lines with micro-level undulations could be found at the top and the middle interface, while an Al-Al mixture can be found between segmented bonding lines, as indicated in Fig. 3.8 (a). In comparison, bonding lines in the crest region are smoother with minimum segmentations and visible gaps, as shown in Fig. 3.8 (b). The smooth bonding lines extensively distort in the crest area in the sample welded at 836 J, resulting in bulk material mixture, as presented in Fig. 3.8 (c). The results suggest that material mixture with micro-level undulations contribute to the bonding among Al tabs, and bulk material mixture dominates the bonding at higher weld energy.

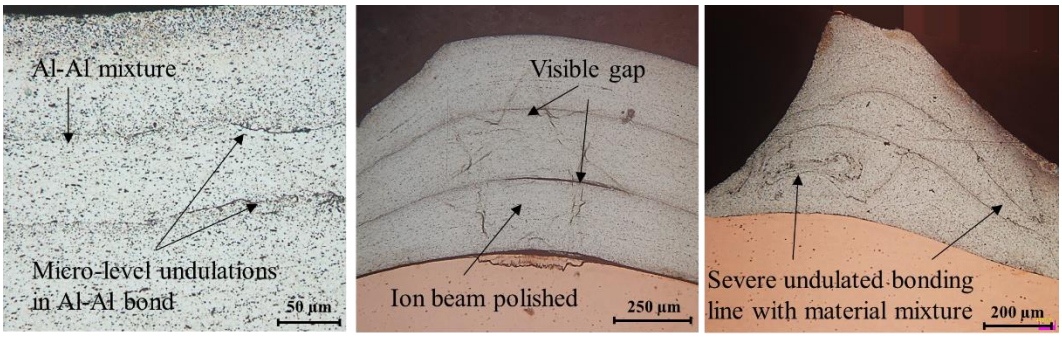

Figure 3.8. OM images with higher magnification (a) at valley of 164 J sample, (b) crest of 164 J sample, and (c) crest of 836 J sample.

The microstructures in area A to D (in Fig. 3.7), which respectively represent the valley and crest area in samples welded at 164 J and 836 J, were closely characterized by EBSD shown in Fig. 3.9. The grain size, varying by location and weld energy, are presented in Fig. 3.9 (a). The grain size in the crest area (15 to 30 µm) is much larger than that in the valley area (3 to 5 µm) in a low energy welded sample, implying recrystallization in the valley. As weld energy increases to 836 J, the grain size in the crest region dramatically drops to about 7 µm, indicating recrystallization as weld energy increases. In comparison, the grain size in the valley gradually decreases to 1.5 µm possibly under the synergy of plastic deformation and increased temperature [6]. Noticeably, no grain exhibits a high misorientation angle in the studied area, even at the weld interface, as shown in fig. 3.9 (b). Previous studies [20-21] confirmed that the interfacial temperature is typically lower than the melting point of Al (~ 657 ºC) [17]. Therefore, as a solid-state welding process, the recrystallization in the valley is driven by plastic deformation with high strain rate.

Inverse pole figure (IPF) maps are presented in Figs. 3.9 (c) to (f). In Fig. 3.9 (c), a sample made at 164 J, the valley area exhibits uniformly distributed grains without distinguishable interfaces. In comparison, clear top and middle interfaces can be identified in the crest region,

where the visible gap closes, as shown in Fig. 3.9 (d). At higher weld energy, further deformation and concurrent recovery due to a temperature rise allows the grain size to decrease slightly in the valley area. The black spots marked in Fig. 3.9 (e) represent extreme deformation that cannot be characterized using current equipment in this study. The white spots in the same figure are iron precipitations from the pure Al according to element spectrum analysis. Besides, the crest area in the same sample exhibits fully recrystallized grains without distinguishable interfaces, as shown in Fig. 3.9 (f).

An analysis of the microstructure via OM and EBSD indicate bulk dynamic recrystallization through all tabs is the dominant bonding mechanisms in Al tabs in this study. The two faying surfaces are clamped together and form initial metallic adhesion. Severe plastic deformation introduces micro-level undulations and provides a driving force for recrystallization. As the weld process proceeds, gaps at the faying surfaces are filled by deformed material and interface diminishes due to grain recrystallization, and bulk material mixture occurs.

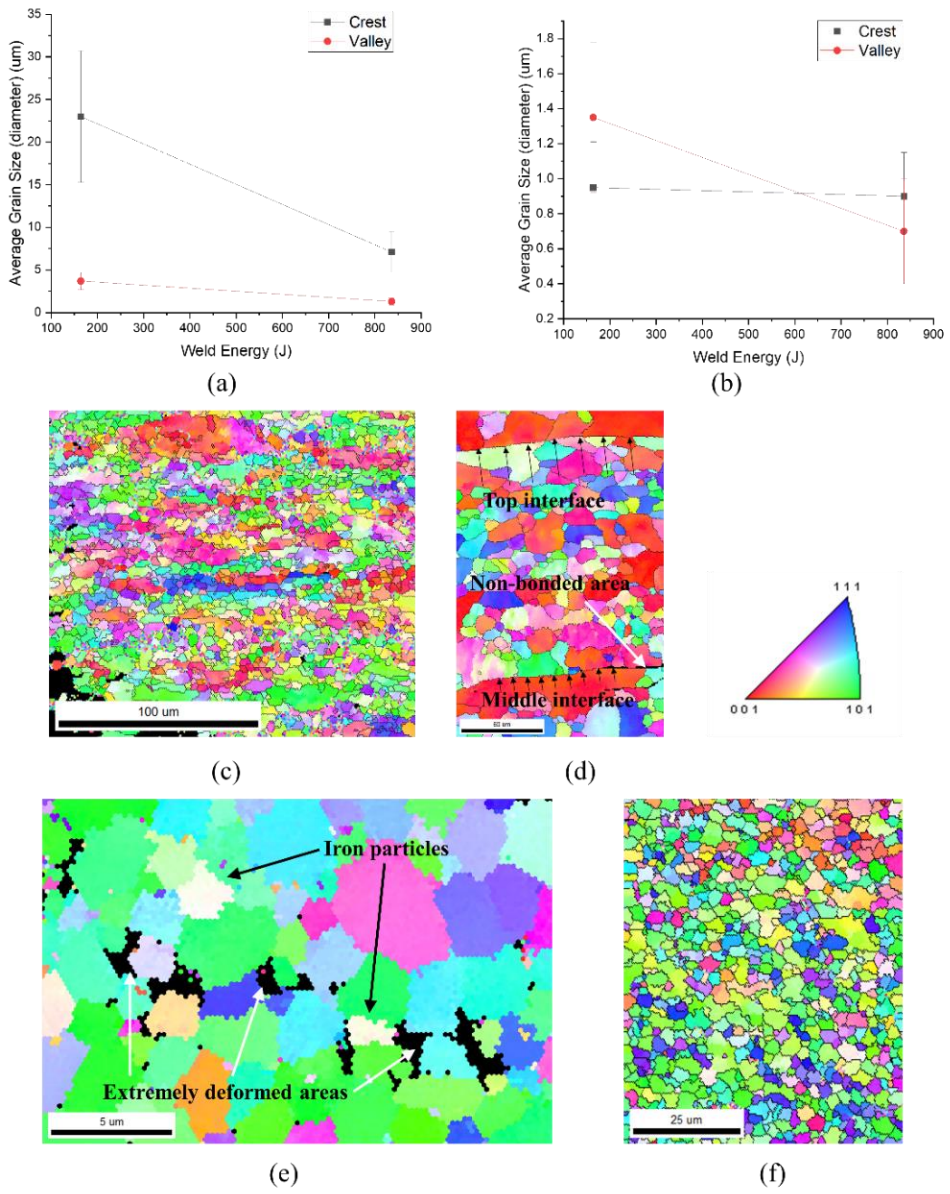

Figure 3.9. Grain structure analysis at valley and crest area for samples welded at 164 J and 836 J: (a) change average grain size, (b) change of grain average misorientation, IPF of (c) area A, (d) area B, (e) area C, and (f) area D.

Bonding Mechanisms between Al and Cu

To characterize the bonding between Al and Cu interface, EDX line scanning was used for the detection of chemical composition around area C marked in Fig. 3.7 (c). The OM image of

area C with higher magnification is presented in Fig. 3.10 (a). A clear Al/Cu interface line can be seen in this area, and the clear line becomes severe undulated at the location where penetration occurs, implying local severe plastic deformation. Both the smooth and undulating areas were studied by EDX line scanning marked as Line a and Line b. The atomic distribution of the Al and Cu elements along Line a is shown in Fig. 3.10 (b). The result indicates a thin diffusion layer with around 6 μm thick, proving interfacial diffusion in Al/Cu bonds. The diffusion layer becomes thicker (~ 12 μm) in the area with severer deformations, as the EDX scanning along Line b shows in Fig. 3.10 (c). Within the diffusion layer, there also exists an around 3 μm plateau region with constant atomic percentage of Al (around 90%) and Cu (10%). According to the Al-Cu phase diagram [17], such constant elemental composition implies a mixture of pure Al and $CuAl_2$. Previous study by Satphathy *et al.* [16] suggests that the interfacial temperature of ultrasonically welded Al 1100 and Cu 110 was no higher than 330 ºC, which is much lower than the melting temperature [17]. Therefore, the formation of the IMCs is more likely caused by severe plastic deformation. Interfacial diffusion in USW of Al and Cu has also been reported by Zhang *et al.* [18], who investigated the nanostructure at the interface of ultrasonically welded Al and Cu by transmission electron microscopy (TEM) and found a ~ 10 nm thick transition layer composed of amorphous phase and nanocrystallites. Both previous studies and the analysis of EDX suggests that the bonding between Al and Cu takes place by interdiffusion enhanced by severe plastic deformation. The variation of diffusion layer indicates non-uniform welding diffusion along the bonding line.

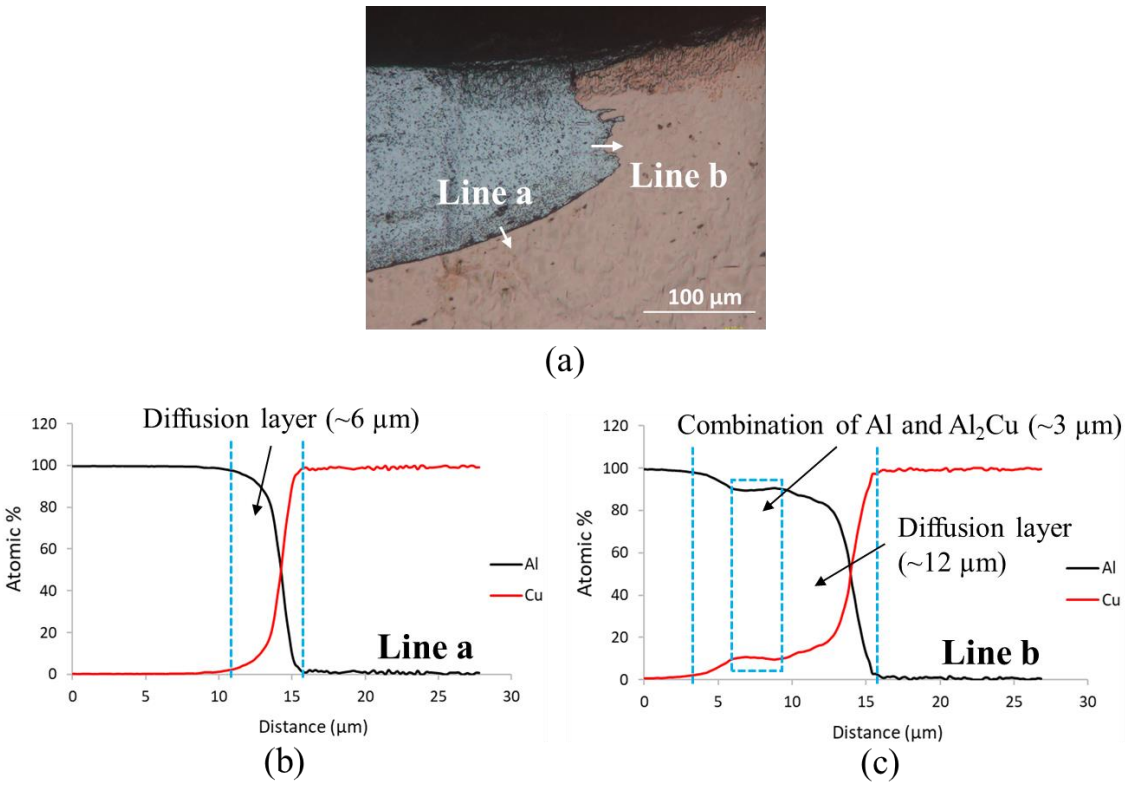

Figure 3.10. EDX analysis at Al/Cu interface in sample welded at 836 J: (a) OM image of area C in marked in Fig. 3.7 (c), (b) element distribution along Line a, and (c) element distribution along Line b.

Weld formation and Lap-Shear Performance of 3AC

The weld formation from one interface to another is not clear in USW of 3AC according to the microstructure evolution. To further understand the weld propagation in 3AC, some factors representing weld formation are required. As implied in the cases of 3CC in Section 3.3.1, weld formation has a strong relationship with the corresponding lap-shear performance, including weld strength and failure mode. Therefore lap-shear test results can be used as an index depicting the weld formation at single interface and from interface to interface especially when microstructural analysis does not show a clear sequence. This hypothesis is not only supported by study of 3CC but also proved by some other researchers [6, 14, 22]. As interfacial weld develops, the weld strength represented as weld load carrying capacity typically increases to a maximum value as

bond grows and gradually decreases as extreme thinning occurs. Moreover, the failure mode generally transfers from interfacial separation to partial pull-out to circumferential as weld develops, and the maximum strength is typically achieved when partial pull-out of the base material predominates.

The lap-shear performance of all interfaces in USW of a 3AC joint made were measured. The maximum shear load carrying capacity (i.e. lap-shear strength) of welds made by 25 psi, 40 μm, and 164 J to 836 J are presented in Fig. 3.11 (a). As weld energy increases, the lap-shear strength gradually decreases at the top interface, gradually increases at the middle interface, and considerably increases at the bottom interface. Four different failure modes were observed in the studied case, including interfacial failure, one-sided pull-out, multi-sided pull-out, and circumferential fracture, designated as 'IF', 'PO1', 'PO2', and 'CF', respectively, as illustrated in Fig. 3.11 (b). As weld energy increases from 164 J to 836 J with constant pressure and amplitude, the failure mode ranges from PO1 to PO2 and to CF at both the top and the middle interface, while the failure mode at the bottom interface changes from IF to PO2 and finally to CF. The decline of the weld strength and tear or fracture of the base material at the top interface implies it experiences a later stage of the weld development within the studied energy range. In comparison, the weld at the middle interface becomes stronger with pull-out failure or circumferential failure, which indicates a middle to slight late stage of a weld development at the middle interface. The bottom interface undergoes a rapid climb of the weld strength with failure mode changing from IF to CF, suggesting a transition from early stage to the middle or slight late stage of the weld development.

The lap-shear performance of the interfaces in 3AC within the studied range indicates that the top interface develops weld faster than the middle and the bottom interface do, while the middle interface slightly develops faster than the bottom interface. Such sequence suggests a top to bottom

weld propagation in USW of 3AC. However, the weld strength and failure mode are affected by sample geometries, material properties, and bonding strength. Even a weak bond can also experience pull-out failure if the workpiece is very thin. The microstructures at the top and the middle interface do not exhibit significant difference for all studied conditions, and non-bonded areas are observed at all interfaces in the cross-sectioned samples. Therefore, these is no solid evidence proving the aforementioned weld propagation in 3AC.

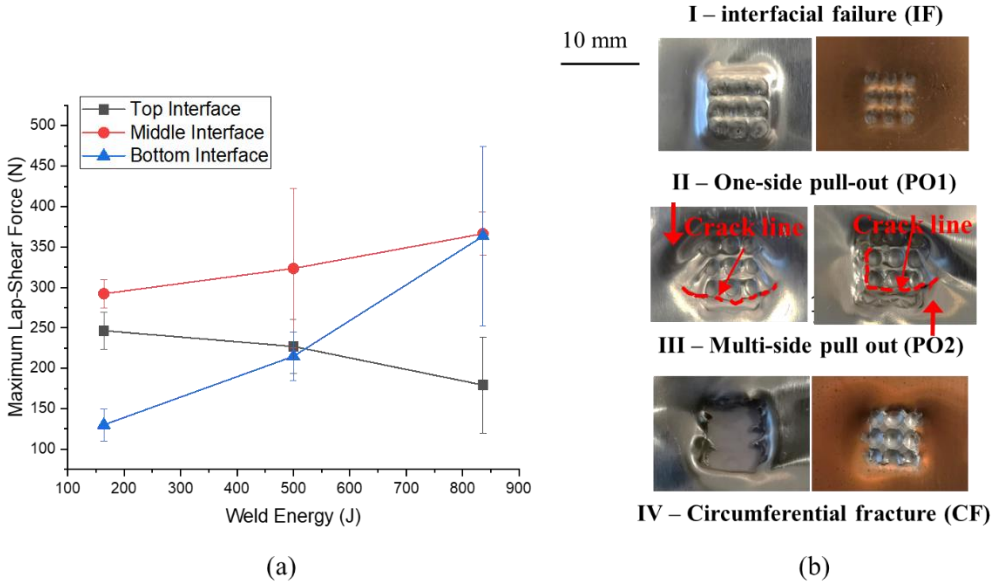

Figure 3.11. Lap-shear performance results: (a) weld strength vs. weld energy for all interfaces of 3AC, (b) 4 different failure modes.

Summary

Multiple microscopy methods, including OM, SEM, EDX, and EBSD were applied to analyze the interfacial bonding conditions in USW of a 3AC joint. The results suggest that the bonding among Al tabs is contributed by metallic adhesion at low and moderate weld energy and bulk material mixture at high weld energy. The formation of the bond is dominated by dynamic recrystallization under severe plastic deformation with high strain rate. The bonding between Al

and Cu is mainly completed by non-uniform interfacial diffusion enhanced by severe plastic deformation and rising temperature. IMCs form in the area with excessive material distortion.

The results of both the microstructure analysis and the lap-shear performance in the 3AC joint suggest that bonds form in valley regions prior to crest regions. The lap-shear performance of all interfaces implies a weld propagation from the top to the bottom. However, considering the microstructure evolution and geometrical influence on lap-shear performance, it is difficult to identify the exact weld formation sequence.

3.4. Influence of Process Parameters

This section investigates the influence of process parameters in USW of the 3AC joint. The effects of clamping pressure and vibration amplitude on weld formation are firstly discussed, followed by a study of the main effects of process variables on weld strength at all interfaces.

3.4.1 Influence of clamping pressure and vibration amplitude on weld formation

Both clamping pressure and vibration amplitude influence the weld formation in USW. Cross-sectional OM images of samples made at 17 psi, 25 psi, and 33 psi clamping pressure levels with constant weld energy of 500 J and a vibration amplitude of 40 μm are presented in Figs. 3.12 (a) to (c), respectively. The interfacial bonding shows no obvious difference under different clamping pressures. The weld strengths of different interfaces are presented in Fig. 3.12 (d). It can be seen that the weld strength at the middle interface decreases with increasing clamping pressure, while that at the top and the bottom interfaces are relatively constant. Although the maximum weld strength at the middle interface is achieved with the lowest clamping pressure, its large variation indicates that the performance is considerably inconsistent at that condition.

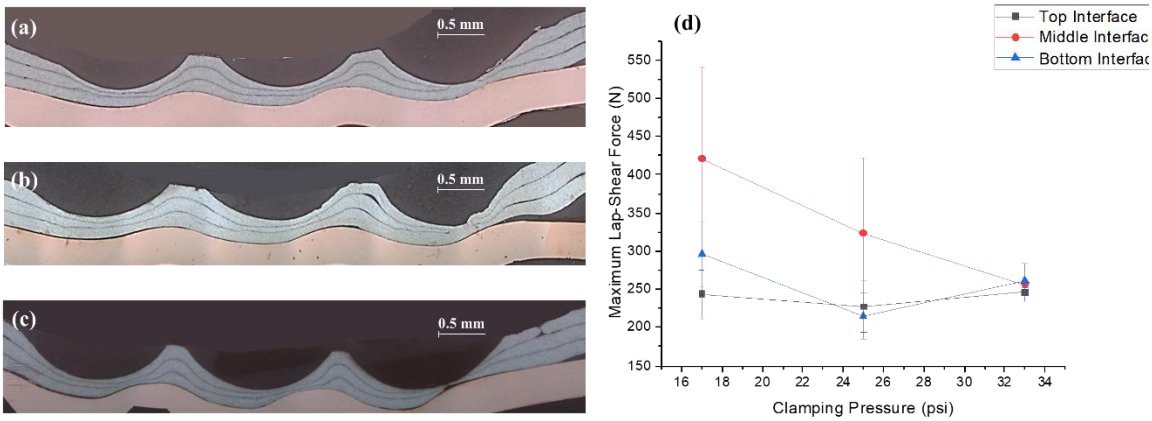

Figure 3.12. Influence of clamping pressure (a) 17 psi, (b) 25 psi, (c) 33 psi, and (d) maximum lap-shear force at different interfaces change with clamping pressure.

Figure 3.13 shows the influence of vibration amplitude. Vibration amplitudes at 32 µm, 40 µm, and 48 µm were studied with constant weld energy of 500 J and clamping pressure of 25 psi. The cross-sectional images show that excessive vibration amplitude results in extensive deformation of Al tabs, where even penetrations can be observed. There is no obvious difference of welding conditions in samples welded at 32 µm and 40 µm. The weld strength at the bottom interface drops when amplitude changes from 32 µm to 40 µm and increases as the amplitude increases to 48 µm. However, the bottom interface exhibits extremely unsteady weld performance when a low vibration amplitude is used, and the maximum weld strength is achieved using 48 µm, although penetration occurs. In comparison, the weld strength of the middle interface is relatively constant as the vibration amplitude changes. The weld strength at the top interface monotonically decreases with increasing vibration amplitude.

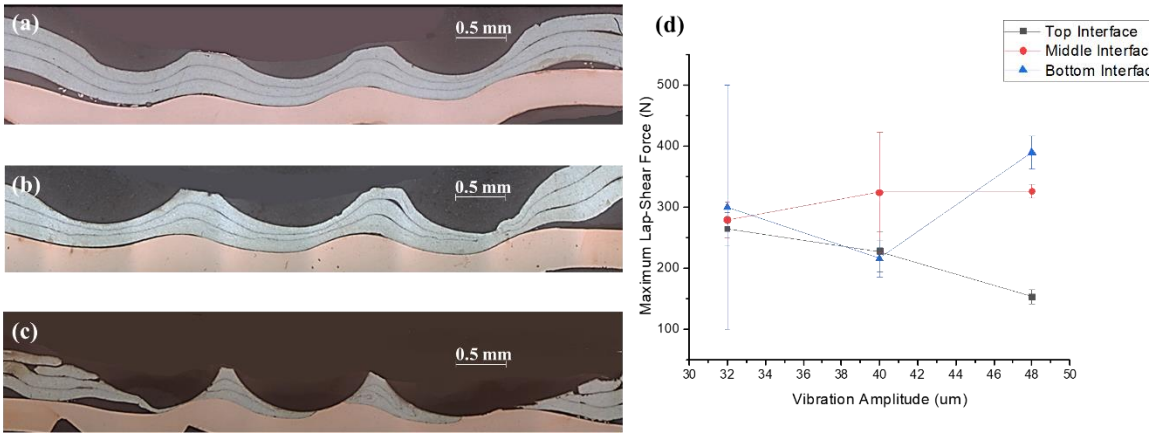

Figure 3.13. Influence of vibration amplitude (a) 32 µm, (b) 40 µm, (c) 48 µm, and (d) maximum lap-shear force at different interfaces change with vibration amplitude.

An ultrasonic weld is made under the synergy of clamping pressure and oscillating interfacial shearing. The metals sheets deform and are clamped closely between the sonotrode tip and anvil, forming initial contact at all interfaces. The vibration of the sonotrode tip initiates motion of the top layer and forces the motion of other layers. The constraint of the stationary anvil provides an opposite driving force, which enables relative motion at all interfaces. The normal and tangential forces at the faying surfaces eliminates the oxide layer and contaminants, resulting in local bond formation. As the process proceeds, temperature increases due to interfacial friction and bulk plastic deformation, which stimulates interfacial interactions and enhances interfacial bonding. Higher clamping pressure brings more intimate contact in the early stages of the welding process, but also impedes the relative motion at the interface. A larger vibration amplitude accelerates the surface cleanup at beginning of the process, but leads to more heating at the interfaces as the process proceeds, and can introduce excessive material flow and softening when the input energy is high.

The cross-sectional images of welds made at different clamping pressure and vibration amplitude show a significant influence of high vibration amplitude on metal sheet deformation.

While the clamping pressure slightly boosts metal sheet deformation, the reaction of the lap-shear performance at each interface to these parameters varies. The weld strength at the middle interface is most sensitive to the change in clamping pressure, but little influenced by the vibration amplitude. Larger vibration amplitude improves the weld strength at the bottom interface but has negative impact to the top interface.

3.4.2 DOE analysis on effects of weld parameters

To understand further the impact of process parameters on the weld at all interfaces in USW of a 3AC joint, a central composite design (CCD) of experiments (DOE) was applied to this study [23]. The experimental matrix is depicted in Table 3.2 in Section 3.2. Each parameter had 5 levels and 15 conditions and were studied with 3 replicates at each interface.

Response surface analysis was performed to investigate the significance of process parameters and their interactions on the lap-shear strength of each interface. A confidence level of 95% was selected to determine the significance of a factor. The response surface analysis was performed twice for each interface. The first time includes all process parameters, their second order terms, and their interactions, while the second time only includes the terms with p-value lower than 0.05 and the corresponding prime term if the p-value of that term was higher than 0.05. The results are summarized in Table 3.3. As detailed in Table 3.3, the strength of the top interface is mostly influenced by weld energy, vibration amplitude, their interaction, and the interaction of energy and clamping pressure. While the strength of the middle interface is most sensitive to weld energy, and interaction of pressure and amplitude. The most important factor influencing the weld strength at the bottom interface is weld energy, vibration amplitude, and its interaction with clamping pressure. The sensitivity analysis indicates that all interfaces are sensitive to weld energy,

but their responses to the other process parameters and their interactions vary from one interface to another.

Table 3.3 Response Surface Analysis of Weld Strength vs. Process Parameters

Factor	P-value		
	Top Interface	**Middle Interface**	**Bottom Interface**
Weld energy (E)	0.001	0.025	0.000
Clamping pressure (P)	0.275	0.151	0.264
Vibration amplitude (A)	0.000	0.905	0.032
E × P	0.023	N/A	N/A
E × A	0.000	N/A	N/A
A × P	N/A	0.017	0.007

(Note: N/A indicates a tern with large p-value that does not significantly influences the result)

An analysis of variance (ANOVA) of main factors versus weld strength of each interface were performed and the results are plotted in Figure 3.14. Figure 3.14 (a) confirms that the weld strength at the top interface decreases with both increasing weld energy and vibration amplitude while not significantly affected by the clamping pressure. Figure 3.14 (b) shows that the weld strength at the middle interface positively changes with increasing weld energy and slightly with amplitude and declines as clamping pressure increases. Figure 3.14 (c) reveals that higher weld energy leads to a considerable increase in weld strength at the bottom interface, and weld strength is statistically higher with larger vibration amplitude. A decreasing tendency can be found for the bottom interface strength with higher clamping pressure, although the influence is not significant.

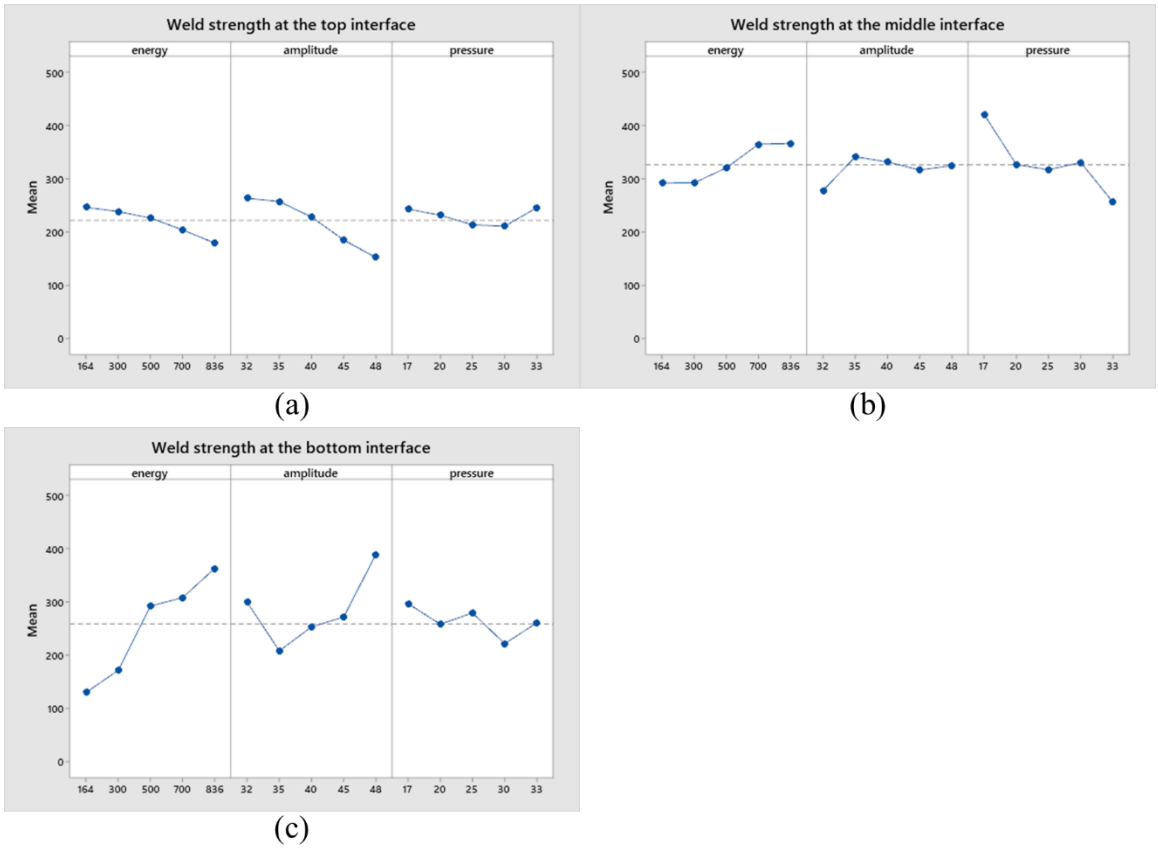

Figure 3.14 Main effects plot for weld energy, vibration amplitude, and clamping pressure at (a) the top, (b) the middle, and (c) the bottom interface.

The statistical analysis of the process parameters versus weld strength implies that the response of weld strength at different interfaces varies and the most significant process parameter is weld energy. The top interface is negatively influenced by weld energy, while both the middle and the bottom interface are positively affected by weld energy. This trend implies that the top interface could form weld prior to the other two interfaces in USW of 3AC, yet the weld formation sequence is influenced by all process parameters.

3.5. Conclusions

The weld formation in multi-layered ultrasonic welding of two types of stack-ups was discussed in this chapter: a 3-layered Al tabs to bare Cu bus-bar (3AC), and a 3-layered Ni-coated Cu tabs to Ni-coated Cu bus bar (3CC). The bonding mechanisms, the weld formation at a single interface and from interface-to-interface were investigated. The influence of the three major process parameters on weld performance was also studied. Specific conclusions are as follows:

1) The bonding between Ni-coated Cu sheets initiates from Ni-Ni bonding with minimum undulations at the contact surfaces. Macro-level undulations in the Ni-Ni bonding lines develop with higher weld energy, and those undulated Ni-Ni bonding lines break and enable Cu-Cu bonding as weld energy increases. Material mixture between Cu-Cu bonding dominates as the process proceeds, and broken Ni-Ni bonds distribute into the base material.
2) A monotonic sequence of weld propagation from the top interface to the bottom interface can be found in USW of 3CC.
3) The bonding between Al tabs is achieved by metallic adhesion due to dynamic recrystallization under severe plastic deformation with a high strain rate. Bulk material mixture occurs if excessive weld energy is used.
4) The bonding between Al and Cu is made by non-uniform interfacial diffusion enhanced by plastic deformation and rising temperature. Severe plastic deformation leads to formation of IMCs ($CuAl_2$).
5) The weld formation among the Al tabs occurs before that of the Al/Cu interface, but the sequence within the Al tabs is difficult to identify in the studied conditions.

6) Weld energy is the most significant process parameter that affects weld strength at all interfaces. At higher weld energy, weld strength at the top interface decreases but increases at the bottom interface. The middle interface is less sensitive to changes in the weld energy.

References

[1] De Vries, E., 2004. Mechanics and mechanisms of ultrasonic metal welding (Doctoral dissertation, The Ohio State University).

[2] Bakavos, D. and Prangnell, P.B., 2010. Mechanisms of joint and microstructure formation in high power ultrasonic spot welding 6111 aluminium automotive sheet. Materials Science and Engineering: A, 527(23), pp.6320-6334.

[3] Zhang, C.S. and Li, L., 2009. A coupled thermal-mechanical analysis of ultrasonic bonding mechanism. Metallurgical and Materials Transactions B, 40(2), pp.196-207.

[4] Arimoto, K., Sasaki, T. and Kim, T., 2019. Ultrasonic Bonding of Multi-Layered Foil Using a Cylindrical Surface Tool. Metals, 9(5), p.505.

[5] Bakavos, D. and Prangnell, P.B., 2010. Mechanisms of joint and microstructure formation in high power ultrasonic spot welding 6111 aluminium automotive sheet. Materials Science and Engineering: A, 527(23), pp.6320-6334.

[6] Lee, S.S., Kim, T.H., Hu, S.J., Cai, W.W., Abell, J.A. and Li, J., 2013. Characterization of joint quality in ultrasonic welding of battery tabs. Journal of Manufacturing Science and Engineering, 135(2), p.021004.

[7] Zhang, C.Q., Robson, J.D. and Prangnell, P.B., 2016. Dissimilar ultrasonic spot welding of aerospace aluminum alloy AA2139 to titanium alloy TiAl6V4. Journal of Materials Processing Technology, 231, pp.382-388.

[8] Watanabe, T., Sakuyama, H. and Yanagisawa, A., 2009. Ultrasonic welding between mild steel sheet and Al–Mg alloy sheet. Journal of Materials Processing Technology, 209(15-16), pp.5475-5480.

[9] Haddadi, F., 2015. Rapid intermetallic growth under high strain rate deformation during high power ultrasonic spot welding of aluminium to steel. Materials & Design, 66, pp.459-472.

[10] Kreye, H., 1977. Melting phenomena in solid state welding processes. Weld. J, 56(5), pp.154-158.

[11] Gunduz, I.E., Ando, T., Shattuck, E., Wong, P.Y. and Doumanidis, C.C., 2005. Enhanced diffusion and phase transformations during ultrasonic welding of zinc and aluminum. Scripta materialia, 52(9), pp.939-943.

[12] Lee, S.S., Kim, T.H., Hu, S.J., Cai, W.W. and Abell, J.A., 2015. Analysis of weld formation in multilayer ultrasonic metal welding using high-speed images. Journal of Manufacturing Science and Engineering, 137(3), p.031016.

[13] Lee, D., Kannatey-Asibu, E. and Cai, W., 2013. Ultrasonic welding simulations for multiple layers of lithium-ion battery tabs. Journal of Manufacturing Science and Engineering, 135(6), p.061011.

[14] Shin, H.S. and de Leon, M., 2017. Mechanical performance and electrical resistance of ultrasonic welded multiple Cu-Al layers. Journal of Materials Processing Technology, 241, pp.141-153.

[15] Das, A., Masters, I. and Williams, D., 2019. Process robustness and strength analysis of multi-layered dissimilar joints using ultrasonic metal welding. The International Journal of Advanced Manufacturing Technology, 101(1-4), pp.881-900.

[16] Wu, X., Liu, T. and Cai, W., 2015. Microstructure, welding mechanism, and failure of Al/Cu ultrasonic welds. Journal of Manufacturing Processes, 20, pp.321-331. Grigorovich, V.K., 1989. The metallic bond and the structure of metals.

[17] Satpathy, M.P., Mohapatra, K.D., Sahoo, A.K. and Sahoo, S.K., 2018, March. Parametric Investigation on Microstructure and Mechanical Properties of Ultrasonic spot welded Aluminium to Copper sheets. In IOP Conference Series: Materials Science and Engineering (Vol. 338, No. 1, p. 012024). IOP Publishing.

[18] Lu, Y., Song, H., Taber, G.A., Foster, D.R., Daehn, G.S. and Zhang, W., 2016. In-situ measurement of relative motion during ultrasonic spot welding of aluminum alloy using Photonic Doppler Velocimetry. Journal of Materials Processing Technology, 231, pp.431-440.

[19] Okamoto, H., Kacprzak, L. and Subramanian, P.R. eds., 1996. Binary alloy phase diagrams. Materials Park, OH: ASM international.

[20] Zhang, Z., Wang, K., Li, J., Yu, Q. and Cai, W., 2017. Investigation of interfacial layer for ultrasonic spot welded aluminum to copper joints. Scientific reports, 7(1), p.12505.

[21] De Vries, E., 2004. Mechanics and mechanisms of ultrasonic metal welding (Doctoral dissertation, The Ohio State University).

[22] Li, H., Choi, H., Ma, C., Zhao, J., Jiang, H., Cai, W., Abell, J.A. and Li, X., 2013. Transient temperature and heat flux measurement in ultrasonic joining of battery tabs using thin-film microsensors. Journal of Manufacturing Science and Engineering, 135(5), p.051015.

[23] Kim, T.H., Yum, J., Hu, S.J., Spicer, J.P. and Abell, J.A., 2011. Process robustness of single lap ultrasonic welding of thin, dissimilar materials. CIRP annals, 60(1), pp.17-20.

[24] Montgomery, D.C., 2017. Design and analysis of experiments. John wiley & sons, Chapter 11, pp. 511

Chapter 4 Influence of Interfacial Undulations on Weld Formation and Performance

Abstract

In the USW process, interfacial undulations caused by plastic deformation influence weld formation by affecting the thermal-mechanical behavior of the material, as well as influences the weld's mechanical performance by affecting local stress and strain under load. A deeper understanding of the influence of interfacial undulation will provide insight and guidance that can enhance process robustness. This study used a fine and a coarse anvil to generate ultrasonic welds with different interfacial undulation levels, and experimentally and numerically compare weld formation and performance. Finite element models were developed to quantitatively investigate weld performance with various interfacial undulations. The results show that stronger bonding with fewer interfacial undulations are made in the early stages of the process, and thus a higher weld strength is achieved when interfacial failure predominates. However, more prominent interfacial undulations help hinder thinning in the base material as the process proceeds, and thus results in a higher weld strength when circumferential failure is observed. Additional simulations compared lap-shear performance of welds with flat and undulated interface assuming same bonding strength and post-weld thickness in the weld area. The results suggest that enhancing bonding strength for undulated cases imporves weld perfromance if interfacial failure dominants.

---

* The contents of this chapter will be submitted to *ASME Journal of Manufacturing Science and Engineering*.

4.1. Introduction

Ultrasonic welding (USW) is a solid-state welding process that creates a bond between metal sheets under static pressure and high frequency vibration. The process has the advantage of creating joints without melting, and is suitable for welding both similar and dissimilar materials. It also has the advantages of requiring low energy consumption and no additional filler materials [1-3]. The application of USW has been rapidly expanding into joining of tabs in electrical battery cells for electrical vehicles and for thin films in various industries such as electronics, semi-conductors, and medical devices.

The formation of bonds in USW has been discussed by various authors. The process stages can be summarized as [4-7]:

1) A compressive relative motion to deform and flatten asperities at the faying surfaces, break oxide layers, disperse surface contaminants, and enable intimate metal-metal contact and localized micro-bonding;
2) The development of localized bonds that expand and close voids due to the collapse of asperities that are softened by frictional heating;
3) The enhancement of interfacial interactions, such as interfacial diffusion [2, 12], metal adhesion and mechanical interlocking [10-11], dynamic recrystallization [4, 8], and local melting [9], by local compression and shearing in the metal sheets, which continue to be softened by heat generated from interfacial friction and plastic deformation, as well as ultrasonic softening; and
4) A condition called over-welding characterized by excessive thinning of the base material, with the eventual penetration of the tool through the base material and

possibly sticking to the tool, and the occasional formation of brittle IMCs at the interface that may appear due to overheating and softening.

In the process of weld formation, several weld attributes have been identified that characterize the stages of the process and its corresponding performance. Lee *et al.* [10] introduced four weld attributes to characterize the weld condition and the weld quality, including bond density, post-weld thickness, weld size, and the thermo-mechanically affected zone (TMAZ). Their study found that bond density continuously increases while the post-weld thickness decreases as the weld process proceeds, and a maximum weld strength is achieved when enough bonding is made without excessive thinning. The study also investigated the TMAZ by measuring the hardness along the longitudinal direction and found the point where hardness returns to that of as-received material. A similar study performed by Shakil *et al.* [13] shows a similar relation between weld attributes and the weld performance. Wu *et al.* [11] estimated the bonding area between Al tabs and Cu bus-bar by measuring residual Al on the mating Cu surface in tested samples, and found a non-linear relationship between bonding area and weld strength. Previous research shows that weld attributes can be used as an index to describe the weld formation and the weld performance.

Although various weld attributes have been investigated, the influence of interfacial bonding geometry, which has been widely observed in ultrasonic welding, is rarely discussed. Jahn *et al.* [14] studied the influence of three different shapes of anvil on the weld formation and lap-shear performance. The study claimed that weld interface changes from a planar to a wavy morphology with increased weld strength as weld energy increases, but the overall performance is not sensitive to variation of anvil size and knurl pattern. Bakavos and Prangnell [15] found a three-stage wave-like interfacial displacement in USW of AA 6111 aluminum, which initiate from

micro-level scale of ~ 5 μm, to intermediate scale of ~ 20-50 μm, and ends up as a regular wave-like pattern of ~ 1 mm related to the sonotrode tip knurl pattern. Watanabe's group [16] observed different interfacial undulations using two sonotrode tips with a trapezoidal edge and a serrated edge, respectively, and implied that the interfacial geometry could affect the weld strength. Formations of interfacial undulations and mechanical interlocking are frequent phenomena in ultrasonic welds, especially for welding of thin and soft materials [10-15], but its impact on weld formation and performance is not well understood yet.

The influence of interfacial undulations on mechanical behavior has been studied in different aspects, especially in rock joints and adhesive bonds. Barton *et al.* [17-19] performed a series of studies in rock joints and developed an empirical model to predict the interfacial shear stress as a function of interfacial undulations and compressive pressure. Zeng and Sun [20] proposed a wavy-shaped adhesive single lap joint that can enhance the joint load carrying capacity by reducing the stress intensity at the edge of the bonding interface where interfacial separation dominates. Melograna and Grenestedt [21] conducted similar study using stronger adherends, and found a negative impact of a wavy-shape due to different failure locations. The conflicting results show that the effects of undulation are influenced by sample geometries and material properties.

A theoretical study of interfacial waviness was performed by several researchers. Bower's group [22-23] established a finite element model (FEM) to investigate the relation between critical stress intensity, K_{IC}, at the crack and the aspect ratio (amplitude/wavelength) of the sinusoidal interface in bonding of two elastic solids. The results indicate two positive linear relationships of the K_{IC} versus low and high aspect ratios. Li *et al.* [24] conducted a numerical study of hierarchical wavy interface morphology effects on fracture toughness in first and second order sinusoidal interface, and discovered that the enhancement of K_{IC} is positive linearly related to first-order

aspect ratio but positive polynomial to second-order aspect ratio. Hirsch and Kastner [25] investigated the influence of a microscale serrated interface on fracture performance in bi-material bonding, and revealed that the main mechanism leading to joint strengthening is the transition from interfacial to base material failure. Kim *et al.* [28] elucidated that interfacial undulations provoke the energy dissipation during fracture and therefore strengthen the joint. Systematic studies of non-flat interface effects on lap-shear performance of adhesively bonded joints were conducted by Jaiswal *et al.* [26] and Razavi *et al.* [27]. A design of experiments (DOE) was employed to evaluate the influence of sample geometries, material properties, and wave amplitude and length. The former group found more significant effects of overlap length and bonding type (brittle or ductile) than the pattern of the interface, while the latter group found an increase of joint strength by lower wave length and higher wave amplitude.

The interest in the effect of interfacial undulations on mechanical behavior in bi-material joints has been growing, as non-planar failures are ubiquitous in various bonds ranging from adhesives to bio-materials, to metals. However, ductile failure in an undulated interface of a bi-metal joint is not well understood. It is desirable to provide scientific guidance for improving bi-metal joining, especially for USW in this study, by investigating the effect of interfacial undulation.

Lap-shear strength is used as the criteria to describe the effect of interfacial undulation in adhesive joints [20, 21, 25-27], as well as in weld strength in USW. Zhou *et al.* [29-30] established an FEM to predict weld strength with interfacial and pull-out failure modes using a cohesive zone with a traction-separation-law model. Xi *et al*. [31] developed an FEM to predict interfacial weld performance for two-layered and multi-layered USW using a ductile damage material model. The models were calibrated based on measured weld attributes and validated by lap-shear tests.

The objective of this study is to investigate the influence of interfacial undulations on weld formation in USW, and assess the weld lap-shear performance subjected to different weld attributes and undulation features. Two anvils with different pyramid knurl teeth sizes were used to create different levels of interfacial undulations. Weld attributes were measured, including bond density, post-weld thickness, and interfacial undulations characterized by wave amplitude and length. The change of these features as weld energy was varied is discussed. Finite element models were developed to evaluate quantitatively the influence of interfacial undulation and bonding on lap-shear weld strength. The models were calibrated with measured weld attributes and validated by experimental results.

The remainder of this chapter is organized as follows: Section 4.2 describes the experimental procedure of USW and lap-shear test; Section 4.3 presents and compares the weld attributes and interfacial undulations over weld energy with the two anvils; Section 4.4 demonstrates the development of the FEM and discusses the influence of interfacial undulations; and Section 4.5 summarizes the study.

4.2. Experimental Setup

Commercial grade Al 1100-O and Cu 110 were ultrasonically welded using two pyramid knurl patterned anvils. This section describes the experimental procedure in creating and testing the ultrasonically welded samples.

4.2.1. Ultrasonic Welding Procedure

A single sheet of Al was welded on top of a Cu coupon, with a coupon dimension of 0.5 mm thick, 30 mm wide, and 45 mm long. The ultrasonic weld was made using a 20kHz, 5kW,

Branson^{TM} high power lateral-drive ultrasonic spot welder under an energy control mode, with the vibration direction parallel to the longer side of the coupons. The apparatus and weld configuration are presented in Fig. 4.1. The process parameters were selected after performing screening tests that established the weld quality boundaries. While investigating weld formation, the clamping pressure and horn vibration amplitude were fixed at 25 psi and 40 µm, respectively, and the weld energy was treated as the variable in this study. The welding parameters and their levels are depicted in Table 4.1. Four replicates were made at each setting, where three samples were lap-shear tested, and the remaining was cross-sectioned at A-A, as illustrated in Fig. 4.1 (b), for microscopic analysis.

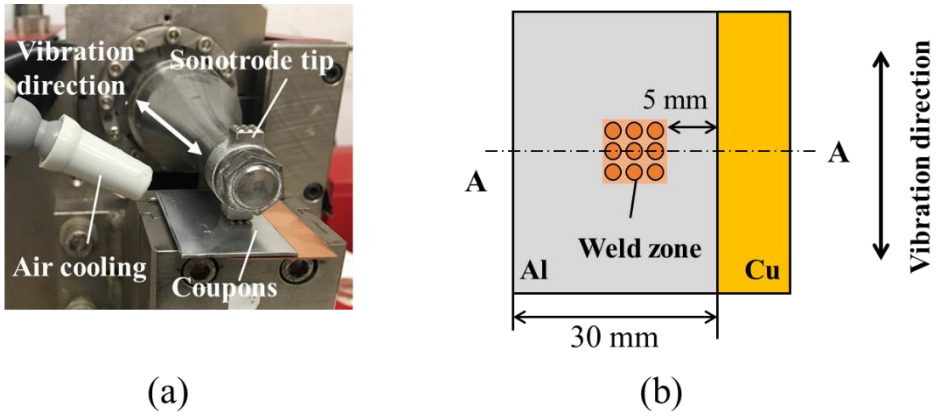

Figure 4.1 Experimental setup for USW (a) apparatus, and (b) top view of weld configuration schematic.

Table 4.1 Welding Factors and Levels

Factor	Level
Weld energy, E (J)`	100, 200, 300, 500, 700, 900, 1100, 1300
Anvil knurl	Fine, coarse

One sonotrode tip and two anvils with a “fine” and a “coarse” knurl pattern were used to produce samples with different undulation levels. Figure 4.2 shows the knurl patterns and their dimensions for the tip and the two anvils. The sonotrode tip has a 3-by-3 semispherical knurl pattern shown in Fig. 4.2 (a). Both the fine and coarse anvils have pyramid knurl patterns, as presented in Fig. 4.2 (b). The coarse anvil has four pyramids in a row on side A, and five on side B that also coincides with the vibration direction. The knurl patterns of the sonotrode tip and side A of the coarse anvil are perfectly aligned.

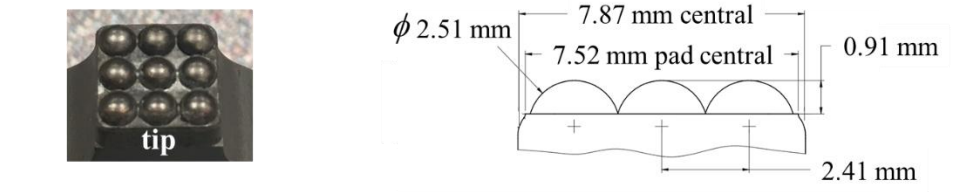

(a)

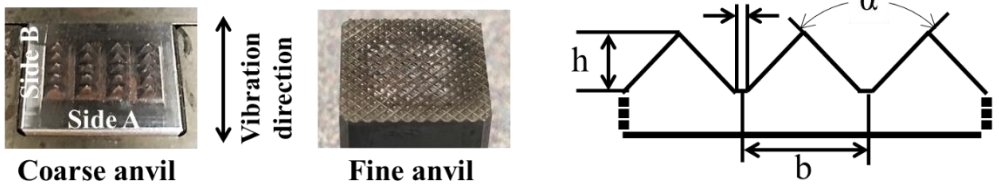

(unit: mm)

Anvil type	h	a	b	α
Fine	0.4	0.02	0.8	90°
Coarse (side A)	0.97	0.48	2.41	90°
Coarse (side B)	0.97	0.08	1.19	60°

(b)

Figure 4.2. Tool knurl patterns and dimensions: (a) sonotrode tip, and (b) two anvils.

4.2.2. Post-Weld Performance Testing/ Microscopy/ Weld Attribute Characterization

A lap-shear test was performed to evaluate the mechanical performance of weld samples, as shown in Fig. 4.3, using a MTS Instron testing machine with 5 kN load cell. The test shear

direction was perpendicular to the sonotrode vibration direction. Each setting was tested with three replicates at cross-head speed of 2 mm/min. The load-displacement curve, as well as the maximum load during the test, were recorded. The remaining sample was cross-sectioned, mounted in epoxy, polished, and etched using Keller's reagent for optical microscopy analysis. Weld attributes, including bond density, post-weld thickness, and interfacial undulation amplitude and length were characterized based on optical microscopy (OM) observations.

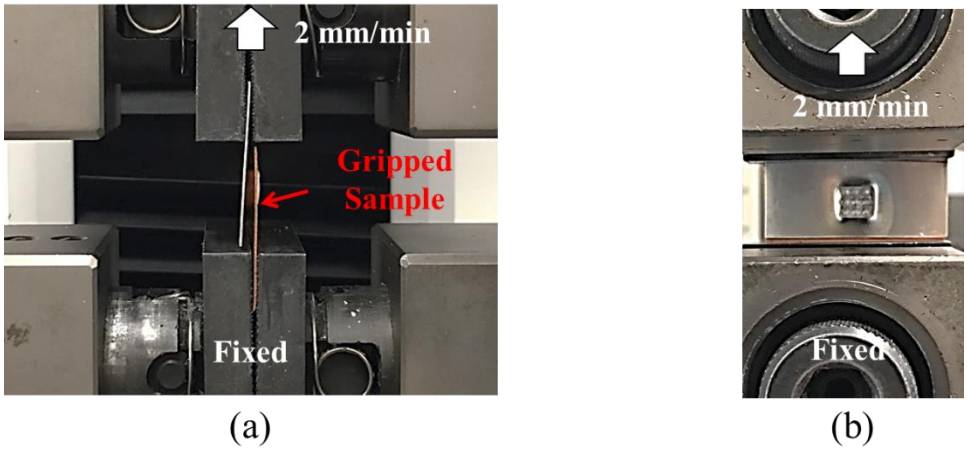

Figure 4.3. Apparatus of lap-shear test: (a) side view, and (b) front view.

4.3. Comparison of Lap-Shear Performance and Weld Attributes

The weld strength at different weld energies of the samples created using fine and coarse anvils was evaluated using lap-shear tests. The weld attributes that describe the bonding conditions are presumably correlated, and are defined, characterized, and compared in this section.

4.3.1. Lap-Shear Performance

Figure 4.4 shows the lap-shear performance of welds created with fine and coarse anvils subjected to different weld energies. The relationship between the maximum lap-shear load, which

represents the weld strength, and weld energy is presented in Fig. 4.4 (a). Three different failure modes can be observed in the studied cases: interfacial failures, partial pull-out failures, and circumferential failures. Examples of these failure modes are shown in Figs. 4.4 (b) to (d). As shown in Fig. 4.4 (a), from 100 J to 1300 J welding energy, the weld strength increases to a maximum value of about 750 N and then decreases for both fine and coarse anvils. At low weld energy (100 J to 300 J), the samples created by fine anvil have higher weld strength than those created by coarse anvil. The dominant failure mode within this range is interfacial failure. As energy increases to moderate level (500 J to 700 J), the failure mode changes to partial pull-out failure, a combination of interfacial separation and base material failure at edge of the weld zone. The maximum weld strength is reached with this failure mode at 500 J for the welds made by fine anvil and 700 J for the welds made by coarse anvil. Noticeably, there is not enough evidence showing significant difference in the maximum weld strength for welds made using different anvils in this study according to a T-test with P-value around 0.56. When weld energy in excess of 700 J is used, the failure mode is a circumferential failure. The weld strength decreases to around 620 N at 900 J and becomes flattened for the fine anvil case, while in the case of coarse anvil, weld strength gradually decreases to about 620 N at 1300 J.

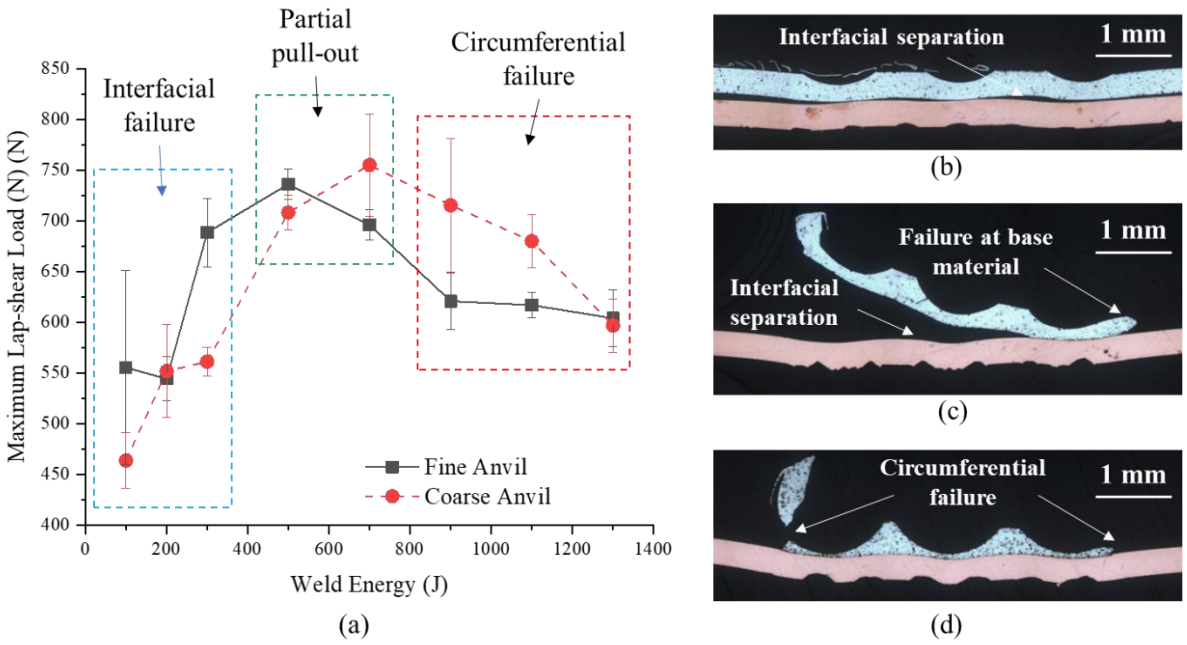

Figure 4.4 Lap-shear performance: (a) maximum lap-shear load and failed samples created using fine anvil at (b) 200 J, (c) 500 J, and (d) 900 J.

4.3.2. Definition of Weld Attributes

The weld attributes have a strong relation between the progress of the welding process and the corresponding weld strength, as observed on the fractured Al/Cu interface of the Cu coupon and in cross-sectional images at A-A. For example, Figure 4.5 shows images of a weld produced at 500 J using fine anvil. The sonotrode tip knurl created nine hemispherical indents on the top surface of the Al coupon, as presented in Fig. 4.5 (b), and left nine circular prints at the Al/Cu interface, as shown in Fig. 4.5 (a). The indentations on the Al coupon are like crests and valleys that represent the negative profile of the sonotrode knurl pattern, as shown in Fig. 4.5 (c). The cross-sectional images also show that the undulation and the knurl indentation are in phase, with bonds more likely to form in the valley regions at the interface.

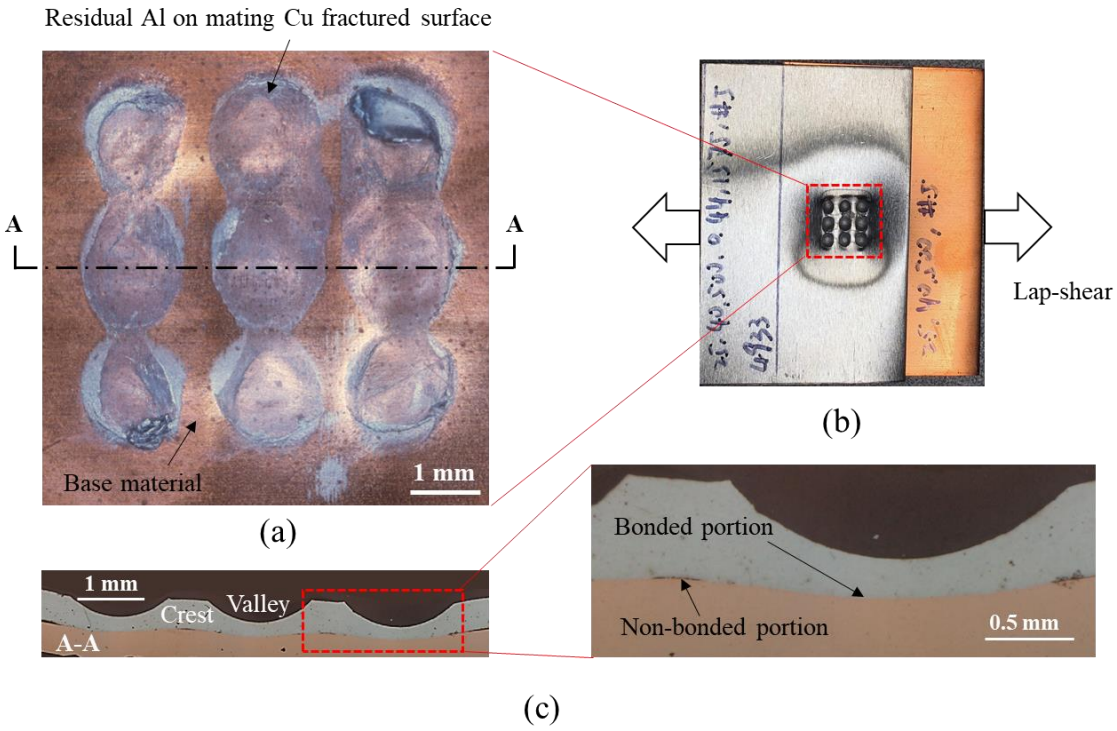

Figure 4.5. Images of sample produced at 500 J using fine anvil: (a) OM observation of fractured

Schematic diagrams representing the weld area at cross-section A-A quantitatively describe the key weld attributes and dimensions that affect the weld mechanical performance, as shown in Fig. 4.6. The effective dimensions in lap-shear tests include coupon size, weld size (W), weld deformation area size (L), and the thickness of coupons [32-33]. The indentation depth of the sonotrode tip knurl (e) was also recorded to calibrate the FEMs. Key weld attributes characterized in this study are bond density, post-weld thickness, and interfacial undulation amplitude and size, which are summarized as follows:

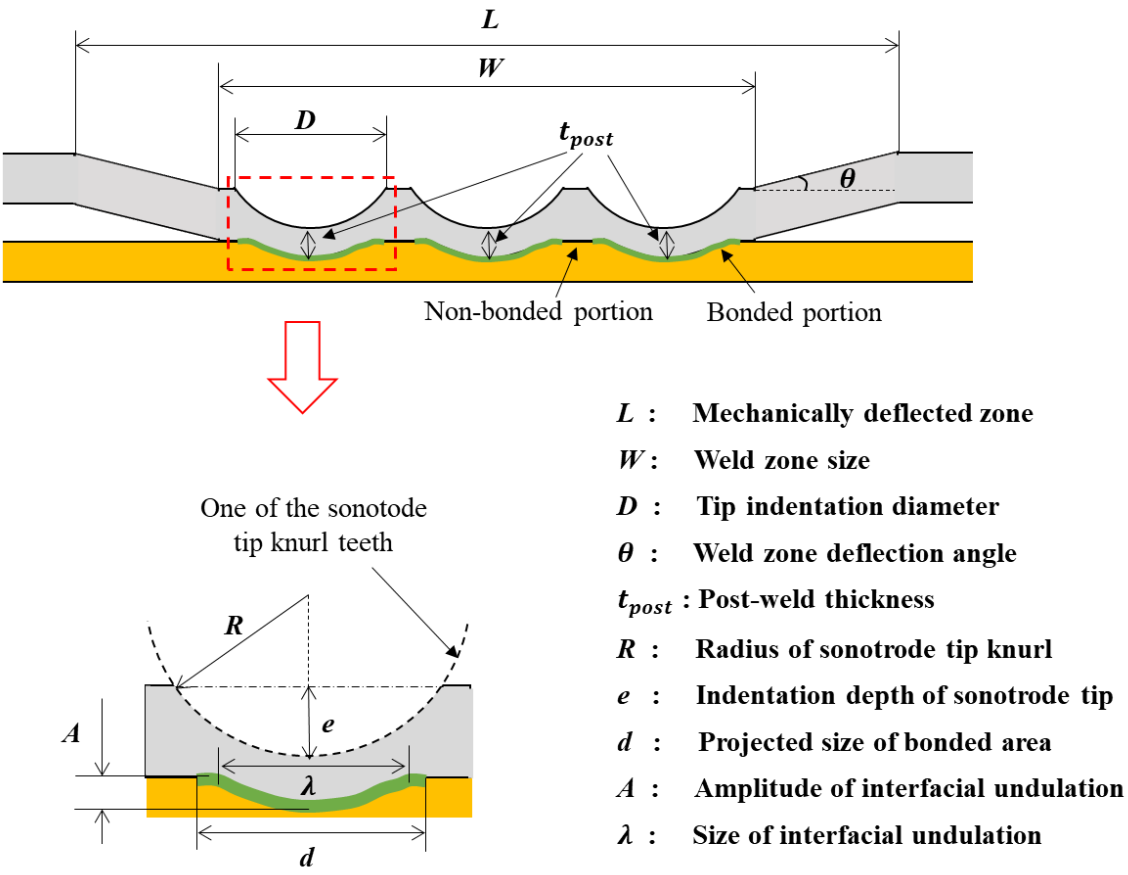

Figure 4.6. Schematic diagram of ultrasonic weld at cross-section A-A.

- *Bond density*: The bond density is defined as the fraction of projected bonding area to the entire footprint of the sonotrode tip area. The bonding area was estimated based on the amount of residual Al on the fractured mating Cu surface of tested samples. To determine the bonding area in samples with pull-out or circumferential failure, bonded and non-bonded regions were also distinguished in cross-sectional areas by microscopy. The area of the sonotrode tip footprint is estimated as the cross-sectional area of the sonotrode tip in this study, namely 7.5 mm × 7.5 mm.
- *Post-weld thickness*: The post-weld thickness is the average thickness of the indented region pressed by the sonotrode tip, which is the shortest distance from

the indented surface to the weld interface in the top layer coupon. The thickness reduction, which is a dimensionless parameter, is defined as the ratio of the post-weld thickness to the original material thickness.

- *Undulation amplitude*: The interfacial undulation amplitude is the average vertical distance from peak to the valley of the undulated interface, as illustrated in Fig. 4.4. The level of interfacial undulation is relative to the thickness of the coupon, and is defined as the ratio of the undulation amplitude to the post-weld thickness.
- *Undulation length*: The undulation length is the horizontal width of the undulated area at the interface. The aspect ratio $\kappa = A/\lambda$ is a frequently used geometric parameter describing the waviness of undulations [22-25] and was employed in this study.

4.3.3. Evolution of Weld Attributes

Multiple samples of different weld strength were cross-sectioned and characterized with optical microscopy to understand the influence of the interfacial undulations on weld attributes evolution. Observations of the cross-sectioned images made with different anvils and different weld energy are presented in Fig. 4.7. All samples studied exhibit a relatively smooth bonding interface without obvious material distortion or mixture. Slight and obvious undulations in phase with the tip knurl indentation can be found in samples created by both the fine and coarse anvils. In the case of using fine anvil, due to plastic deformation and indentation of the tools, as the weld energy increases the thickness of the Al coupon continuously reduces as materials are flattened and overflows along the knurl plane. This thinning is less evident for samples produced by the

coarse anvil because its more aggressive knurl pattern finds more space for the material to deform vertically instead of along the sonotrode knurl surface.

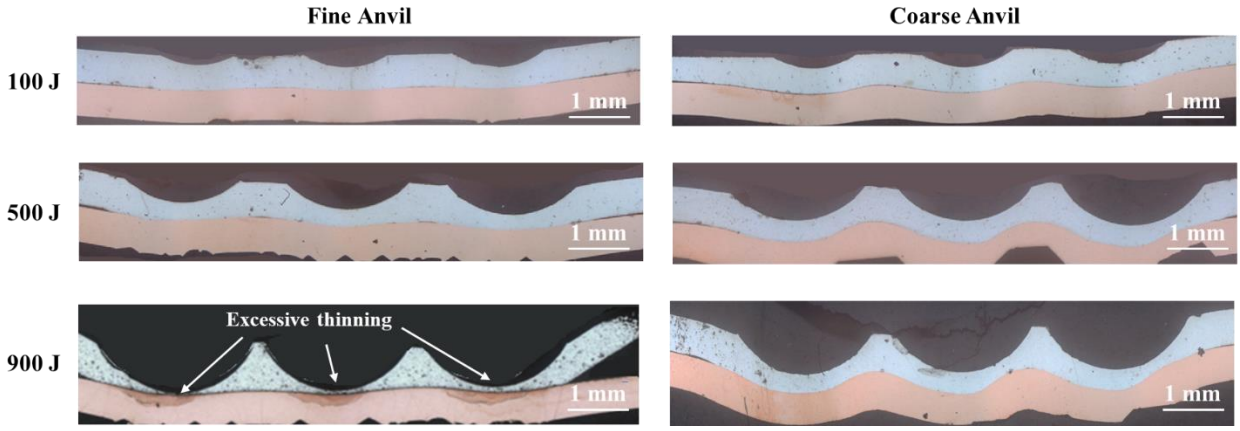

Figure 4.7. Cross-sectional micrographs of samples made by fine and coarse anvil at 100 J, 500 J and 900 J.

The fracture surface of samples made at low weld energy levels are shown in Fig. 4.8. The bright regions represent residual Al on the mating Cu surface, implying local bonding. In both cases, there are nine circular bonding spots that represent the indentation of the sonotrode knurl teeth. The size of these spots increases and the non-bonded regions among these spots shrink, and even disappear with increasing weld energy. In the case of a coarse anvil, a row of five additional smaller Al spots can be observed in between the larger circular bonding areas, which matches the five knurl teeth of the coarse anvil in the vibration direction as detailed in Fig. 4.2. Nevertheless, the three major waves in the cross-sectional images in Fig. 4.7 indicate that the smaller indentations caused by the anvil teeth do not change the undulation morphology at the interface. Moreover, the size of the major circular indentation from the tip knurl is smaller in the case of coarse anvil.

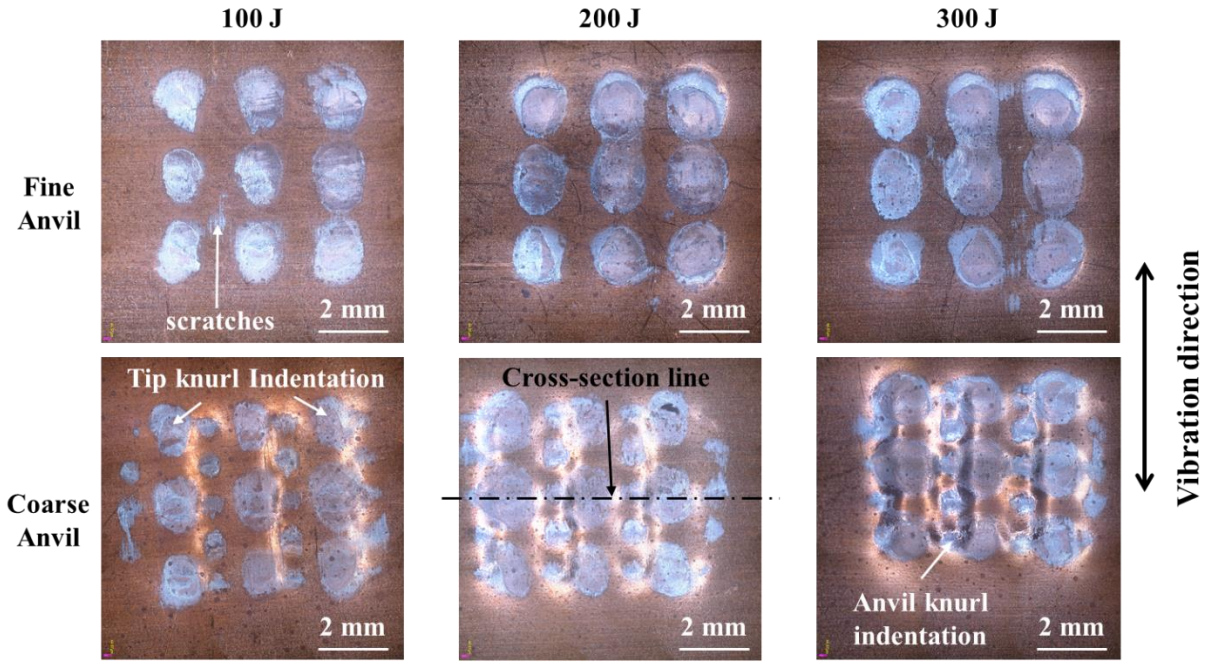

Figure 4.8. Fracture surface of samples made by different anvils at different weld energy.

Bond Density and Post-Weld Thickness

The bond density and post-weld thickness of select samples made by the two anvils were quantitatively measured as discussed in previous sections. The results for these two weld attributes is shown in Fig. 4.9. Figure 4.9 (a) shows there is no obvious difference in bond density for the two cases. In both cases, bond density stays constant as weld energy changes from 100 J to 200 J, then quickly grows as weld energy increases to 500 J. Thereafter, the bond density gradually increases to about 80 % at 1300 J. In comparison, the post-weld thickness, shown in Fig. 4.9 (b), differs significantly, especially at high weld energies. In the case of a fine anvil, the post-weld thickness continuously decreases at a relatively high rate. The thickness reduces to about 0.05 mm with a reduction rate of 95% when the weld energy is at 900 J. There is almost no thickness of Al at the joint location in samples created at 1300 J. In the case of a coarse anvil, quick post-weld thickness reduction is also observed, and there is no obvious difference in the two cases until weld

energy reaches 500 J. At 900 J, the post-weld thickness is measured as about 0.15 mm, which is much thicker than the sample made at same weld energy using the fine anvil. The thickness of the deformed weld stays constant as weld energy increases to 1300 J.

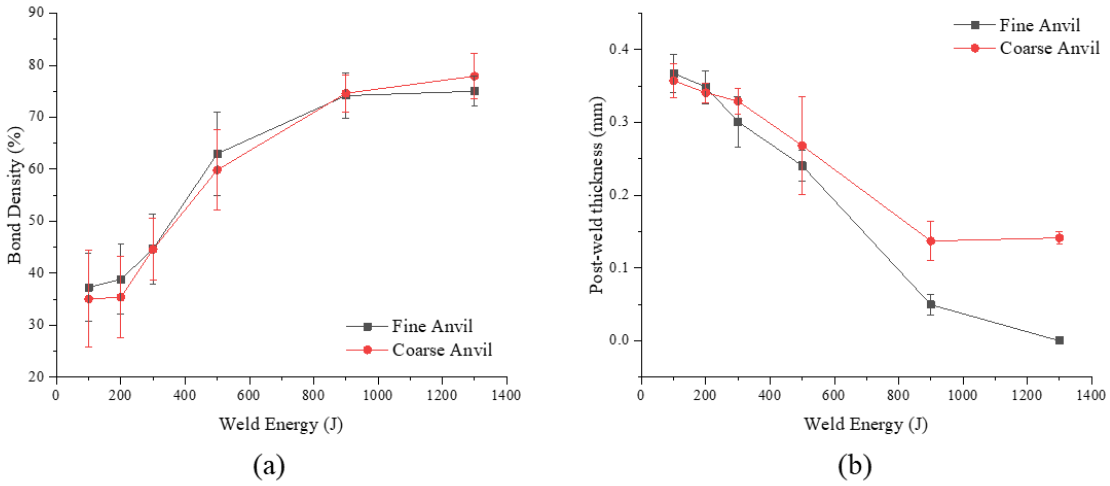

Figure 4.9. Comparison of (a) bond density and (b) post-weld thickness.

Interfacial Undulations

Interfacial undulations in phase with the sonotrode tip knurl can be found in all studied samples. The smooth undulating interface indicate that the formation of the waviness is caused by indentation of the sonotrode tip and anvil. Due to the symmetry of the tool knurl pattern, it is reasonable to use the morphology at the central cross-sectioned area to describe the undulation for the entire weld zone. The amplitude and size of the interfacial undulations were measured using micrographs of cross-section A-A, and the results are shown in Fig. 4.10. The coarse anvil introduces much more significant interfacial undulations than the fine anvil. Noticeably, the Al coupon is penetrated and the interface is almost flat in the sample made using fine anvil at 1300 J, thus the undulation information is not available for that condition.

The absolute value of the undulation amplitude and size are presented in Figs. 4.10 (a) and (b), respectively. These figures indicate that the coarse anvil introduces considerably higher undulation amplitude and large undulation size under all studied weld conditions. Figure 4.10 (a) shows that the undulation amplitude increases to a peak value at 500 J for the fine anvil, and at 900 J for coarse anvil, and then slightly decreases at higher weld energy. The reduction of the undulation amplitude for both cases implies flattening due to plastic deformation. The flattening might be caused by relative motion reduction between the coupons and is augmented between tool and coupons when weld energy is high [4]. Figure 4.10 (b) shows that the size of the interfacial undulation for samples made by the coarse anvil monotonically increases from around 1.8 mm to 2.1 mm as weld energy increases from 100 J to 300 J, and then stays at around 2.1 mm for higher weld energy. The size of the interfacial undulation is close to the tooth-to-tooth distance of the tip knurl, implying a maximum undulation size is reached and constrained by tool geometry. In contrast, the size of the undulation first increases, reaches the maximum value of 1.9 mm at 500 J, and then decreases when using a fine anvil.

The level of undulations (i.e. ratio of undulation amplitude to the average post-weld thickness, as defined in Section 4.3.2) subjected to weld energy is shown in Fig. 4.10 (c). For both cases, the level of undulation exceeds 100%, implying a universal deformation of the entire weld zone. Between the two cases, the coarse anvil introduces a higher level of undulation within the studied energy range. It is also worth noting that the level of undulation dramatically increases from about 30 % to 150 % as weld energy increases from 500 J to 900 J in the case of the fine anvil, although both post-weld thickness and undulation amplitude drop in these conditions. This phenomenon indicates that excessive thinning is predominant at this stage. The aspect ratio of the undulations is also studied and presented in Fig. 4.10 (d). The shape of the curve is similar to that

of the undulation amplitude for both cases. This similarity suggests that the dominant feature of the interfacial undulation is undulation amplitude.

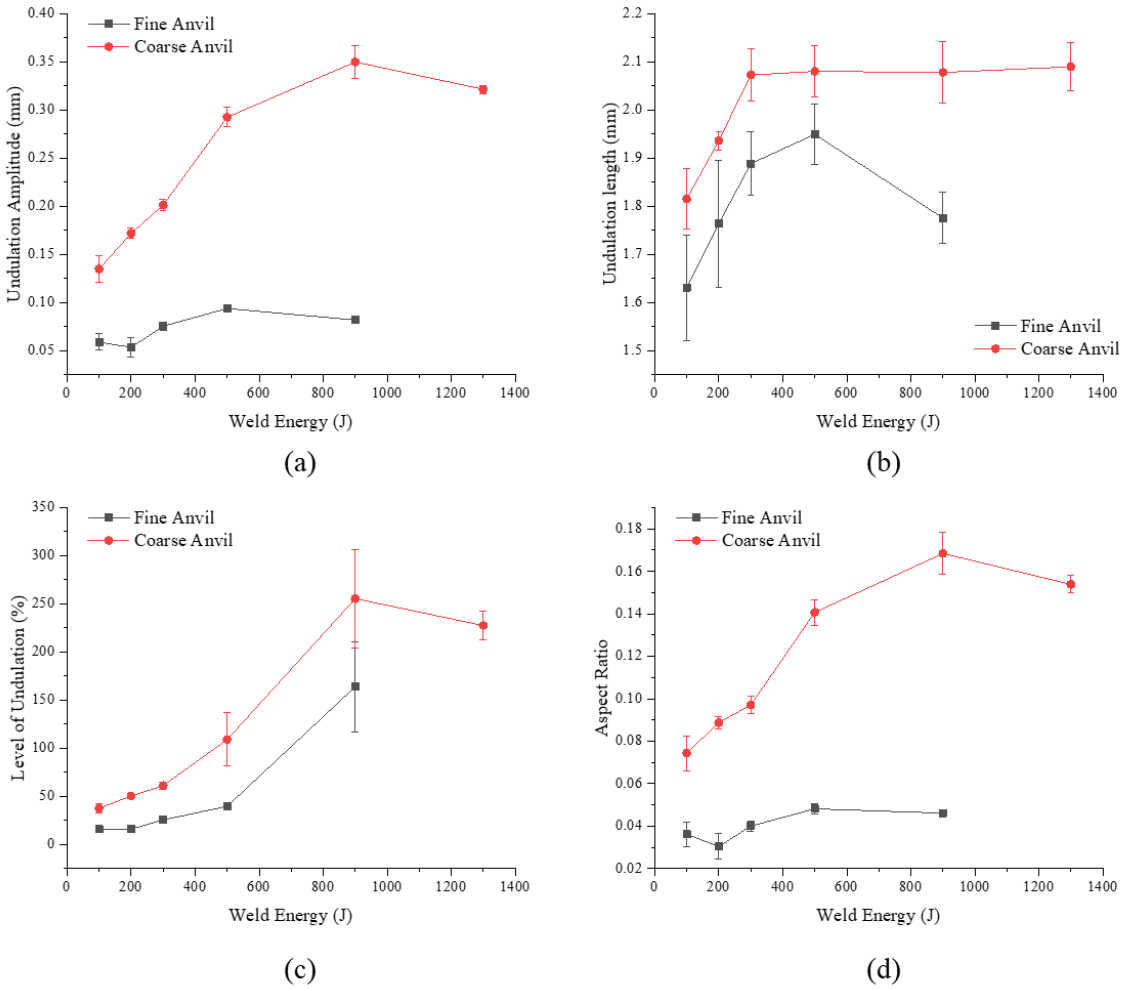

Figure 4.10. Change of interfacial undulations in samples made at different weld energy using the fine and coarse anvil: (a) undulation amplitude, (b) undulation size, (c) level of undulation, and (d) aspect ratio.

Hardness Profile

In addition to the weld attributes, hardness is also an important feature of ultrasonically welded samples. The hardness profile close to the bonding interface over the entire weld zone for different weld energies and anvils was collected and the results are shown in Fig. 4.11. The

hardness of original material as received is 29 HV, which is marked as as-received in the figures. A cross-sectional image illustrating the locations for hardness measurement is shown in Fig. 4.11 (a). The locations are classified into two groups, one at the valley and the other at the crest, as pointed out in Fig. 4.11 (a). The measurements were made at the center of each region, separated by a distance of around 1.2 mm. Figures 4.11 (b) and (c) present the evaluation of hardness at crests and valleys, respectively, for samples made at different weld energies by the two anvils. The hardness of both crest and valley locations increases with increasing weld energy and degrades with intense weld energy input. The initial hardening of the material results from plastic deformation, while the later softening is possibly caused by the elevated temperature and acoustic softening. Noticeably, material close to the interface is still harder than the as received material, indicating that material hardening is predominant during the process within the studied energy range. The average hardness in the valleys is relatively higher than that at the crest because more severe plastic deformation occurs in those areas under the press of the tool knurls. The comparison of hardness variations for samples made by the fine and coarse anvils indicates that the coarse anvil introduces higher hardness at the crest while lower hardness in the valley area during the process. The lower hardness variation in the samples made by the coarse anvil implies more uniform plastic deformation in the longitudinal direction of the workpiece.

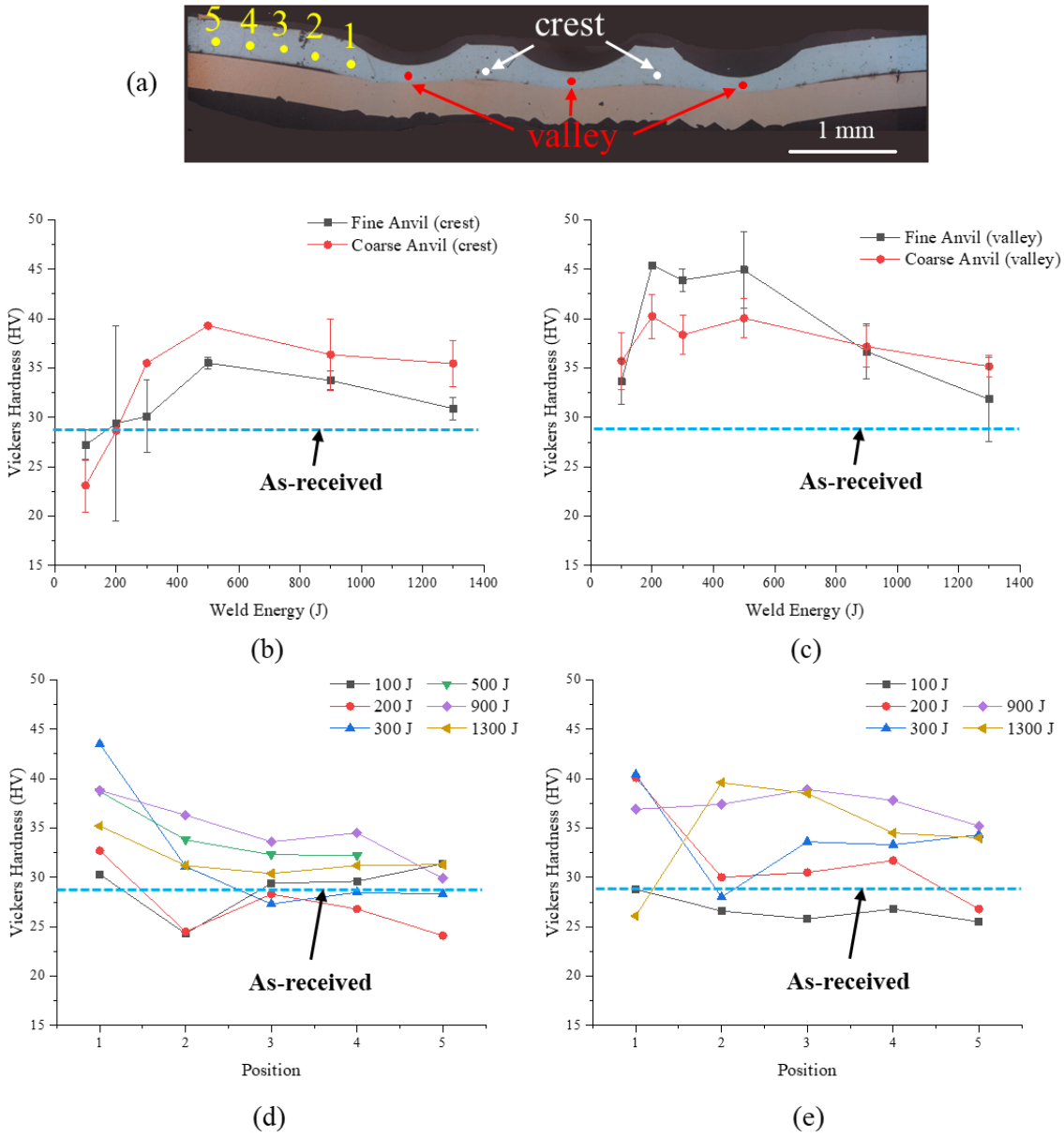

Figure 4.11. Hardness evaluation of welds for different weld energies and anvils: (a) cross-section image of weld made at 500 J using fine anvil, hardness profile of the weld interface at (b) crests and (c) valleys, and hardness profile out of weld zone for (d) file anvil and (e) coarse anvil.

The hardness distribution out of the weld zone was also investigated. Five points from the edge of the weld zone with 0.5 mm longitudinal interval were measured. The results are presented in Figs. 4.11 (d) and (e) for samples made by the fine and coarse anvil, respectively. In the case of

the fine anvil, the hardness gradually decreases to the level of the as-received material for all studied samples. The hardness variation over weld energy at the same location shows that the material experiences hardening, then softening during the process. In the case of the coarse anvil, similar hardness variation is observed, which suggests less influence of anvil geometry on the thermo-mechanically affected zone out of the weld region.

Hardness is an important index to illustrate the material property [10], and thus can empirically estimate the material yield strength in a positive linear relationship, as discussed by Cahoon *et al.* [34] and Tiryakioğlu *et al.* [35]. The relationship is expressed as:

$$\frac{\sigma_{y,measured}}{\sigma_{y,as-received}} = \frac{HV_{measured}}{HV_{as-received}} \tag{4.1}$$

Where σ_y represents the yield strength,$HV_{measured}$ is the Vickers hardness value of the measured area, and $HV_{as-received}$ is the original Vickers hardness for the as-received material. The plastic behavior of the material for different regions therefore can be indirectly estimated based on this relationship. Nevertheless, it is also worth noting that the hardness profile can only provide insight of the material properties and the accuracy is limited by the precise location of cross-section, and could also vary from sample to sample.

4.3.4. Summary of the experimental results

The lap-shear performance and the weld attributes of samples created by fine and coarse anvil were studied and compared. The lap-shear test results show that the maximum lap-shear strength can be achieved with a partial pull-out failure, and is not affected by the type of anvil used. The fine anvil creates a stronger weld with an interfacial failure when the weld energy is low, while the coarse anvil creates a stronger weld with a circumferential failure when weld energy is high.

Four weld attributes were quantitatively analyzed. The results indicate that the bond density increases with increasing weld energy, and is not affected by the anvil geometry, although the hardness indentations exhibit slightly different morphology. The post-weld thickness is negatively related to weld energy, and does not exhibit an obvious difference at low weld energy for both cases. However, the coarse anvil preserves the post-weld thickness at high weld energy. Slight interfacial undulations and considerable interfacial undulations can be found in samples made by the fine and the coarse anvil, respectively. Undulation amplitude was observed to increase first and then slightly decrease as weld energy increases. A reduction in the undulation amplitude implies flattening of the coupons. The undulation size is positively influenced by the weld energy and constrained by the knurl geometry in the case of coarse anvil, while at high weld energy it is more likely to be influenced by flattening effects in the fine anvil.

These experimental results indicate that different anvil knurl geometries introduce different characteristics of the weld attributes and thus different lap-shear performance. Previous studies claimed that the lap-shear performance of a joint is influenced by the geometry of the sample and the interface, and moreover, the strength of the base material and bonding. Exact local bonding strength is difficult to directly measure and can only be estimated. To estimate the bonding strength and develop a deeper understanding of the undulation effects, the lap-shear performance is evaluated numerically and discussed in the next section.

4.4. Finite Element Simulation of Lap-Shear Test

In this research three-dimensional finite element models were created using ABAQUS Dynamic Explicit to predict the lap-shear performance of the weld. The models were calibrated based on experimentally measured weld attributes. For select samples, the bonding strength at a

given weld energy was estimated to match the experimental results. An empirical relationship between bonding strength and weld energy was then developed. Validation of the model and the bonding strength estimation was accomplished by comparing the maximum lap-shear force, load-displacement curve, and the failure mode of experimental results for the remaining samples. To investigate further the influence of interfacial undulation in lap-shear test, models with a flat interface having the same bonding strength were built and compared with the models with an undulated interface. The flow chart showing the method is illustrated in Fig. 4.12.

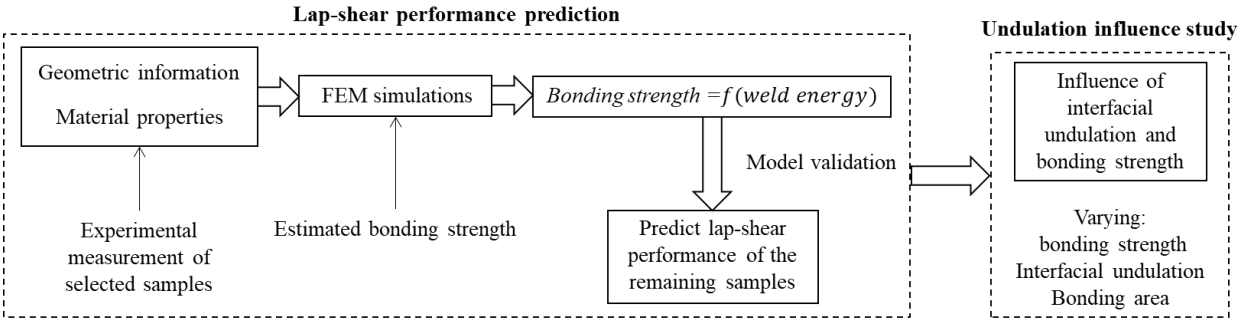

Figure 4.12. Flow chart of the FEM study.

4.4.1. Model Development

The finite element model consists of three parts, a top Al layer, a thin bonding layer, and a bottom Cu layer. The construction of the model is discussed as follows.

Geometry

The details of the model geometries are depicted in Fig. 4.12. The configuration of the model is shown in Fig. 4.12 (a). The dimensions of the top and the bottom layer were set as the same as the experimental coupons, with 0.5 mm thickness, 30 mm length in x-direction, 45 mm width in z-direction, and an overlap length of 20 mm. The deformation zone, representing the TMAZ, was set as 10 mm × 10 mm, and the weld zone was set as 7.5 mm × 7.5 mm. The TMAZ

was 5 mm away from the free edge of the top layer in the x-direction. A connector with a 10 mm length was introduced to mimic the grips of the Instron machine, as shown in Fig. 4.12 (a). Nine spherical indentations pressed by the sonotrode knurl were included in the model in the top layer while the indentation caused by the anvil in the bottom layer was neglected. The top Al layer and the bottom Cu layer were connected by a thin layer of bonding elements as illustrated in Figs. 4.12 (b) and (c). Three scenarios were modeled, one modeled the lap-shear test for the fine-anvil-made samples, the second one modeled the lap-shear test for the coarse-anvil-made samples, and the third one modeled the samples with flat interface. Figure 4.12 (b) depicts an example of the first two scenarios with undulated interface, and Fig. 4.12 (c) shows corresponding example of the last scenario with flat interface. The projected bonding area and the post weld thickness are kept the same for undulated and flat cases. The experimental observations indicate that the bonding area is not significantly influenced by the type of anvil, and therefore in all studied cases, the bonding layer was assumed based on the experimental observations to be nine partial spherical shells of 20 μm thickness each, as shown in Fig. 4.12 (b) and (c). At high weld energy, the nine bonding spots were assumed to be connected as shown in Fig. 4.12 (c).

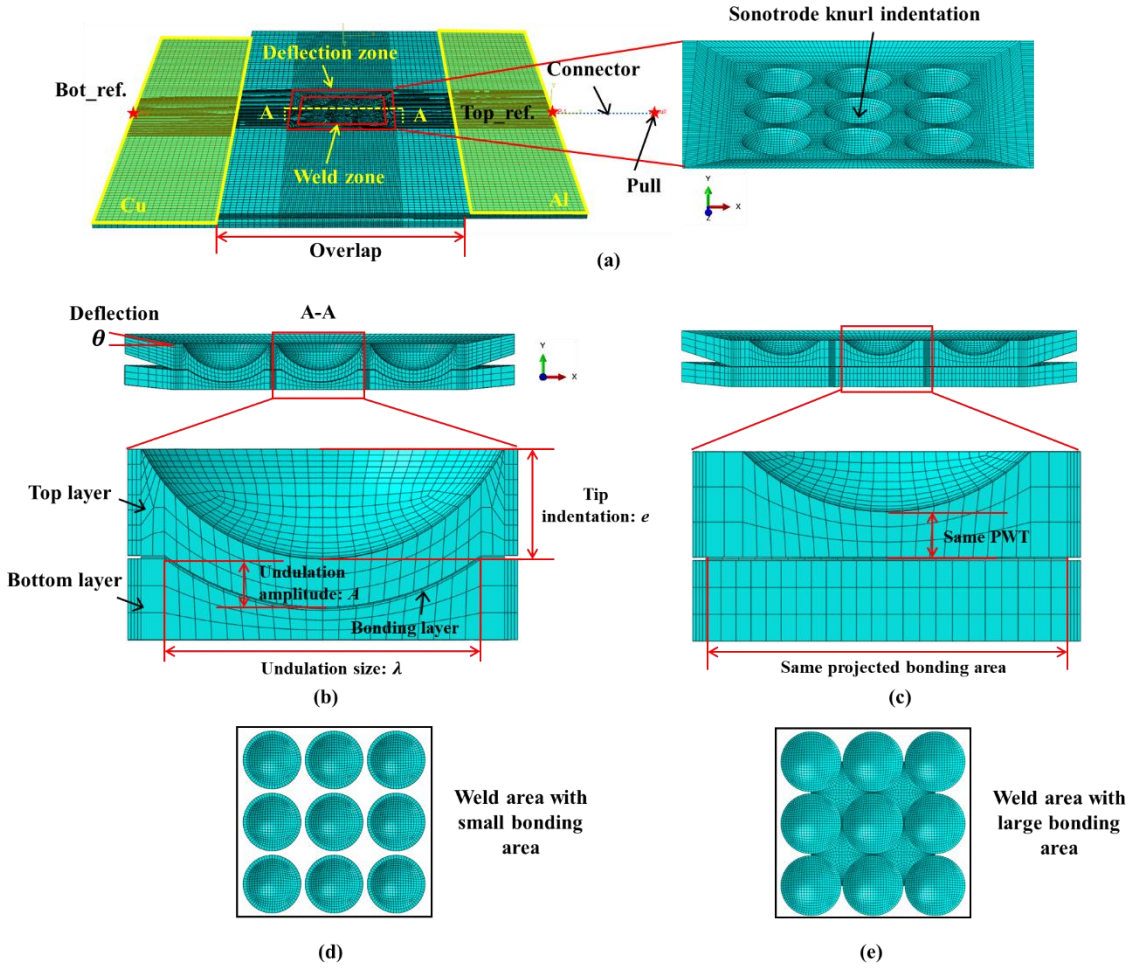

Figure 4.12. FEM for the lap-shear test: (a) model geometry, (b) cross-section view in weld zone for cases with undulated interface, (c) cross-section view in weld zone for cases with flat interface, (d) top view of bonding layer with small bonding area, and (d) top view of bonding layer with large bonding area.

For different welds, the geometry of the FEM was calibrated by varying five factors, including the tip indentation depth, e, the post-weld thickness, t_{post}, the undulation amplitude, A, the undulation size, λ, and the bonding size, d. These factors were experimentally measured as discussed in Section 4.3. The bonding size of the samples made by the coarse anvil was set the same as the samples made by the fine anvil at the same weld energy. To investigate the influence of interfacial undulation for different welds, flat interface phantom models with the same projected bonding size were also established.

Mesh

The model was meshed using explicit linear reduced integration hexagonal eight-node element of type C3D8R. The average element size was set as 0.5 mm in the non-weld area, and 0.1 mm in the weld zone. The element size gradually increases from 0.1 mm adjacent to the weld zone to 0.5 mm adjacent to the non-weld area in the deflection zone. The element size was selected to ensure the accuracy of the simulation while avoiding extreme computational time. Both the top and the bottom layers were each five elements thick, and the bonding layer had two layers of elements.

Boundary Conditions

The simulation only contains an initial step and a pull step. The bottom layer was fixed in both steps at the starred point marked as "Bot_ref." in Fig. 4.12 (a). The highlighted area on the Cu layer was coupled to this point and therefore constrained as a solid body and moves together with the reference point. Similarly, the highlighted area on the Al layer in Fig. 4.12 (a) was coupled to the point marked as "Top_ref.". This point was connected to the point marked as "pull" by an elastic translator connector with elasticity of 5000 N/mm, which was estimated from the initial slope of the load-displacement curves of the lap-shear tests. The introduction of the elastic translator connector simulated the effect of stiffness of the Instron machine. The "pull" point was constrained for all motions at the initial stage and then pulled a distance of 3 mm using "smooth step" in ABAQUS in a period of 0.3 s in the x-direction. To simulate the quasi-static test with reasonable computational time, a mass scaling factor of 500 was used [36].

The upper surface of the bonding layer was tied to the lower surface of the top layer, while the lower surface was tied to the upper surface of the bottom surface using a node-to-surface

relationship. The surfaces of the top and the bottom layers were set as master surfaces so that the nodes at the bonding layer surfaces moved together with the workpiece and failure occurred either at the bonding layer or at the base material.

Constitutive Material Model

The general material properties of the Al and Cu coupons are presented in Table 4.2. The plasticity of the materials were obtained from previous experimental results [31] and the stress-strain curves are shown in Fig. 4.13 (a). The yield strength of the Al coupon in the weld zone and deformation zone was modified based on the hardness measured using the relationship of Eqn. (1) in Section 4.3. For simplicity, the materials were assumed to have isotropic hardening and the Von Mises criterion was used for plastic yielding.

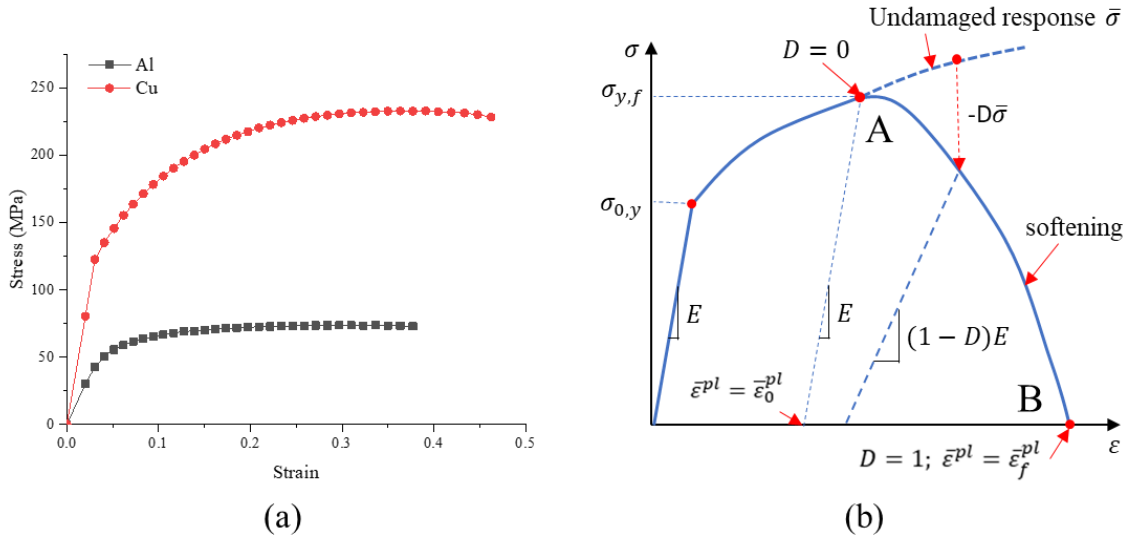

Figure 4.13. Stress-strain curves of (a) Al and Cu, and (b) schematic representative uniaxial progress damage model [31].

Table 4.2 General Material Properties of Al and Cu

Material	Density ρ (kg/mm^3)	Young's Modulus E (GPa)	Poisson's ratio ν	Yield strength σ_y (MPa)	Vickers Hardness (HV)
Al	2.7×10^3	70	0.35	30.7	28
Cu	8.9×10^3	115	0.33	82.2	91

Experimental observations have shown that the fracture mechanism in the Al-Cu ultrasonic welds are a combination of ductile and shear failure [24, 31]. Therefore, progressive failure models that include ductile and shear fracture provide a better description of the failures observed in lap-shear tests of ultrasonically welded Al-Cu samples, and thus were used as the damage criterion in this study for both base materials and the bonding layer.

The damage models include damage initiation and damage evolution. A schematic representative of a uniaxial progress damage model is shown in Fig. 4.13 (b). The material exhibits elastic-plastic behavior with strain hardening until reaching a maximum stress. Once the maximum stress is reached at point A, damage initiates due to micro void nucleation for ductile fracture, or shear band localization for shear fracture. Then the damage evolves from point A to point B with softening of yield stress and progressive degradation of the material stiffness. The mathematical representation of the damage model starts with an assumption of the decomposition of the total strain $\boldsymbol{\varepsilon}$ into an elastic part $\boldsymbol{\varepsilon^{el}}$ and a plastic part $\boldsymbol{\varepsilon^{pl}}$ [36]:

$$\boldsymbol{\varepsilon} = \boldsymbol{\varepsilon^{el}} + \boldsymbol{\varepsilon^{pl}} \tag{4.2}$$

The effective stress tensor of the material $\bar{\boldsymbol{\sigma}}$, postulated as the undamaged response, is a function of strain and 4th order elastic tensor $\boldsymbol{C}$:

$$\bar{\boldsymbol{\sigma}} = \boldsymbol{C}(\boldsymbol{\varepsilon} - \boldsymbol{\varepsilon^{pl}}) \tag{4.3}$$

The actual stress $\boldsymbol{\sigma}$ at each stage of the damage evolution is determined by the effective stress $\overline{\boldsymbol{\sigma}}$ and a non-decreasing scalar damage variable *D*:

$$\boldsymbol{\sigma} = (1 - D)\overline{\boldsymbol{\sigma}} \tag{4.4}$$

At point A, the damage variable *D* equals zero and the equivalent plastic strain $\overline{\boldsymbol{\varepsilon}}^{\boldsymbol{pl}}$ is equal to $\overline{\boldsymbol{\varepsilon}}_{\boldsymbol{0}}^{\boldsymbol{pl}}$, which is the value at the onset of damage. For ductile damage, $\overline{\varepsilon}_{0,D}^{pl}$ is a function of stress triaxiality $\eta = -p/q$ and strain rate with p being the hydrostatic pressure and q being the equivalent Von Mises stress. For the shear damage, $\overline{\varepsilon}_{0,S}^{pl}$ is a function of shear stress ratio $\beta_s = (q + k_s p)/\tau_{max}$, where k_s is a material parameter and τ_{max} is the maximum shear stress. The criterion is met when the state variable, ω, which monotonically increases with plastic deformation, equals 1:

$$\omega = \int \frac{d\overline{\varepsilon}^{pl}}{\overline{\varepsilon}_0^{pl}} = 1 \tag{4.5}$$

where $\overline{\varepsilon}^{pl}$ is the plastic strain, and $\overline{\varepsilon}_0^{pl}$ is the plastic strain onset of fracture initiation, which depends on η and plastic strain rate $\dot{\varepsilon}^{pl}$ for ductile failure and β_s and $\dot{\varepsilon}^{pl}$ for shear failure. In this study, a quasi-static state based on the experiments was simulated and therefore the influence of strain rate is neglected. For both Al and Cu in this study, the equivalent fracture strain at damage initiation subjected to triaxiality and shear stress ratio were obtained from a previous study by Xi *et al.* [31]. The value of k_s was set as 0.3 per [31].

At point B, complete failure occurs when the value of *D* decreases to zero and the value of $\overline{\boldsymbol{\varepsilon}}^{\boldsymbol{pl}}$ changes to $\overline{\boldsymbol{\varepsilon}}_{\boldsymbol{f}}^{\boldsymbol{pl}}$ which is determined by the fracture energy G_f, where

$$G_f = \int_{\overline{\varepsilon}_0^{pl}}^{\overline{\varepsilon}_f^{pl}} L\sigma_y d\,\overline{\varepsilon}^{pl} = \int_0^{\overline{u}_f^{pl}} \sigma_y d\,u^{pl} \tag{4.6}$$

In the function, L is computed automatically by ABAQUS based on element geometry, and $\overline{u}_f^{pl}$ is the equivalent plastic displacement. The damage evolution from point A to point B can be specified either by G_f or $\overline{u}_f^{pl}$. For simplification of the model, a linear displacement-based damage evolution law was selected and the complete failure displacement was set as 0.1 based on a previous study [31]. The element with complete failure will be removed in ABAQUS.

The fracture morphologies of interfacially failed samples reveals that the interface experiences ductile-brittle hybrid fracture in Al/Cu ultrasonically welded samples, and that failure on the Al side is predominant. To simplify the model, the properties of the bonding layer was assumed similar to the base Al material with partial Al strength. The yield strength of the bonding layer was defined as:

$$\sigma_b = \alpha\sigma_{Al} \tag{4.7}$$

where α is the bonding strength factor influenced by weld energy and the type of anvil. The general material properties and the damage model of the bonding layer were set the same as those of base Al.

4.4.2. Calibration of Bonding Strength

An empirical relation between bonding strength factor α and weld energy was built by matching the maximum shear load and load-displacement curve of selected samples with varying value of α. A validated relation can be used to predict the weld performance of all welds within the studied range.

Figures 4.14a-4.14d illustrate examples matching the simulation with calibrated bonding strength to experimental results for the fine anvil case. The welds with interfacial failures present a relatively good match between the simulation and experimental results, as shown in Figs. 4.14 (a) and (b). The simulations of the welds with a base material failure exhibit a slight over

estimation. Overall, the simulations show a reasonable match with the experimental results, and the bonding strength factor gradually increases with increasing weld energy.

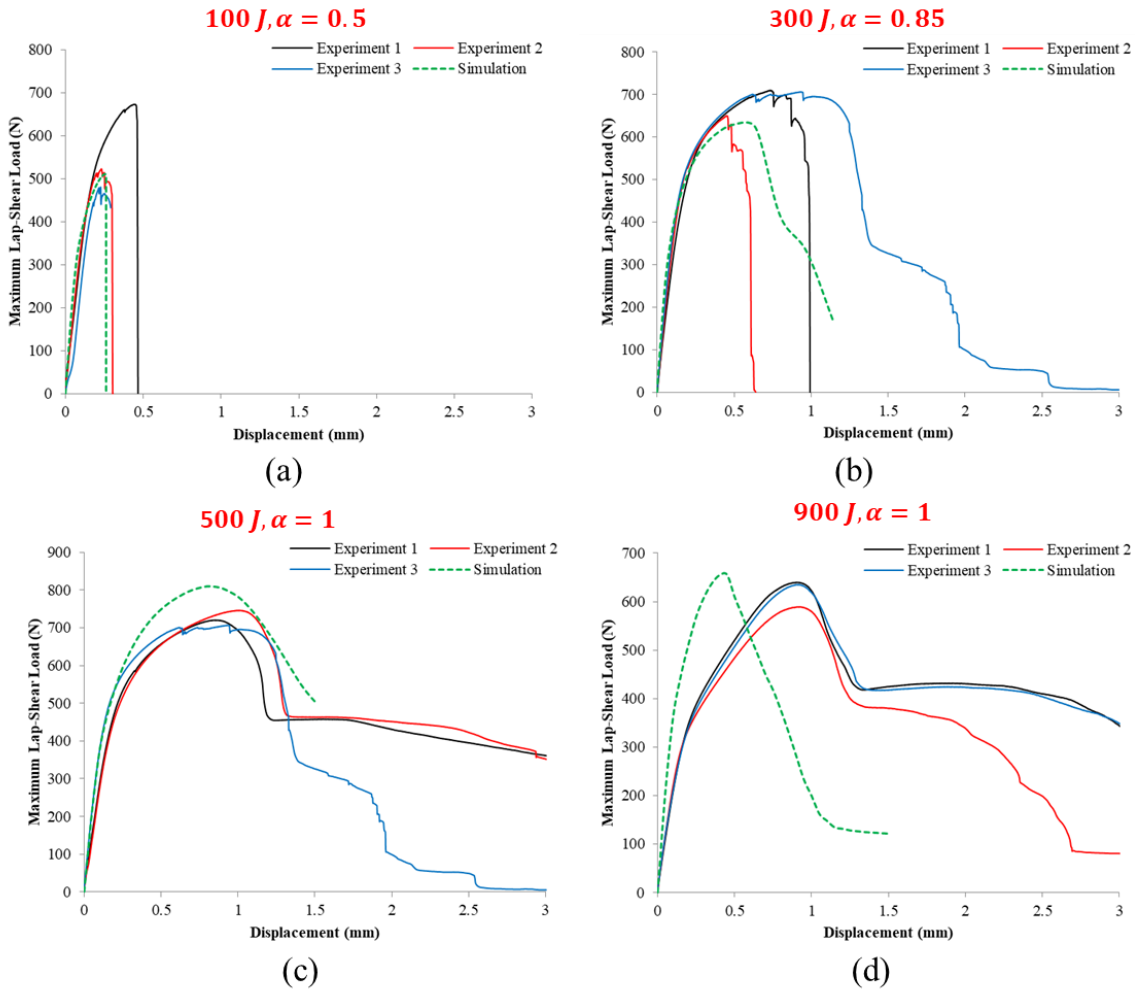

Figure 4.14. Comparison of load-displacement curve for experimental and simulation results for fine anvil at (a) 100 J, (b) 300 J, (c) 500 J, and (d) 900 J.

The comparison between simulation and experimental results for selected samples produced using a coarse anvil is presented in Figs. 4.15a-4.15d. All simulations show good match with the experimental results. The simulation results indicate a smaller bonding strength factor in the case of the coarse anvil than that of the fine anvil.

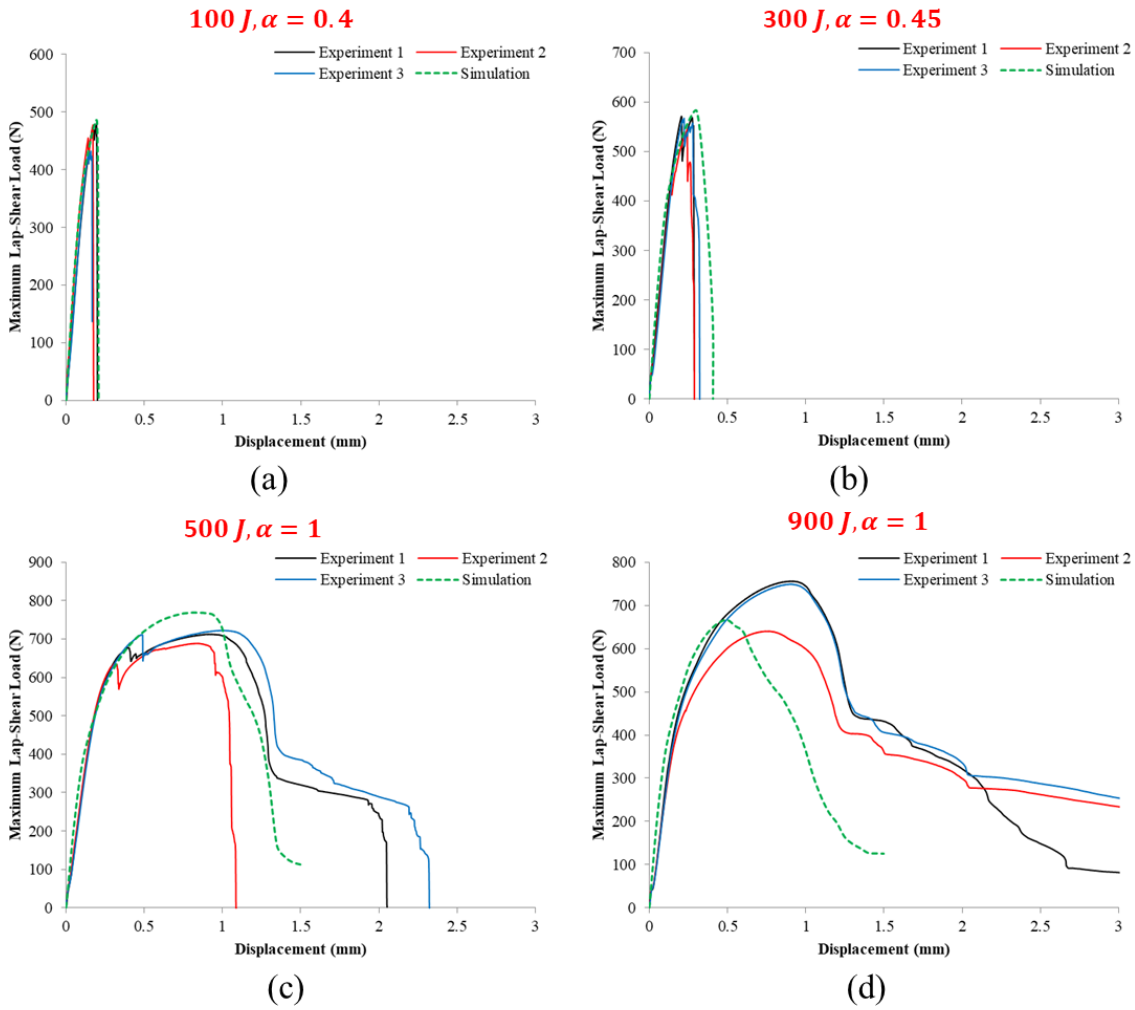

Figure 4.15. Comparison of load-displacement curve for experimental and simulation results for coarse anvil at (a) 100 J, (b) 300 J, (c) 500 J, and (d) 900 J.

Regression functions predicting the bonding strength factor for the two studied cases were summarized as

$$\alpha_{fine} = \begin{cases} -7 \times 10^{-7} W_E + 0.0017 W_E + 0.3227 & (W_E < 500\,J) \\ 1 & (W_E \geq 500\,J) \end{cases} \quad (4.8)$$

$$\alpha_{coarse} = \begin{cases} 5 \times 10^{-6} W_E - 0.0018 W_E + 0.0.5482 & (W_E < 500\,J) \\ 1 & (W_E \geq 500\,J) \end{cases} \quad (4.9)$$

where α_{fine} and α_{coarse} are the bonding strength factor for the fine and the coarse anvil case, respectively, and W_E represents the weld energy used. The R-squared value is 0.985 for Eqn. (4.8) and 0.982 for Eqn. (4.9). Remarkably, the bonding strength cannot be directly evaluated as the failure mode transfers to pull-out, and the bonding strength for samples failure in the base material is assumed to be the same as Al. Predictions of the bonding strength factor for welds made by the two anvils are presented in Fig. 4.16. The predictions show that the fine anvil initiates higher bonding strength than the coarse anvil does.

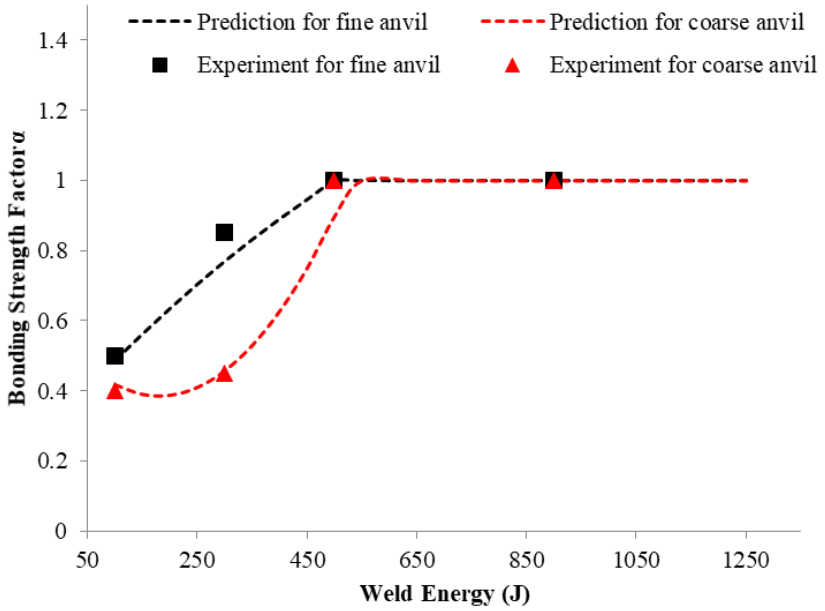

Figure 4.16. Predicted versus experimental dependencies of bonding strength factor.

4.4.3. Model Validation

Validation is necessary to evaluate the feasibility of the developed FEM and the predicted bonding factor. The validation was performed by comparing the simulation and experimental results with the predicted bonding strength. Samples made with 200 J and 700 J were used to validate the simulation. The geometric information was obtained experimentally, and the bonding

strength factor were calculated as 0.635 for 200 J and 1.00 for 700 J with the fine anvil, and 0.400 for 200 J and 1.00 for 700 J with the coarse anvil. The comparison of maximum lap-shear load and load-displacement curve between the simulation and experimental results are shown in Fig. 4.17. The accuracy of the simulation was calculated by

$$accuracy = \frac{\left|F_{simulation} - F_{exp.ave.}\right|}{F_{exp.ave.}} \times 100\% \quad (10)$$

where the $F_{simulation.}$ and $F_{exp.ave.}$ represent the maximum lap-shear load of the simulation and experiments, respectively. The accuracy from the simulation of the fine anvil was 1.4% at 200 J and 6.7% at 700 J, while the accuracy from the simulation of the coarse anvil was 8.1% at 200 J and 5.4% at 700 J. The comparison of load-displacement curves between the simulation and experimental results are plotted in Figs. 4.17 (b) to (c) and (e) to (f). All simulation curves show good agreement with the experimental results. The validation demonstrates that the constructed models are appropriate for simulating the lap-shear performance of the ultrasonically welded samples and the prediction of the bonding strength is reasonable.

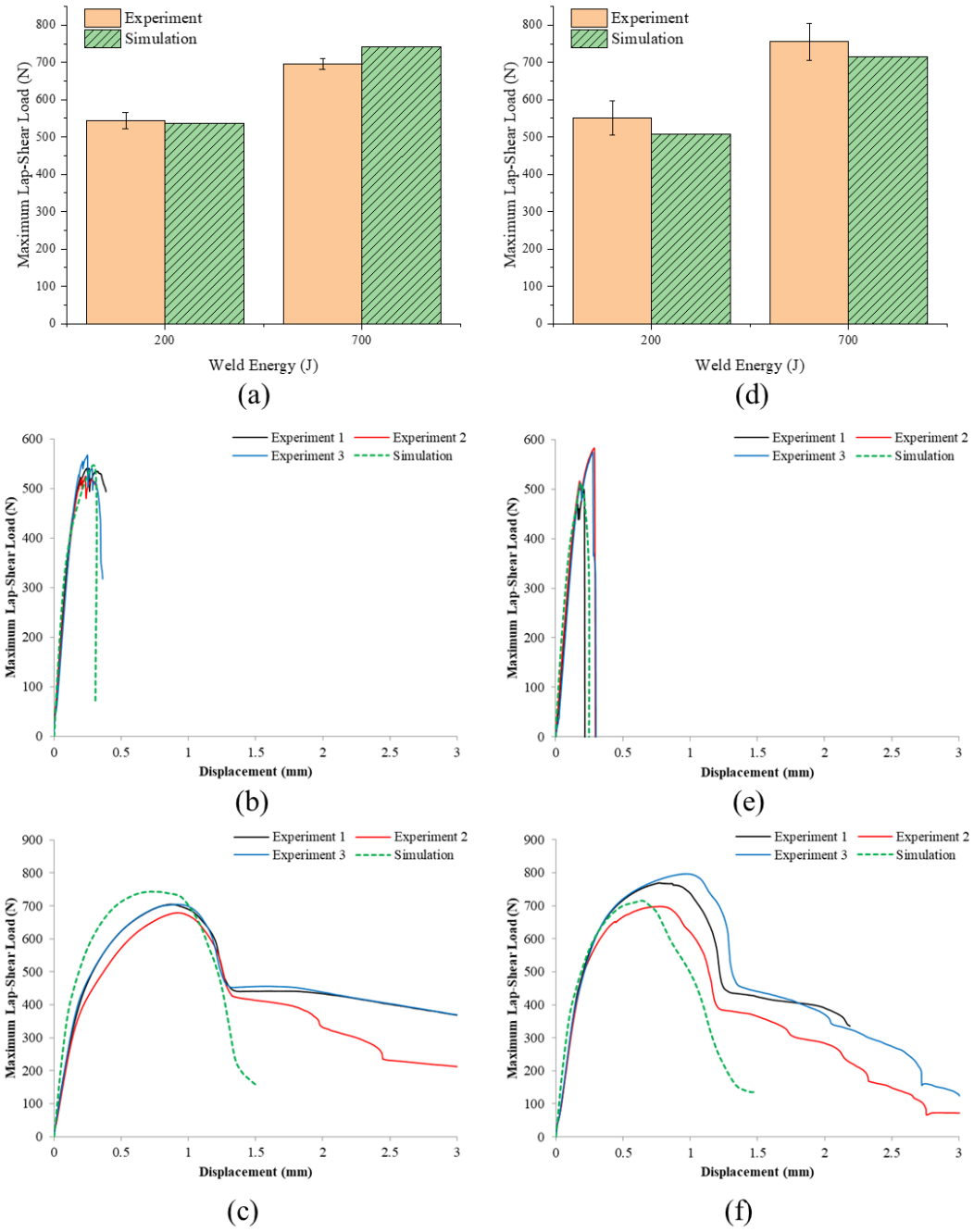

Figure 4.17. Comparison of experimental and simulation results in peak lap-shear load for (a) fine anvil and (d) coarse anvil, and load-displacement curve for (b) 200 J with fine anvil, (c) 700 J with fine anvil, (e) 200 J with coarse anvil, and (f) 700 J with coarse anvil.

4.4.4. Influence of Interfacial Undulation and Bonding Strength

To quantify the contribution of interfacial undulations on the lap-shear strength of a weld, corresponding models with flat interfacial bonding were constructed at varying weld energy. The lap-shear performance was compared with the models built based on samples made by the coarse anvil. In the flat bonding models, the projected bonding size is equal to that of the undulated bonding models, while the post-weld thickness and the material properties were set the same as the models with undulated interface constructed under the same weld energy.

Figure 4.18 presents the comparison of the peak lap-shear load in models with flat and undulated interface. The results indicate that interfacial undulation first improves the maximum lap-shear load in models for 100 J and 200 J by about 4% and 10 % respectively, where interfacial failure is predominant. As the major failure transfers its mode from interfacial to the base material, the interfacial undulation starts to negatively affect the lap-shear performance. The reduction varies at about 5%, 2 %, 15%, and 14% in models made for 500 J, 700 J, 900 J, and 1100 J. respectively.

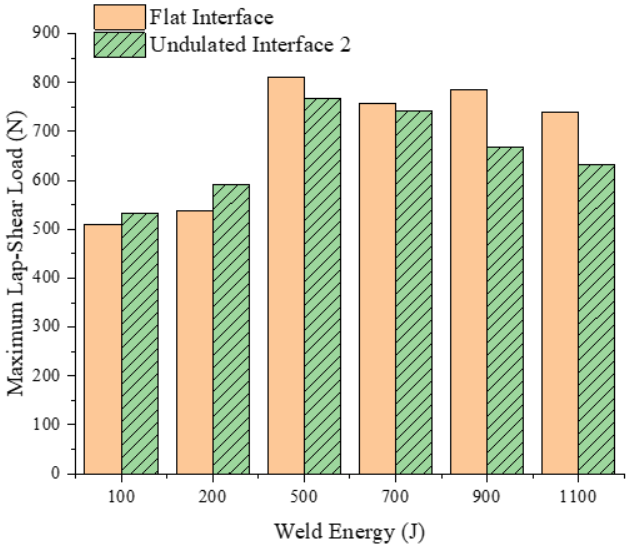

Figure 4.18. Comparison of peak lap-shear load between flat and undulated interface.

The load-displacement curves of models with flat and undulated interface for the interfacial and circumferential failure conditions are compared in Fig. 4.19. According to Fig. 4.19 (a), there is no significant difference in lap-shear behavior with an interfacial failure between flat and undulated interface in the studied case. However, higher toughness is evident in the behavior of flat-interface model compared with failure in the base material, as shown in Fig. 4.19 (b).

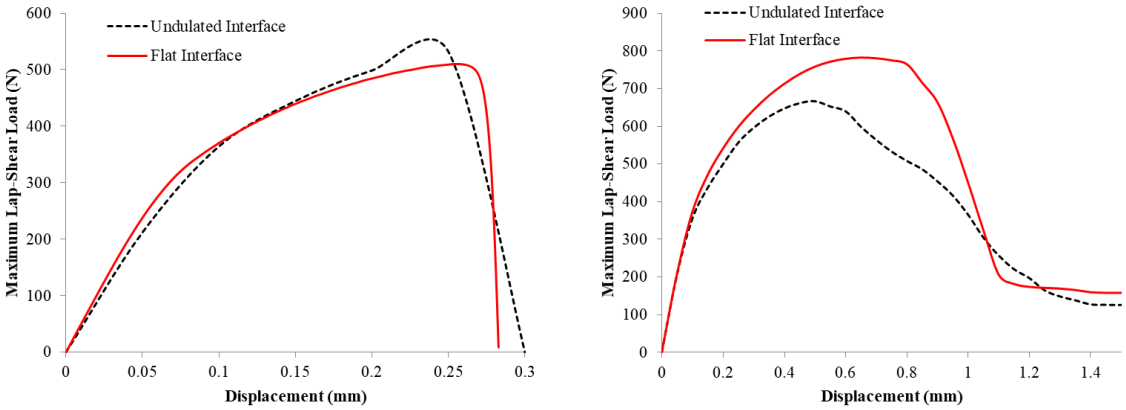

Figure 4.19. Load-displacement curve for (a) 100 J with interfacial failure, (b) 900 J with circumferential failure.

The evolution of the equivalent Von Mises stress distribution at the bonding layer for interfacial failure cases are presented in Fig. 4.20. The stage illustrated includes the displacement of the pull-point at 0.05 mm, 0.15 mm, and 0.2 mm, where the maximum lap-shear load is reached in the flat interface. Both undulated and flat bonding cases show that stress concentration initiates from the edge of the weld and develops toward the inner side of the weld. In the flat interface model, the stress is more uniformly distributed and at a higher magnitude. A schematic of the status of the elements in the bonding layer from start to failure is presented in Fig. 4.20 (c). The elements deform under the shear effect from the top and the bottom layer, and the elements experiencing the highest local stress are removed when the failure criterion is satisfied. The simulation shows that the failure can occur either in one layer of the elements, or in both layers.

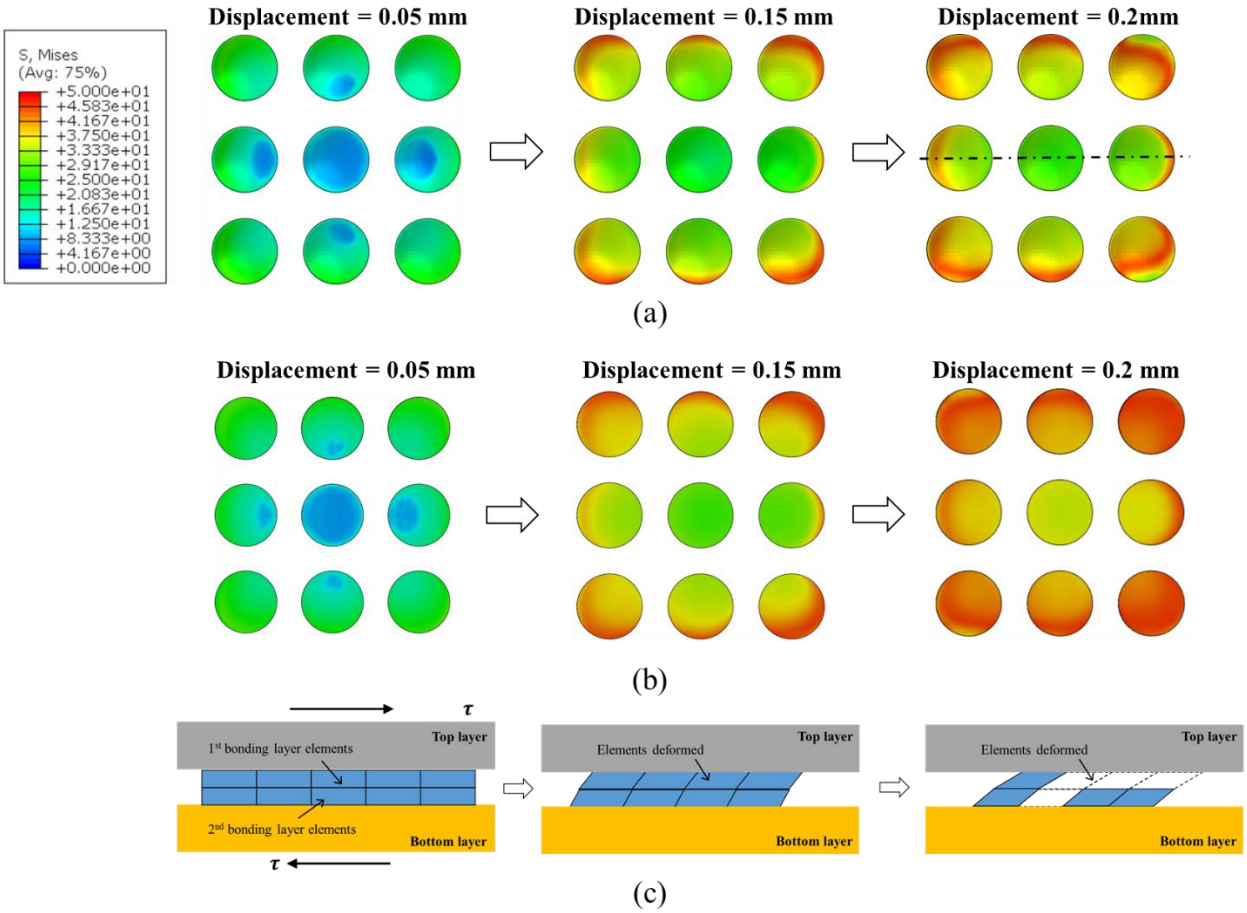

Figure 4.20. Mechanical behavior evolution at the bonding layer for the cases with interfacial separation: (a) stress distribution for undulated interface, (b) stress distribution for flat interface, and (c) schematic of element deformation and removal.

To further verify the stress difference between a flat and undulated interface, the equivalent Von Mises stress distribution is tracked along the dashed line in Fig. 4.20 (a) at the bonding layer and the results are presented in Fig. 4.21. The three line segments indicate the stress distribution in the bonding spots from left to right. In both cases, higher stresses are present at the two ends of the bonding layer, and relatively constant stress exists in the inner areas. The flat bonding layer experiences higher stresses for the entire center area, which ranges from about 35 MPa at the inner side to about 45 MPa at the ends. The bonding layer also has high stress concentration at about 45 MPa at the ends, but has lower stress at the inner area with about 30 MPa. A possible reason could

be that the undulated interface increases the phase angle of a mixed mode failure, and thus increases the toughness of the local area.

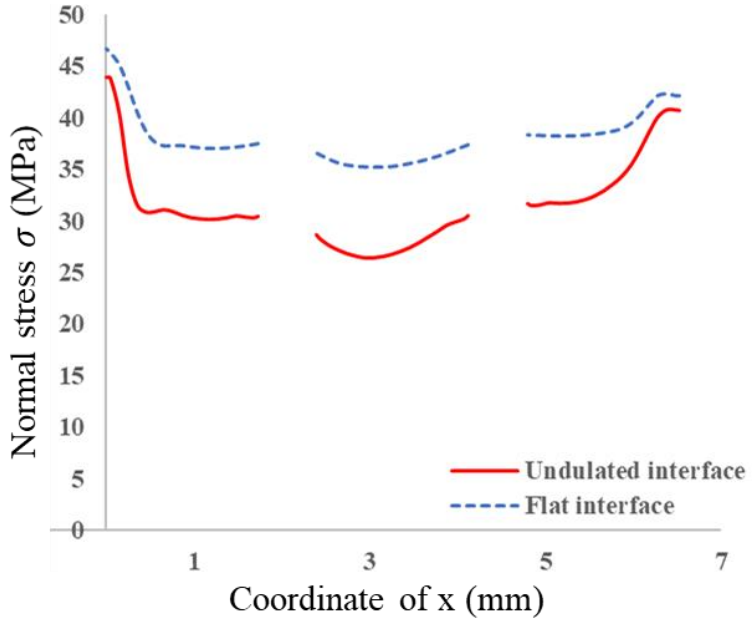

Figure 4.21. Equivalent Von Mises stress distribution at the center of the bonding layer for flat and undulated interface with 0.2 mm pull-point displacement.

In contrast to the positive effect of an undulated interface in the case of interfacial separation, interfacial undulation yields a reduction in the lap-shear load carrying capacity when a failure occurs in the base material. Figure 4.22 shows the stress distribution in the top layer with 0.65 mm pull-point displacement. The results indicate a higher stress concentration at the edge of the weld area in the case with undulated interface. There is little failure in the bonding layer when tearing occurs in the base material. Thus, the mechanical performance is determined by the stress distribution in the softer top layer. Therefore, higher stress at the weld edge implies lower load carrying capacity.

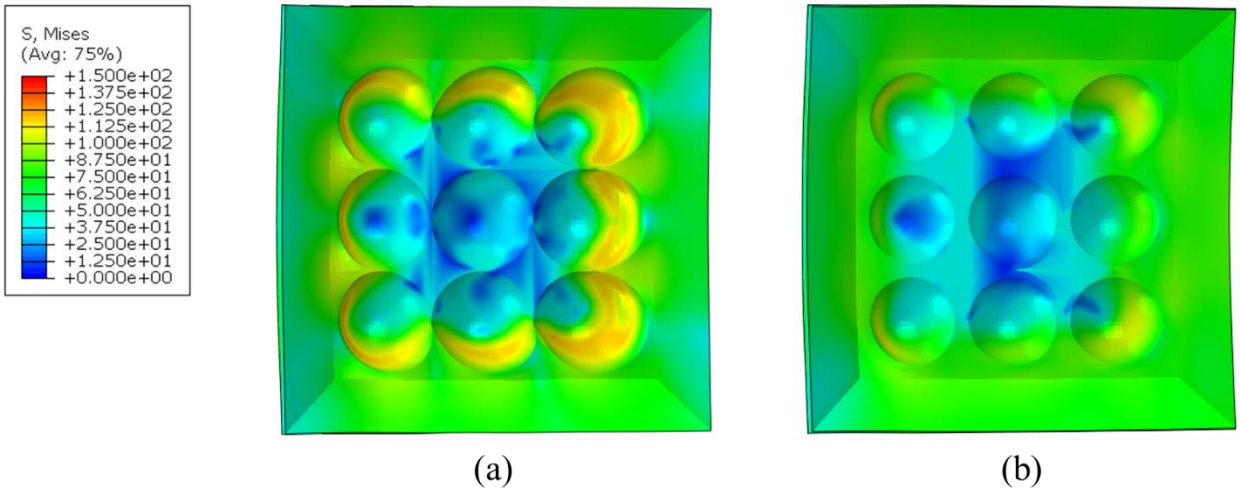

Figure 4.22. Stress distribution in the weld area in cases with base material failure for (a) undulated interface and (b) flat interface.

4.5. Conclusions

In this study, the influence of interfacial undulation on weld formation and performance were investigated based on experimental observation and finite element analysis. The lap-shear performance and corresponding weld attributes including bond density, post-weld thickness, undulation amplitude, and undulation size were investigated. Three-dimensional finite element models were built to predict the lap-shear performance of ultrasonically welded samples made using a fine and a coarse toothed anvil. The models were calibrated by the geometric input obtained from experiments. Elastic-plastic material with progressive ductile and shear failure were employed to describe the material property for both the base materials and the bonding layer. The bonding strength was predicted by matching the simulation results to experimental results, and the relationship between bonding strength and weld energy for both fine and coarse anvil cases was established. The model was validated by its good correspondence to the simulation results of the remaining experimental data. The influence of interfacial undulation under two failure modes,

interfacial separation and pull-out failure, was discussed based on the results from the finite element model. The main conclusions are:

1) The coarse anvil creates a more prominent interfacial undulation and maintains a greater post-weld thickness when weld energy is high.
2) The fine anvil creates a stronger weld in the initial stages of the process.
3) The interfacial undulation positively affects the lap-shear load carrying capacity when interfacial failure mode dominates, but negatively affects the lap-shear load carrying capacity when the failure mode transfers to pull-out or circumferential failure.

Moreover, the study of the influence of interfacial undulations on weld formation and performance also provides some insight into the weld formation in multi-layered USW when more undulations exist at the top interfaces in this research. The findings in this chapter help explain the weld formation in 3CC and 3AC in Chapter 3. Prominent undulations, especially at the top interface result in weaker local bonding. However, the weld formation delay may be compensated by more concentrated stress, larger strain, and higher interfacial temperature. To verify this assumption, further study correlating thermal-mechanical behavior and bonding formation is required.

References

[1] Lee, D. and Cai, W., 2017. The effect of horn knurl geometry on battery tab ultrasonic welding quality: 2D finite element simulations. Journal of Manufacturing Processes, 28, pp.428-441.

[2] Feng, M.N. and Luo, Z., 2019. Interface morphology and microstructure of high-power ultrasonic spot welded Mg/Al dissimilar joint. Science and Technology of Welding and Joining, 24(1), pp.63-78.

[3] Satpathy, M.P. and Sahoo, S.K., 2016. Microstructural and mechanical performance of ultrasonic spot welded Al–Cu joints for various surface conditions. Journal of Manufacturing Processes, 22, pp.108-114.

[4] Lu, Y., Song, H., Taber, G.A., Foster, D.R., Daehn, G.S. and Zhang, W., 2016. In-situ measurement of relative motion during ultrasonic spot welding of aluminum alloy using Photonic Doppler Velocimetry. Journal of Materials Processing Technology, 231, pp.431-440.

[5] Lin, J.Y., Nambu, S. and Koseki, T., 2019. Evolution of bonding interface during ultrasonic welding between steel and aluminium alloy. Science and Technology of Welding and Joining, 24(1), pp.83-91.

[6] Fujii, H.T., Endo, H., Sato, Y.S. and Kokawa, H., 2018. Interfacial microstructure evolution and weld formation during ultrasonic welding of Al alloy to Cu. Materials Characterization, 139, pp.233-240.

[7] De Vries, E., 2004. Mechanics and mechanisms of ultrasonic metal welding (Doctoral dissertation, The Ohio State University).

[8] Mariani, E. and Ghassemieh, E., 2010. Microstructure evolution of 6061 O Al alloy during ultrasonic consolidation: an insight from electron backscatter diffraction. Acta Materialia, 58(7), pp.2492-2503.

[9] Kreye, H., 1977. Melting phenomena in solid state welding processes. Weld. J, 56(5), pp.154-158.

[10] Lee, S.S., Kim, T.H., Hu, S.J., Cai, W.W., Abell, J.A. and Li, J., 2013. Characterization of joint quality in ultrasonic welding of battery tabs. Journal of Manufacturing Science and Engineering, 135(2), p.021004

[11] Wu, X., Liu, T. and Cai, W., 2015. Microstructure, welding mechanism, and failure of Al/Cu ultrasonic welds. Journal of Manufacturing Processes, 20, pp.321-331. Grigorovich, V.K., 1989. The metallic bond and the structure of metals.

[12] Zhang, Z., Wang, K., Li, J., Yu, Q. and Cai, W., 2017. Investigation of interfacial layer for ultrasonic spot welded aluminum to copper joints. Scientific reports, 7(1), p.12505.

[13] Shakil, M., Tariq, N.H., Ahmad, M., Choudhary, M.A., Akhter, J.I. and Babu, S.S., 2014. Effect of ultrasonic welding parameters on microstructure and mechanical properties of dissimilar joints. Materials & Design, 55, pp.263-273.

[14] Jahn, R., Cooper, R. and Wilkosz, D., 2007. The effect of anvil geometry and welding energy on microstructures in ultrasonic spot welds of AA6111-T4. Metallurgical and Materials Transactions A, 38(3), pp.570-583.

[15] Bakavos, D. and Prangnell, P.B., 2010. Mechanisms of joint and microstructure formation in high power ultrasonic spot welding 6111 aluminium automotive sheet. Materials Science and Engineering: A, 527(23), pp.6320-6334.

[16] Komiyama, K., Sasaki, T. and Watanabe, Y., 2016. Effect of tool edge geometry in ultrasonic welding. Journal of Materials Processing Technology, 229, pp.714-721.

[17] Barton, N. and Choubey, V., 1977. The shear strength of rock joints in theory and practice. Rock mechanics, 10(1-2), pp.1-54.

[18] Barton, N. and Bandis, S., 1982, January. Effects of block size on the shear behavior of jointed rock. In The 23rd US symposium on rock mechanics (USRMS). American Rock Mechanics Association.

[19] Barton, N., Bandis, S. and Bakhtar, K., 1985, June. Strength, deformation and conductivity coupling of rock joints. In International journal of rock mechanics and mining sciences & geomechanics abstracts (Vol. 22, No. 3, pp. 121-140). Pergamon.

[20] Zeng, Q.G. and Sun, C.T., 2001. Novel design of a bonded lap joint. AIAA journal, 39(10), pp.1991-1996.

[21] Melograna, J.D. and Grenestedt, J.L., 2004. Revisiting a wavy bonded single lap joint. AIAA journal, 42(2), pp.395-402.

[22] Zavattieri, P.D., Hector, L.G. and Bower, A.F., 2007. Determination of the effective mode-I toughness of a sinusoidal interface between two elastic solids. International Journal of Fracture, 145(3), pp.167-180.

[23] Cordisco, F.A., Zavattieri, P.D., Hector Jr, L.G. and Bower, A.F., 2012. Toughness of a patterned interface between two elastically dissimilar solids. Engineering Fracture Mechanics, 96, pp.192-208.

[24] Li, B.W., Zhao, H.P., Qin, Q.H., Feng, X.Q. and Yu, S.W., 2012. Numerical study on the effects of hierarchical wavy interface morphology on fracture toughness. Computational Materials Science, 57, pp.14-22.

[25] Hirsch, F. and Kästner, M., 2017. Microscale simulation of adhesive and cohesive failure in rough interfaces. Engineering Fracture Mechanics, 178, pp.416-432.

[26] Jaiswal, P.R., Hirulkar, N.S., Papadakis, L., Sundaram, K.K. and Joshi, N.B., 2018. Parametric study of non flat interface adhesively bonded joint. Materials Today: Proceedings, 5(9), pp.17654-17663.

[27] Razavi, S.M.J., Berto, F., Peron, M. and Torgersen, J., 2018. Parametric study of adhesive joints with non-flat sinusoid interfaces. Theoretical and Applied Fracture Mechanics, 93, pp.44-55.

[28] Kim, W.S., Yun, I.H., Lee, J.J. and Jung, H.T., 2010. Evaluation of mechanical interlock effect on adhesion strength of polymer–metal interfaces using micro-patterned surface topography. International Journal of Adhesion and Adhesives, 30(6), pp.408-417.

[29] Zhou, B., Thouless, M.D. and Ward, S.M., 2005. Determining mode-I cohesive parameters for nugget fracture in ultrasonic spot welds. International journal of fracture, 136(1-4), pp.309-326.

[30] Zhou, B., Thouless, M.D. and Ward, S.M., 2006. Predicting the failure of ultrasonic spot welds by pull-out from sheet metal. International journal of solids and structures, 43(25-26), pp.7482-7500.

[31] Xi, L., Banu, M., Jack Hu, S., Cai, W. and Abell, J., 2017. Performance prediction for ultrasonically welded dissimilar materials joints. Journal of Manufacturing Science and Engineering, 139(1).

[32] Kafkalidis, M.S. and Thouless, M.D., 2002. The effects of geometry and material properties on the fracture of single lap-shear joints. International Journal of Solids and Structures, 39(17), pp.4367-4383.

[33] Tran, V.X. and Pan, J., 2010. Effects of weld geometry and sheet thickness on stress intensity factor solutions for spot and spot friction welds in lap-shear specimens of similar and dissimilar materials. Engineering Fracture Mechanics, 77(9), pp.1417-1438.

[34] Cahoon, J.R., Broughton, W.H. and Kutzak, A.R., 1971. The determination of yield strength from hardness measurements. Metallurgical transactions, 2(7), pp.1979-1983.

[35] Tiryakioğlu, M., Robinson, J.S., Salazar-Guapuriche, M.A., Zhao, Y.Y. and Eason, P.D., 2015. Hardness–strength relationships in the aluminum alloy 7010. Materials Science and Engineering: A, 631, pp.196-200.

[36] Dassault Systems, 2011. Abaqus Analysis User's Manual (v.6.11), Dassault Systems, Providence, RI

Chapter 5 Enhancement of Process Robustness in Multi-Layered Ultrasonic Welding by Localized Preheating

Abstract

Multilayered ultrasonic welding (USW) is widely used in joining of electrodes or tabs in lithium-ion batteries. This chapter proposes a localized preheating method to improve the process robustness and studies the effects of preheating temperature on the weld process and performance experimentally and numerically. The experimental results indicate that weld formation can be accelerated and the weld strength can be improved with process preheating, especially at the interface closest to the anvil. The effect of preheating is most significant during the early stage of the process, and diminishes as the process progresses. Numerical models reveal the underlying mechanisms influencing the temperature distribution, workpiece motion, and stress distribution of preheating on the welding process. Preheating improves the robustness of multilayered USW joints.

---

* The content of this chapter will be submitted to *ASME Journal of Manufacturing Science and Engineering*.

5.1. Introduction

Ultrasonic welding (USW) is an effective process for welding similar and dissimilar materials with highly conductive and reflective properties [1-4]. During the process, workpieces are tightly clamped between the sonotrode horn and anvil and forced to vibrate along with the vibrating tool tip at an ultrasonic frequency (typically 20 kHz [1]). The high-frequency oscillations generate reciprocating shearing at the faying surfaces, flatten the local surface asperities, disperse oxides and contaminants, and create intimate metal-to-metal contact at the interface that allows the formation of solid-state bonding. The process is typically completed within 1 second. The maximum temperature in the workpieces is normally less than half of the absolute melting temperature of the substrate materials [5-6]. Thus, the inherent nature of the USW process makes it suitable for joining multiple stack-ups of varying thickness and material combinations, especially for soft thin materials. However, some challenges exist in welding hard and thick materials.

In recent years, there has been growing demand for joining multiple stack-ups of similar and dissimilar metals when manufacturing electric vehicle batteries, lightweight automotive structures, biomedical devices, and electronic components. One large challenge in applying ultrasonic welding to multi-layered joining is the lack of process robustness. Several studies of multi-layered USW have shown inconsistent weld quality at different interfaces. Lee *et al.* [7] tracked the motion of all workpieces in USW of four-layered Cu sheets by high speed camera and found that bonds at different interfaces did not form simultaneously. Shin *et al.* [8] studied multi-layered Al-Cu USW with different configurations and found interfacial bonding strength highly depended on interface location and weld configuration. Similar observations were also reported by Das *et al.* [5] in a study of process robustness for ultrasonically welded multi-layered Al-Cu sheets. The literature has shown that it is challenging to form satisfactory bonding at the interface

between dissimilar materials and/or thicker workpieces. Inconsistent weld quality at different interfaces narrows the process window and significantly reduces the process robustness. To improve the process robustness and weldability for hard and thicker materials in USW, a deeper understanding of the fundamental physics of the process and innovative approaches to improve the process are desirable.

USW is a complex process that involves thermal, mechanical, and metallurgical phenomena. The interfacial temperature and strain conditions are difficult to measure experimentally and comprehensive understanding of the fundamental physics in the process has not been developed. Several attempts have been made to investigate the thermal-mechanical performance in USW process using the finite element method (FEM). Siddiq and Ghassemieh [9] proposed a three-dimensional (3D) model to investigate the thermal-mechanical behavior in ultrasonic consolidation. Their material model, including thermal and ultrasonic softening, was discussed in their study. Elangovan *et al.* [10] developed a two-dimensional (2D) model with heat generated by friction and plastic deformation to investigate the temperature distribution in USW and found the peak temperature was at the center of the weld interface. Kim *et al.* [11] used a 3D model of Al USW and found significant effects of frictional heating on plastic deformation during the process. Zhang and Li [12-13] developed thermal-mechanical models for ultrasonic consolidation and used this model to investigate the effect of the substrate material dimensions. Lee *et al.* [14-15] simulated the multi-layered USW process using a combination of isotropic and kinematic hardening of the material and investigated the influence of sonotrode geometry on strain and temperature distributions. Shen *et al.* [16] included dynamic recrystallization in modeling USW of similar materials, while Li *et al.* [17] considered the diffusion and formation of intermetallic compounds (IMCs) in USW of dissimilar materials and modeled the resistance heat

assisted USW process [18]. Jedrasiak and Shercliff [19] proposed a more computationally efficient FEM by separating thermal and plastic deformation. In summary, FEM has proven to be an efficient method to investigate the thermal-mechanical behavior in USW and for process optimization.

Innovative approaches are needed to enhance the process robustness based on better understanding of the underlying physics. Thermal assistance has proven to be effective in controlling and improving the robustness of manufacturing process quality. For example, preheating has been used to reduce the cooling rate and thus prevent the formation of brittle phases in fusion welding [20-21]. Thermal-enhanced machining has been widely used to improve machinability and tool life [22–24]. Elevated temperature has also been used in solid-state welding. Liu *et al*. [25] and Sharma *et al.* [26] employed thermal enhancement in frictional stir welding to soften materials and improve tool reliability. The concept of thermally enhanced USW has also been investigated by several researchers. Gunduz *et al.* [27] proved that elevated temperature can enhance diffusion during USW of Zn–Al. Cao's research team [18, 28] employed resistance heating to enhance the weldability of two-layered Al–Cu USW. These results indicate that the synergistic effects of ultrasonic vibration and Joule heating significantly increases the weld temperature, stimulate interface diffusion, and therefore improves weld quality. A simulation conducted by Lee *et al.* [14] predicted that localized preheating might enable a more uniform temperature distribution and hence improve weldability at preheated interfaces.

This chapter discusses the influence of localized preheating on the weldability and robustness of a multi-layered USW for Ni-coated Cu sheets. A 2D FEM model was established to investigate the thermal-mechanical performance with and without preheating. The remainder of this chapter is organized as follows: Section 5.2 introduces the experimental setup and results;

Section 5.3 describes the establishment of the numerical model; Section 5.4 discusses the thermal-mechanical behavior in the multi-layered USW process under different preheating temperatures; and Section 5.5 summarizes the findings and presents the conclusions.

5.2. Experimental Study

In this study, three layers of thin Ni-coated Cu tabs (0.2 mm in thickness) were welded on top of a thick Ni-coated Cu bus-bar (0.9 mm in thickness) in an overlapped configuration and designated as a '3CC' joint. Both tabs and bus-bar were 41 mm in width and 45 mm in length. The Ni-coating was 2.4 μm for the tabs and 1.5 μm for bus-bar. The weld was made at the center of the metal sheets and the vibration direction was parallel to the shorter side. Four different conditions were investigated, including three preheating cases and a non-preheated case as the control group. The change of the lap-shear performance was measured and used to evaluate the influence of preheating at the interface between the tab and bus-bar, and between the outermost tabs. This section presents the experimental setup and results for the study of localized preheating effects.

5.2.1. Ultrasonic Welding Process with Preheating

The multi-layered USW samples were made using a Branson^{TM} series L20 USW machine under the energy-control mode with a 5000 W maximum power and at a 20 kHz constant vibration frequency. The weld energy was varied while clamping pressure and vibration amplitude were fixed as 20 psi and 65 μm, respectively. Ten weld energy levels were used ranging from 800 J to 2800 J in 200 J increments. The process parameters were determined based on a screening test to cover various weld qualities, from cold to good to over-weld. At each weld energy, three

preheating temperatures, 50 ºC, 100 ºC and 150 ºC, were used to study the preheating effects. A non-preheated group was also used as a benchmark whose details are presented in Chapter 3. Four replicates were fabricated for each process setting, where three samples were used for lap-shear tests and one was reserved for metallurgical analysis.

Preheating was accomplished using a specially designed apparatus depicted in Fig. 5.1, and only the bus-bar was preheated. A K-type thermocouple was attached to the bus-bar outside of the weld area to monitor the temperature. First, the bus-bar was heated uniformly on the heating plate to a temperature 10–20 ºC higher than the desired preheating temperature. Then it was moved to the fixture via the ramp structure shown in Fig. 5.1. As soon as the bus-bar was in position and reached the desired preheating temperature, the other three tabs were quickly placed onto it and the weld was performed.

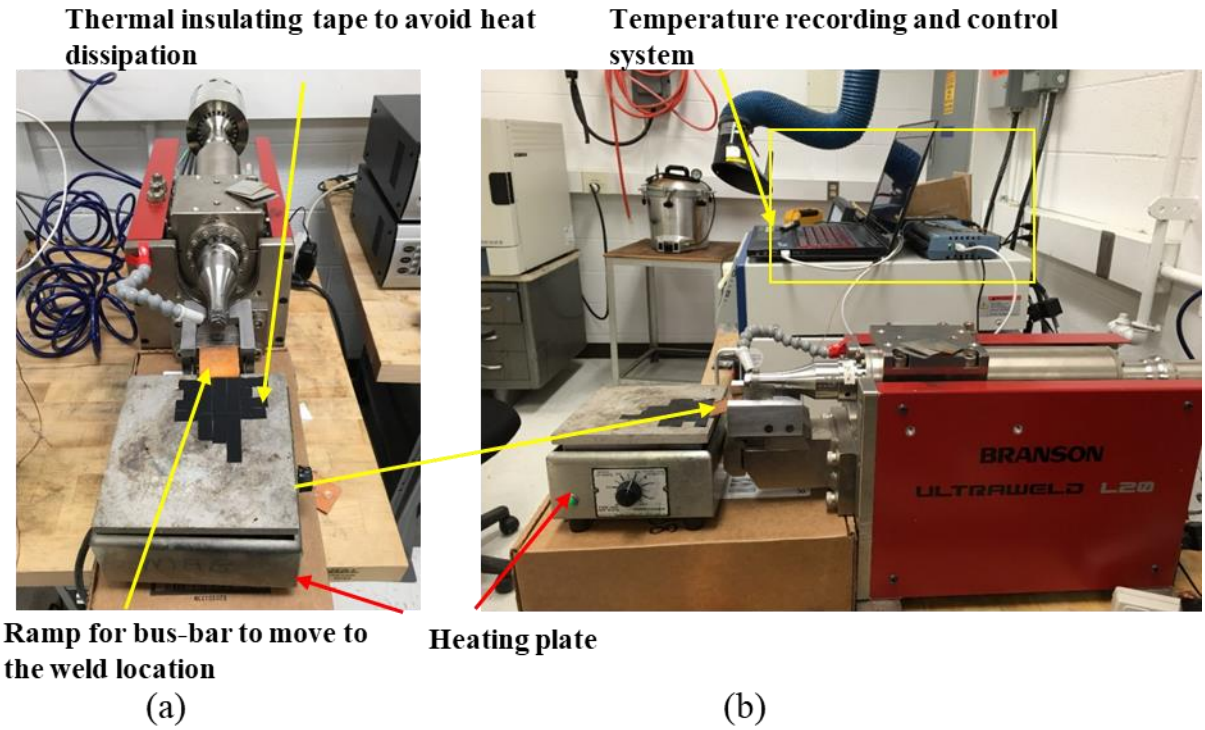

Figure 5.1. USW system setup for preheating showing (a) top view and (b) side view.

Metallurgical analysis was performed using an optical microscope to characterize the change in the interface microstructure as weld energy and preheating temperature were varied. The samples were cross-sectioned at the center of the weld in the direction parallel to weld vibration. Lap-shear test was performed at the interface between the tab and bus-bar and between the outermost tabs, which are defined as the bottom and the top interfaces, respectively. The details of the cross-sectioning and lap-shear test are presented in Chapter 3.

5.2.2. Experimental Results of Preheating

The maximum lap-shear load versus weld energy under different preheating temperatures is presented in Fig. 5.2. The change of the lap-shear load at the bottom interface is show in Fig. 5.2 (a). The results indicate that preheating increases the lap-shear load carrying capacity most effectively for weld energy up to 1600 J. Higher preheating temperature leads to higher peak lap-shear load. The minimum weld energy required to form a measurable weld at the bottom interface decreases as preheating temperature increases. As discussed in Chapter 3, only Ni-Ni bonds with minimal undulations form in samples made at 1600 J or lower welding energy without preheating. The effect of preheating becomes less significant as welding energy increases. At moderate weld energy, ranging from 1600 J to 2000 J, the lap-shear load at the bottom interface is slightly enhanced by preheating, and the optimal preheating temperature is 100 ºC under the studied conditions. During this stage, interfacial undulations initiate and develop as the process proceeds. Preheating effects diminish when the weld energy is more than 2000 J, as Cu–Cu bonds increase along with more severe interfacial undulation and mechanical interlocking. In comparison, there is no significant change of the lap-shear load at the top interface for different preheating conditions, as shown in Fig. 5.2 (b).

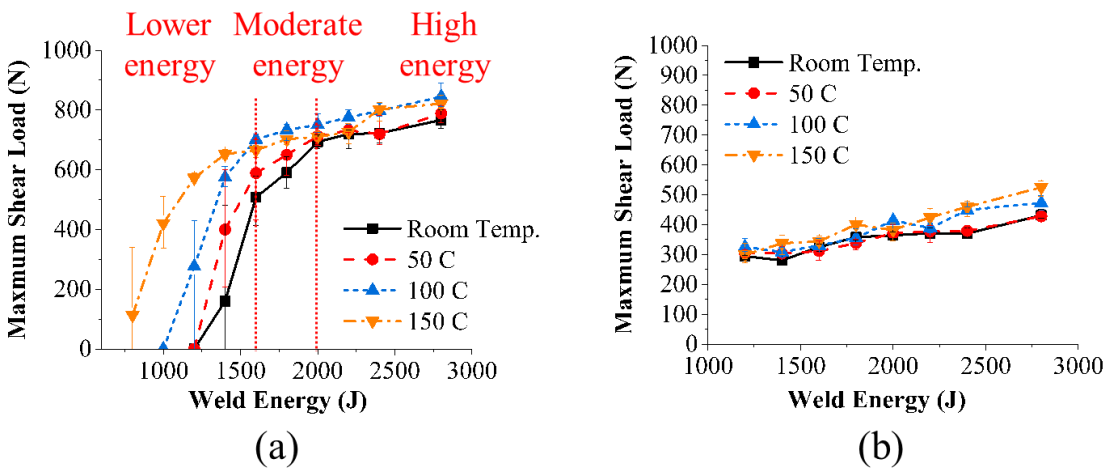

Figure 5.2. Lap-shear results for preheated and non-preheated samples at: (a) bottom interface and (b) top interface.

Optical microscopic images of samples produced at three temperatures and three energy levels are shown in Fig. 5.3. It can be observed in Fig. 5.3 (a) that at 1200 J, the bottom interface is joined only when the preheating temperature reaches 150 ºC. Significantly different joint conditions at the bottom interface can be found in samples welded at 1600 J, as shown in Fig. 5.3 (b). The bottom interface is joined by Ni–Ni bonds with negligible interfacial undulations without preheating. When the sample is preheated to 50 ºC, visible undulation starts to form, resulting in higher joint strength, as studied in Chapter 4. When the preheating temperature rises to 150 ºC, more undulations are formed at the bottom interface, and some of the Ni-coating breaks down, allowing for Cu–Cu bonds. However, in the samples welded at 2000 J, the joint features are very similar at different preheating temperatures, which can be seen in Fig. 5.3 (c).

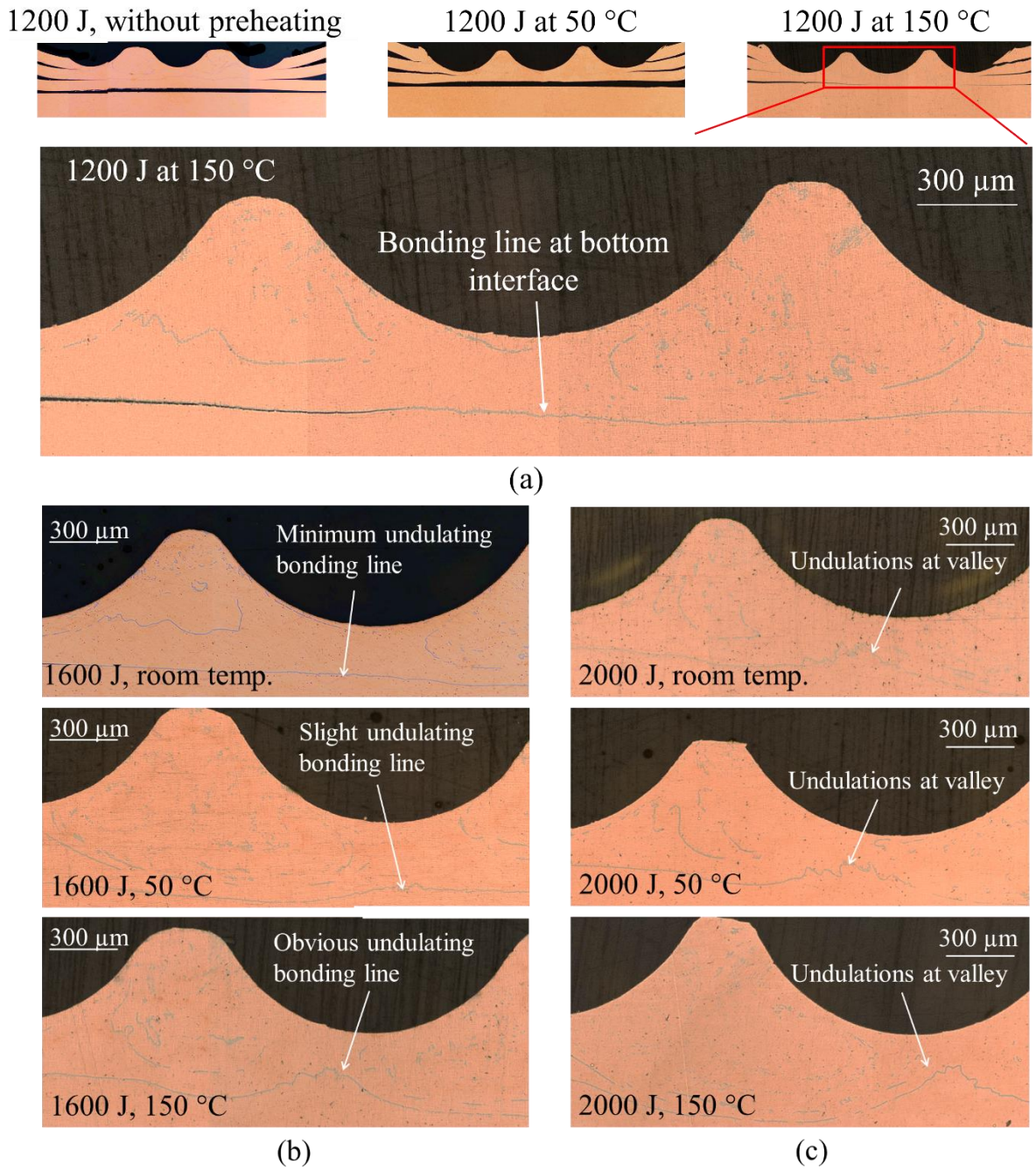

Figure 5. Microstructural analysis of samples under both ambient and preheated conditions with (a) 1200 J, (b) 1600 J, and (c) 2000 J.

Lap-shear load test results show that localized preheating at the bus-bar before welding enhances the lap-shear load carrying capacity at the bottom interface but does not affect the top interface. A wider range of weld energies can be used to achieve a quality weld at different

interfaces with preheating, and thus an improved weldability and process robustness for the multi-layered USW of this study is demonstrated.

5.3. Finite Element Model

Finite element models were developed to investigate the effect of preheating by predicting the thermal-mechanical performance during the welding process under different thermal conditions, and to optimize the preheating temperature. The models were built using Abaqus/Explicit 6.19 because it is an effective solver for dynamic thermal-mechanically coupled simulations with severe plastic deformation. This section illustrates the establishment of the model based on four key elements and describes the procedure of the simulation.

5.3.1. Model Establishment

Presented in this section is the establishment of a model incorporating four key elements. The key elements required in the construction of the USW finite element model include the geometry of the model, the boundary conditions, interactions between different components and their constitutive material properties, and the heat generation and conduction during the process.

Model Geometry

The geometry of the model is show in Fig. 5.4. To reduce the computational cost of the process simulation, a 2D plane strain model representing the geometry at the center of the weld configuration parallel to the vibration direction was built. A schematic of the weld configuration with sonotrode tip and anvil and the specified plane cut for the model is shown in Fig. 5.4 (a). The model consists of a sonotrode tip, an anvil, three Cu tabs with 0.2 mm thickness, and a bus-bar

with 0.9 mm thickness. The geometry of the tools are matched to the knurl patterns of the actual tip and anvil. The width of the workpieces was set as 41 mm.

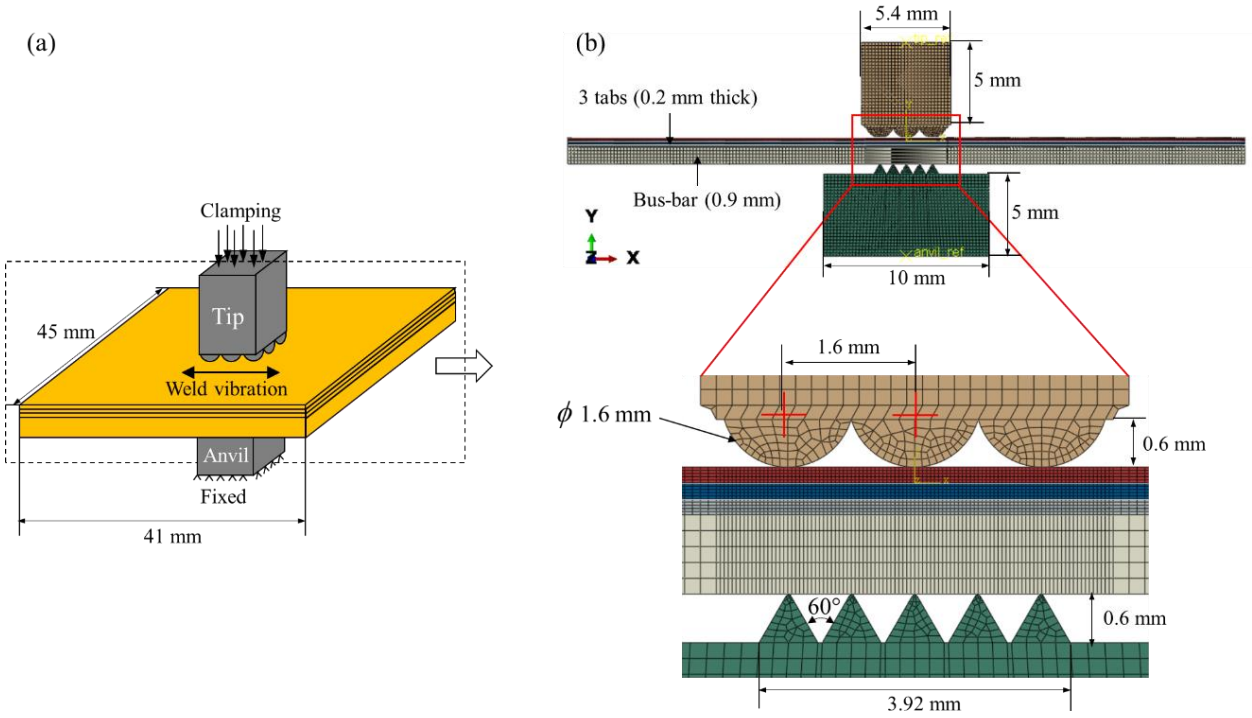

Figure 5.4. Geometry and mesh of the finite element model: (a) schematic of the weld configuration, and (b) details of the 2D model

Mesh

Most of the model was meshed using a CPE4RT element, which is a 4-node plane strain thermally coupled quadrilateral element with reduced integration and hourglass control. A small portion of the anvil tip was meshed using a CPE3T element, which is similar to the CPE4RT but is triangular in shape. The total number of elements for the model was 10,658. The sonotrode tip and anvil were constrained as solid bodies and therefore did not require very fine meshes. The main body of the tool set was meshed with a 0.2 mm average element size, and the tool knurls were meshed with a 0.1 mm average element size to ensure an accurate description of the geometry. All workpieces were partitioned into two, one part representing the weld area with a

width of 5 mm, while the remainder was the unwelded area. The weld area was meshed using 0.05 mm element and the unwelded area was meshed using 0.2 mm element. Both tabs and bus-bar had 5 layers of element in the thickness direction.

Boundary Conditions

The workpieces were clamped by the sonotrode tip and anvil as show in Fig. 5.4. The anvil was fixed at the bottom side for the entire procedure. The sonotrode tip was pressed by a uniformly distributed constant clamping pressure of 40 MPa at its upper surface. This pressure is equivalent to the 20 psi clamping pressure set as the Branson^{TM}'s clamping load and the size of the tool. When vibration is initiated, the tip vibrates in the horizontal direction (x-direction) with a 65 μm peak-to-peak amplitude at a frequency of 20 kHz. The tip can move only in the horizontal and vertical directions and is constrained from rotation. The workpieces were tightly clamped by the tool and thus no additional displacement constraint was applied. A gravitational acceleration, $g = 9.81$ m/s^2, was applied to all the workpieces. A predefined 25 ºC room temperature was applied to the entire model and was used as the initial temperature. For preheated cases, a predefined temperature equal to the preheating temperature in the experiment was set for the bus-bar. The model was assumed to be adiabatic and there was no heat exchange between the model and the environment.

Interactions

Two types of contact were used in the 2D model. The first was general contact between two surface pairs, including the upper surface of the outermost tab in contact with the lower surface of the tip pair, and the lower surface of bus-bar in contact with the upper surface of the anvil pair. The tool surface was defined as master surface to avoid unexpected penetration. In comparison,

contact within the workpieces was set as a kinematic surface-to-surface contact. A constant friction coefficient was set between the contact surfaces for the entire procedure. The friction coefficient, μ, was set as infinite and 0.3 between the tool and workpiece and between the workpieces, respectively [14, 29]. Heat conduction, κ, between the components was also included, with the conductance set to 235 $mW/mm^2 \cdot {}^oC$ [14]. The heat conduction allows continuous heat transfer from one component to the other.

Constitutive Material Properties

Two materials were used in this model, one was steel, used for the tip and anvil, and the other was for Cu, which had thermal-mechanically coupled properties. In practice, the steel for the tool was hardened with a chromium coating. The deformation of the tool is much smaller than the workpiece, and thus was assumed to be rigid body with infinite strength. Previous experimental [11] and simulation [17] results also indicate a much lower temperature in the tool than the workpieces. Therefore, the thermal effect on the material properties of the steel was neglected in this study. The steel and Cu material properties are listed in Table 5.1 [14].

Table 5.1 Material Properties of Steel and Cu[14]

Property	Steel	Cu
Density (kg/mm^3)	7.8×10^3	8.94×10^3
Young's Modulus (GPa)	200	Change with temperature
Poison's ratio	0.27	0.35
Thermal conductivity ($W \cdot m^{-1} \cdot {}^oC^{-1}$)	80	Change with temperature
Specific heat ($J \cdot kg^{-1} \cdot {}^oC^{-1}$)	440	Change with temperature

The workpieces in USW are subject to both normal and cyclic tangential loadings. During the process the material hardening due to cyclic loading and material softening due to elevated temperature were considered. A basic assumption is that the total strain rate, $\dot{\boldsymbol{\varepsilon}}$, is composed of an elastic component, $\dot{\boldsymbol{\varepsilon}}^{\boldsymbol{el}}$, and a plastic component, $\dot{\boldsymbol{\varepsilon}}^{\boldsymbol{pl}}$, as shown in Eqn. (5.1) [31]:

$$\dot{\boldsymbol{\varepsilon}} = \dot{\boldsymbol{\varepsilon}}^{\boldsymbol{el}} + \dot{\boldsymbol{\varepsilon}}^{\boldsymbol{pl}} \tag{5.1}$$

The elastic behavior can be described by a scale product of elastic strain, $\boldsymbol{\varepsilon}^{\boldsymbol{el}}$, and a 4th order elasticity tensor, $\boldsymbol{C}$ [31]:

$$\boldsymbol{\sigma} = \boldsymbol{C}\boldsymbol{\varepsilon}^{\boldsymbol{el}} \tag{5.2}$$

where $\boldsymbol{\sigma}$ is the 2nd order stress. The plastic behavior follows a flow rule associated with a yield surface [31]:

$$\dot{\boldsymbol{\varepsilon}}^{\boldsymbol{pl}} = \dot{\bar{\varepsilon}}^{pl}\partial f(\boldsymbol{\sigma} - \boldsymbol{\alpha})/\partial\boldsymbol{\sigma} \tag{5.3}$$

where $f(\boldsymbol{\sigma} - \boldsymbol{\alpha}) = \sigma_0$ describes the yield surface and σ_0 is the yield stress, $\dot{\bar{\varepsilon}}^{pl} = \sqrt{\frac{2}{3}\dot{\boldsymbol{\varepsilon}}^{\boldsymbol{pl}}\dot{\boldsymbol{\varepsilon}}^{\boldsymbol{pl}}}$ is the equivalent plastic strain rate, and $\boldsymbol{\alpha}$ is the back stress that is controlled by plastic hardening model.

The plastic hardening model has two components, one is an isotropic hardening component, which describes the size of the yield surface according to the yield stress σ_0, and the other is a kinematic hardening component, which describes the translation of the yield surface via $\boldsymbol{\alpha}$. Figure 5.5 shows the effect of strain hardening on the yield locus for isotropic, kinematic, and the mixed hardening used in this study [32]. The mathematical model used for isotropic hardening is:

$$\sigma^0 = \sigma|_0 + Q_\infty(1 - e^{-b\bar{\boldsymbol{\varepsilon}}^{\boldsymbol{pl}}}) \tag{5.4}$$

where σ^0 represents the yield surface size subjecting to the equivalent plastic strain, $\bar{\boldsymbol{\varepsilon}}^{\boldsymbol{pl}}$, and yield stress at zero plastic strain, $\sigma|_0$. Q_∞ and b are material parameters. The mathematical model used for kinematic hardening is:

$$\dot{\boldsymbol{\alpha}} = C(\boldsymbol{\sigma} - \boldsymbol{\alpha})\dot{\varepsilon}^{pl}/\sigma^0 - \gamma\boldsymbol{\alpha}\dot{\varepsilon}^{pl} \tag{5.5}$$

where C and γ are material parameters calibrated from cyclic test data, which were obtained from literature in this study [14].

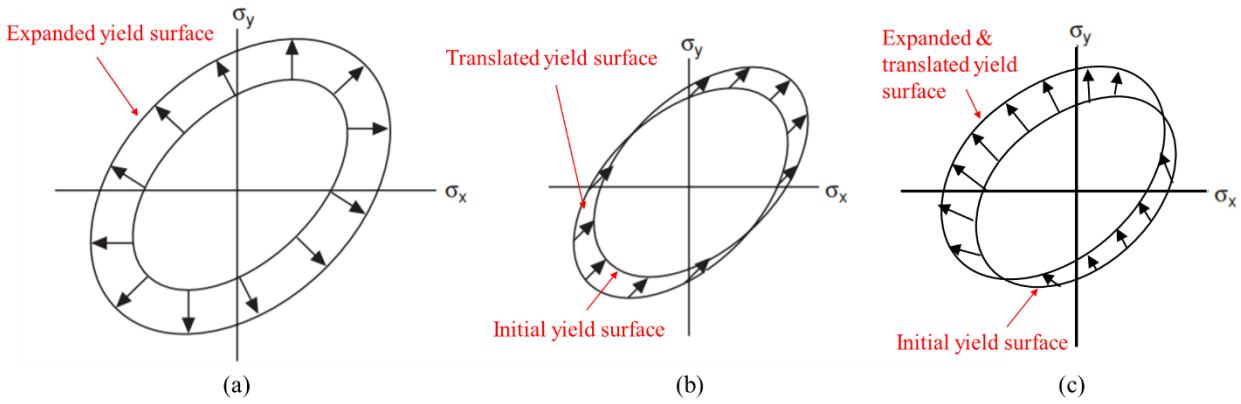

Figure 5.5. Schematics showing the effect of strain hardening on the yield locus: (a) isotropic hardening, (b) kinematic hardening, and (c) mixed hardening used in this study (adopted from [32]).

In addition to material hardening, material softening caused by elevated temperature was included in this study. An extension with temperature dependency for Eqns. 5.4 and 5.5 was applied to include the thermal softening effect. Therefore, the final hardening models used in this study are:

$$\sigma^0 = \left[\sigma|_0 + Q_\infty(1 - e^{-b\bar{\boldsymbol{\varepsilon}}^{\boldsymbol{pl}}})\right] f(T) \tag{5.6}$$

for isotropic hardening model, and

$$\dot{\boldsymbol{\alpha}} = [C(\boldsymbol{\sigma} - \boldsymbol{\alpha})\dot{\varepsilon}^{pl}/\sigma^0 - \gamma\boldsymbol{\alpha}\dot{\varepsilon}^{pl}]f(T) \tag{5.7}$$

for kinematic hardening model, where $f(T)$ is the function subjected to temperature dependent initial yield strength. The function was adopted from [35], and can be expressed as:

$$f(T) = \begin{cases} a_0 T + b_0 & if\ T \le T_1 \\ 1 - [(T - T_1)/(T_m - T_1)]^n & if > T_1 \end{cases} \tag{5.8}$$

where T_1 is the transition temperature and T_m is the melting temperature in K. Parameters a_0, b_0, and exponent n are material constants. The values of the aforesaid parameters are summarized in Table 5.2 [14].

Table 5.2 Constants in Eqns. 5.4 to 5.8

Constant	Value
Q_∞	10
b	11
C	22300
γ	340
T_1	573
T_m	1358
a_0	-6.86×10^{-4}
b_0	1.004
n	0.4599

The temperature dependent material properties of the workpieces were obtained from Lee et al. [14] and are presented in Fig. 5.6. A polynomial fit curve was adopted to describe the Young's modulus of Cu as a function of temperature based empirical measurements, as shown in Fig. 5.6 (a). The purpose of using the fitted curve instead of the actual experimental number was to avoid

numerical instability due to scattered data points. The initial yield strength subjected to temperature is shown in Fig. 5.6 (b). Moreover, thermal properties of Cu were also included for the coupled thermal-mechanical analysis. The temperature dependent specific heat, thermal conductivity, and thermal expansions coefficient are presented in Figs. 5.6 (c) to (e) respectively.

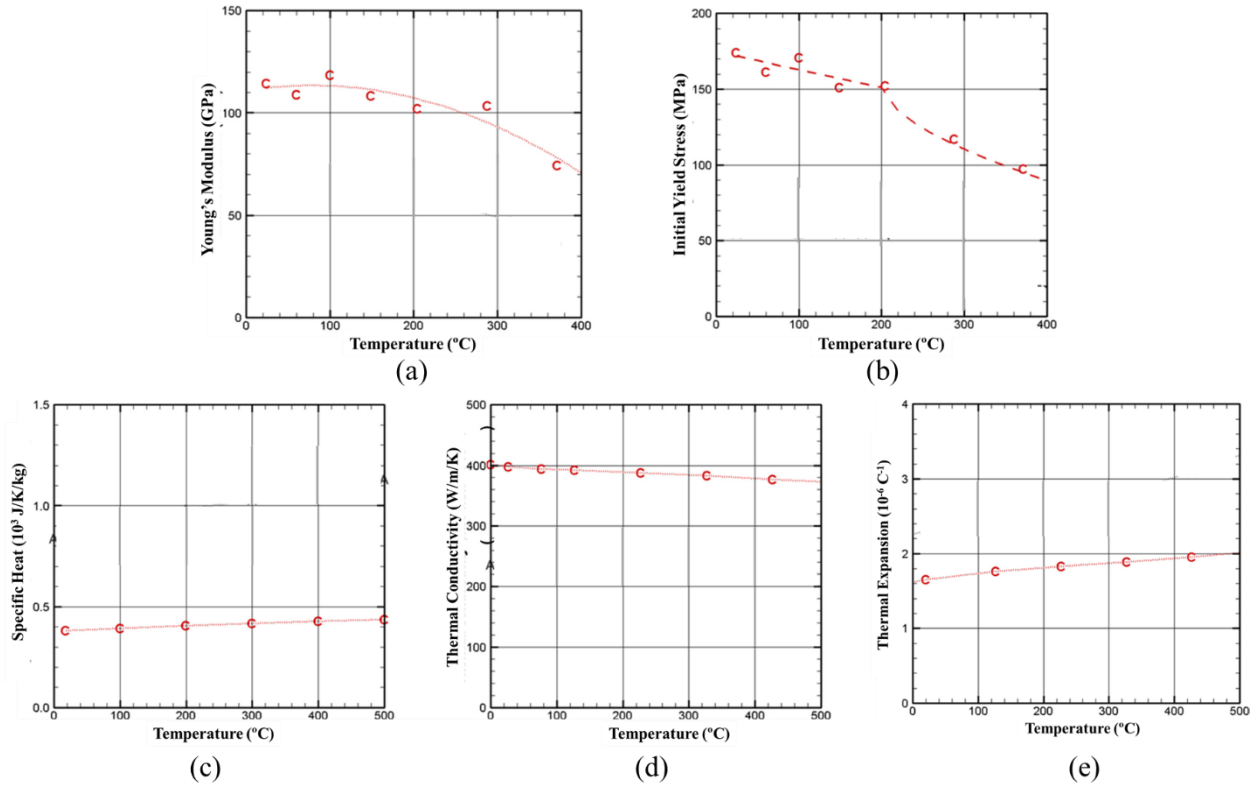

Figure 5.6. Temperature dependent mechanical properties of Cu: (a) Young's modulus, (b) initial yield stress, (c) specific heat, (d) thermal conductivity, and (e) thermal expansion (adopted from [14]).

Noticeably, thermal expansion introduces additional thermal strain, which is also included in the finite element model in the present study. The thermal strain, ε^{th}, can be expressed as [14]:

$$\varepsilon^{th} = \alpha(T)(T - T^0) - \alpha\left(T^i\right)\left(T^i - T^0\right) \tag{5.9}$$

where $\alpha(T)$ is the temperature dependent thermal expansion coefficient, and T^i and T^0 represent the initial and thermal expansion coefficient reference temperatures, respectively.

Heat Generation and Conduction

There are two sources of heat generation in USW, one caused by interfacial friction and the other induced by plastic deformation of the workpieces. The heat generated by friction, q_f, is a function of friction coefficient, μ, the relative slipping speed, $\dot{s}$, and fraction of frictional heat dissipation, η_f [31]:

$$q_f = \eta_f \mu \dot{s} \tag{5.10}$$

where η_f equals 0.65 in this study according to previous literature [14] and $\dot{s}$ is numerically determined in each computational step. The heat generated by plastic deformation is described by the stress and plastic strain rate with an inelastic heat fraction, η_p:

$$q_p = \eta_p \boldsymbol{\sigma} \dot{\boldsymbol{\varepsilon}}^{\boldsymbol{pl}} \tag{5.11}$$

The value of η_p was set as 0.8 based on experimental study [17].

The heat conduction within the model was governed by:

$$\rho c(T) \frac{\partial T}{\partial t} = -\vec{\nabla}\left(-k(T)\vec{\nabla}T\right) + Q \tag{5.12}$$

where ρ is the density, $c(T)$ is the temperature dependent specific heat shown in Fig. 5.6 (c), $k(T)$ is thermal conductivity shown in Fig. 5.6 (d). Q is the volumetric heat generation, which is attributed to plastic deformation and governed by Eqn. 5.11.

Another important thermal aspect is the heat conduction at the gaps between different components in the model. A gap introduces a discontinuity at the faying surfaces, and the heat

transfer across this discontinuity can be estimated using gap conductance, κ. The heat flux across the faying surfaces, q_g is defined as [31]:

$$q_g = \kappa \Delta T \tag{5.13}$$

where ΔT represents the temperature difference between the two contacting surfaces. The value of κ is determined by the dimensionless gap resistance, *G*, as [14]:

$$G = \frac{k_g}{\kappa d} \tag{5.14}$$

where k_g is the thermal conductivity of the gas in the gap, and *d* is an effective gap distance determined by surface roughness and clamping pressure. In the model, the properties of air at atmospheric pressure was used as the gas in the gaps and *G* was assumed to be one [14].

5.3.2. Simulation Procedure

A weld in USW is typically accomplished by a clamping and a welding step. The entire process cycle is finished with additional holding and unloading step. However, the latter two steps do not play a significant role in weld formation and were not considered in this study. The present model simulates the clamping and welding steps. During the clamping step, only a uniform clamping pressure mentioned in Section 5.3.1 was applied on the upper surface by the sonotrode tip. The pressure gradually increases from 0 to 40 MPa as a function of time. The step duration was set as 10 ms. After the clamping step, vibration of the sonotrode tip was initiated with amplitude ramped up from 0 to 65 μm within 5 ms and kept constant for the rest of the welding step. The weld duration was set as 0.02 second. Although the simulation time was much shorter than the actual weld time, for example at ~0.8 s for a weld made at 1200 J, it was found that running

the entire procedure would be too computationally expensive. However, insight of the influence of preheating temperature can still be obtained for a shorter weld time and can be extrapolated for longer weld times.

5.4. Simulation Results

This section presents and discusses the simulation results, including temperature, displacement, and stress distribution under different preheating conditions.

5.4.1. Temperature distribution

The simulated temperature distribution for the three preheating cases and the ambient condition case at the end of 0.2 sec weld time are presented in Fig. 5.7. All cases show the maximum temperature at the center of the weld and at the inner tabs (i.e., 2^{nd} and 3^{rd} tabs). The results agree with previous simulation using similar material properties from the literature [14]. The temperature distribution in the workpieces for the ambient condition in Fig. 5.7 (a) indicates that the maximum temperature is at the center of the top interface with 361 ºC and gradually decreases to 324 ºC at the bottom interface. A more uniformly distributed temperature distribution can be found in the case of 50 ºC preheating. In this case, all interfaces are around 340 ºC, as pointed out in Fig. 5.7 (b). The temperature at the top interface is lower than that in the ambient condition possibly due to reduction of relative motion at the top interface, which will be discussed in detail in Section 5.4.2. As preheating temperature increases, the temperature at the bottom interface increases to 368 ºC in the 100 ºC preheating case and 389 ºC in the 150 ºC preheating case, as shown in Figs. 5.7 (c) and (d). In the 100 ºC case, both the top and the middle interface have maximum temperature around 340 ºC. While in the 150 ºC case, peak temperature gradually declines from the bottom interface to the top interface. Overall, the temperature at the top interface

experiences slight decrease at the top interface with bottom layer preheated. The relative constancy of the top interface may help sustain the interfacial strength. The considerably increased temperature at the bottom interface may contribute to the acceleration of the interfacial weld formation.

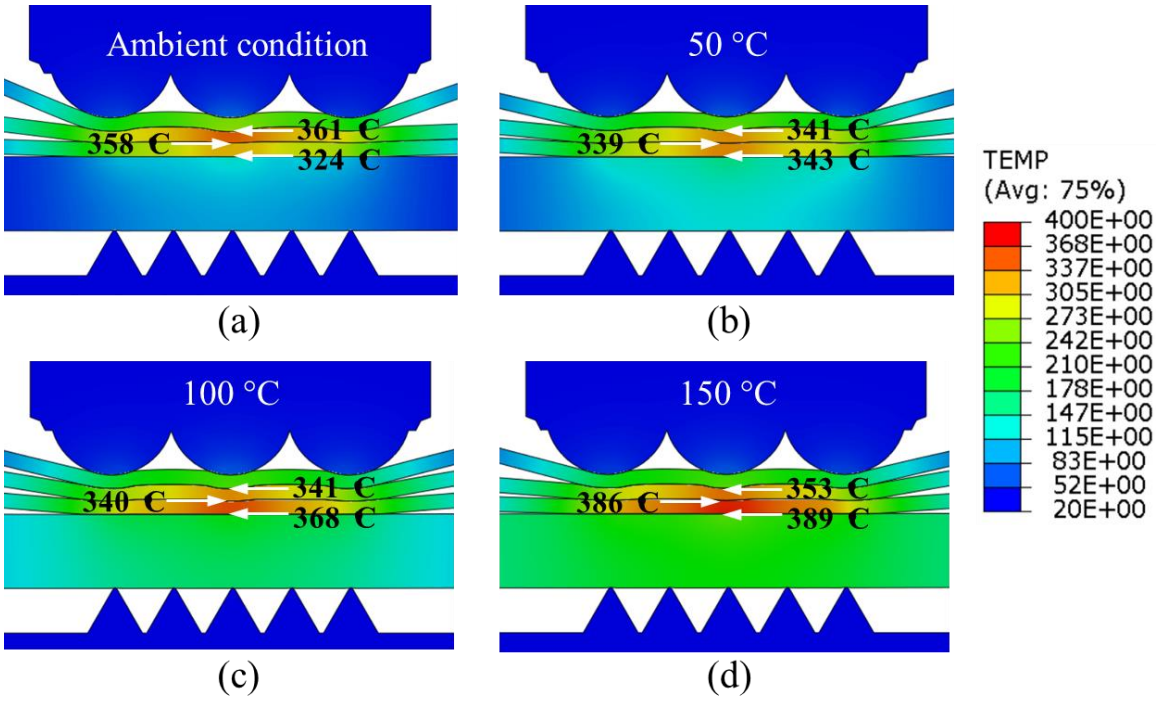

Figure 5.7. Temperature distribution in the workpieces for different bus-bar initial temperatures: (a) ambient condition, (b) 50 ºC, (c) 100 ºC, and (d) 150 ºC.

5.4.2. Workpiece Displacement

Relative motion in vibration direction at the interfaces play an important role in weld formation of USW. Larger relative motion can induce more frictional heat generation and accelerate the dissipation of surface contaminants, and thus accelerate the weld formation. The absolute relative motion of the workpieces under different conditions was tracked and the results are shown in Fig. 5.8. The relative motion at the top interface is defined as ‘tab 1-2’, at the middle interface is ‘tab 2-3’, and at the bottom interface is ‘tab 3-bus bar’. In the ambient condition, the

relative motions of the top and middle interfaces are about the same and gradually increase as time goes on. The relative motion at the bottom interface firstly increases, and then decreases to almost zero before slightly increases again, as shown in Fig. 5.8 (a). Since the process is at the very early stage of the process, the possibility to form large area bond is highly unlikely. Similar trend of relative motion at different interfaces can be found for the 50 ºC case, as shown in Fig. 5.8 (b). The relative motion at the bottom interface continuously increases for 100 ºC and 150 ºC preheating. The larger relative motion at the bottom interface introduces more frictional heat dissipation and enhances the weldability at the bottom interface.

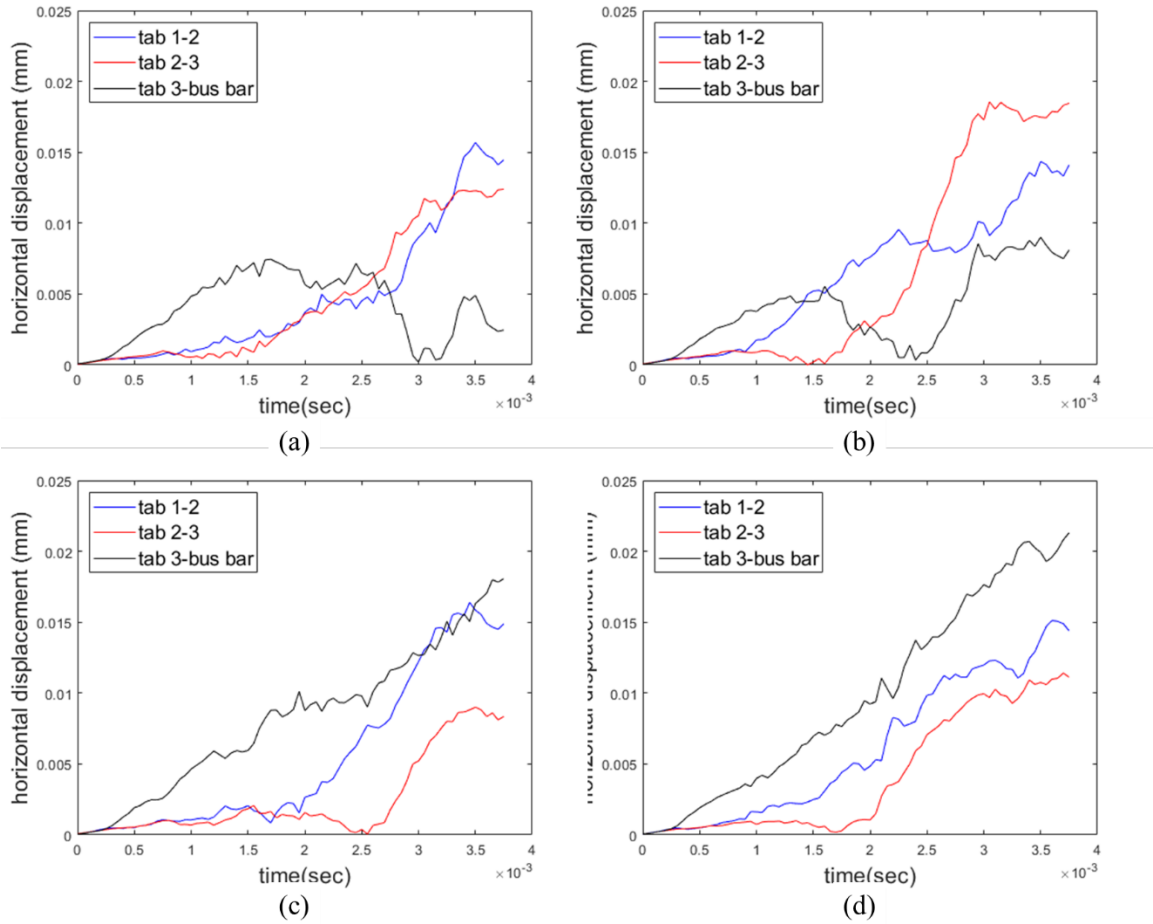

Figure 5.8. Horizontal displacement of workpieces during ramp up period for (a) ambient condition, (b) 50 ºC, (c) 100 ºC, and (d) 150 ºC.

5.4.3. Stress and Strain Distribution

The spatial distributions of the equivalent Mises plastic stress at the end of the simulation (at 0.2 sec) for different cases are presented in Fig. 5.9. The results show no obvious difference in stress distribution of all studied case. The tabs experience more plastic deformation in area than the bus-bar. The plastic deformed area in the bus-bar almost equals to the size of the anvil knurl, which indicates that the plastic deformation of the bus-bar is governed by the anvil. The stress concentration in the bus-bar is at the teeth of the knurls. With the bus-bar preheated, the stress at the tip of the knurl is slightly higher than that in the ambient condition. The higher plastic deformation allows stronger grip by the anvil on the bus-bar.

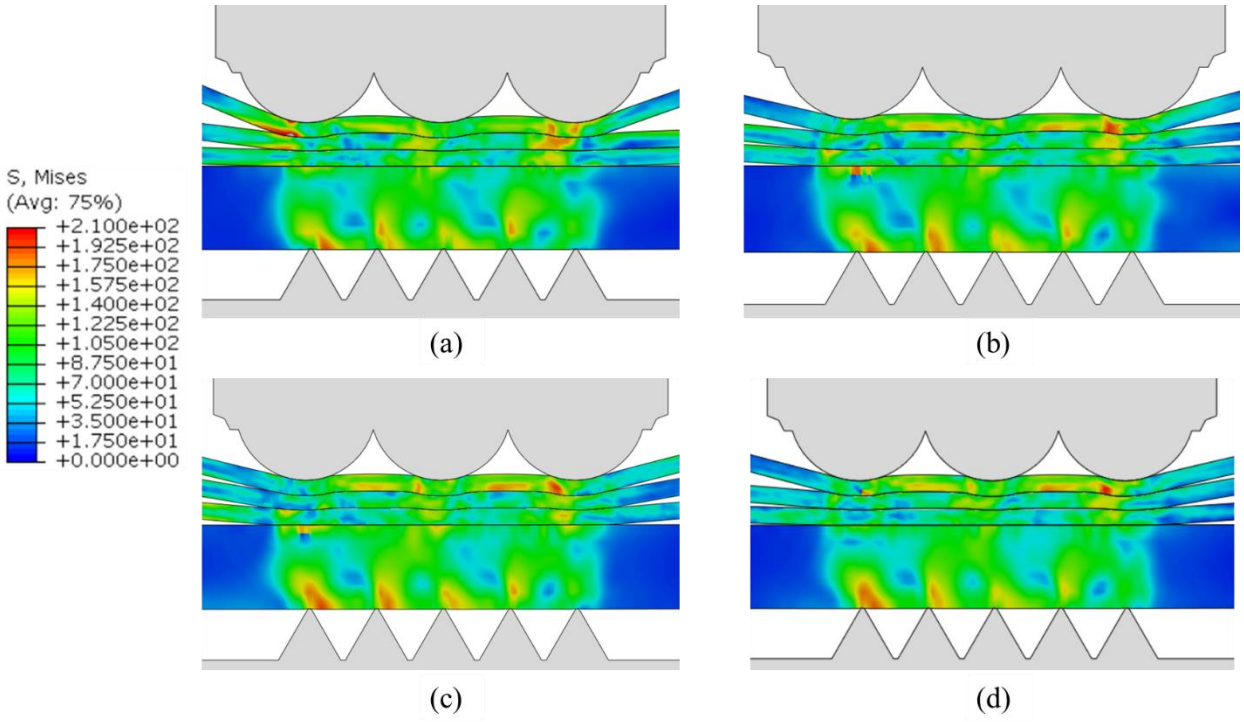

Figure 5.9. Equivalent plastic strain distribution for (a) ambient condition, (b) 50 ºC, (c) 100 ºC, and (d) 150 ºC.

The spatial distribution of the maximum principal strain are shown in Fig. 5.10. In all studied cases, strain concentrates at the area under the tips of the sonotrode knurl, and the

maximum strain concentrates in the 2nd tab. The higher strain in the 2nd tab allows the material to reach the flow stress earlier at the top and middle interface than that at the bottom interface. In the ambient condition, the strain in the 2nd tab is considerably higher than other preheating conditions. As preheating temperature increases, the strains in all tabs become more uniform as the strain in the 2nd tab decreases and strain in other tabs increases in both value and deformed area. The larger strain close to the bottom interface implies more deformation at the contacted area, allowing faster bond formation. Therefore, the weldability at the bottom interface is enhanced.

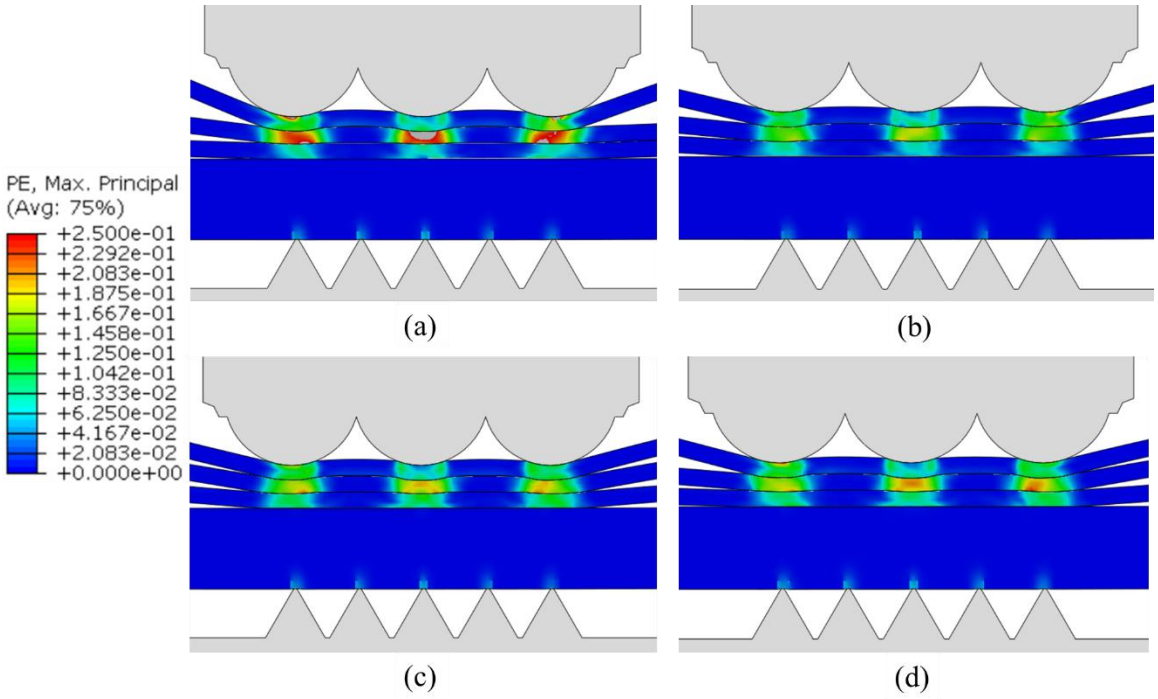

Figure 5.10. Maximum principal strain distribution for (a) ambient condition, (b) 50 ºC, (c) 100 ºC, and (d) 150 ºC.

5.4.4. Summary of the Simulation Results

In summary, the influence of localized preheating temperature was investigated with the simulation from three aspects: (a) temperature distribution, (b) workpiece relative motion, and

(c) stress and strain distribution. The results indicate that preheating leads to a more uniform temperature distribution, softens the material and allows larger relative motion at the bottom interface, and introduces more gripping from the anvil by material softening. However, the simulation only studied the earliest stages of the USW process before the weld forms. To investigate the influence of preheating temperature further, the simulation should be run for a longer process time.

5.5. Conclusion

This study investigates enhanced process robustness for four-layered Cu ultrasonic welds by localized preheating. The process was studied both experimentally and numerically. The bus-bar was preheated to specific temperatures before the welding process. The lap-shear load carrying capacity at the top and the bottom interface subjected to weld energy were measured and used as an index to show the influence of preheating temperature. Corresponding metallurgical features of the samples were analyzed to provide an additional explanation of the effect of preheating. Two-dimensional finite element models were built to numerically investigate the influence of preheating temperature and provide guidance for the selection of optimal and preheating temperature. The findings are as follows:

1) Preheating improves the bottom interface lap-shear strength, while it has little effect on the lap-shear strength of the top interface.

2) The benefit of preheating diminishes as weld energy increases.

3) An optimal preheating temperature maximizes the enhancement of the bottom interface strength.

4) Preheating improves weldability in multi-layered USW by expanding the required welding energy window to achieve satisfactory weld strength at the bottom interface while avoiding over-weld at the top interface.

5) Preheating influences the thermal-mechanical behavior at all interfaces and thus influences the weld formation in USW of 3CC.

References

[1] De Vries, E., 2004. Mechanics and mechanisms of ultrasonic metal welding (Doctoral dissertation, The Ohio State University).

[2] Das, A., Masters, I. and Williams, D., 2019. Process robustness and strength analysis of multi-layered dissimilar joints using ultrasonic metal welding. The International Journal of Advanced Manufacturing Technology, 101(1-4), pp.881-900.

[3] Elangovan, S., Prakasan, K. and Jaiganesh, V., 2010. Optimization of ultrasonic welding parameters for copper to copper joints using design of experiments. The International Journal of Advanced Manufacturing Technology, 51(1-4), pp.163-171.

[4] Neppiras, E.A., 1965. Ultrasonic welding of metals. Ultrasonics, 3(3), pp.128-135.

[5] Das, A., Li, D., Williams, D. and Greenwood, D., 2018. Joining technologies for automotive battery systems manufacturing. World Electric Vehicle Journal, 9(2), p.22.

[6] Lee, S.S., Kim, T.H., Hu, S.J., Cai, W.W., Abell, J.A. and Li, J., 2013. Characterization of joint quality in ultrasonic welding of battery tabs. Journal of Manufacturing Science and Engineering, 135(2), p.021004.

[7] Lee, S.S., Kim, T.H., Hu, S.J., Cai, W.W. and Abell, J.A., 2015. Analysis of weld formation in multilayer ultrasonic metal welding using high-speed images. Journal of Manufacturing Science and Engineering, 137(3), p.031016.

[8] Shin, H.S. and de Leon, M., 2017. Mechanical performance and electrical resistance of ultrasonic welded multiple Cu-Al layers. Journal of Materials Processing Technology, 241, pp.141-153.

[9] Siddiq, A. and Ghassemieh, E., 2008. Thermomechanical analyses of ultrasonic welding process using thermal and acoustic softening effects. Mechanics of Materials, 40(12), pp.982-1000.

[10] Elangovan, S., Semeer, S. and Prakasan, K., 2009. Temperature and stress distribution in ultrasonic metal welding—An FEA-based study. Journal of materials processing technology, 209(3), pp.1143-1150.

[11] Kim, W., Argento, A., Grima, A., Scholl, D. and Ward, S., 2011. Thermo-mechanical analysis of frictional heating in ultrasonic spot welding of aluminium plates. Proceedings

of the Institution of Mechanical Engineers, Part B: Journal of Engineering Manufacture, 225(7), pp.1093-1103.

[12] Zhang, C.S. and Li, L., 2009. A coupled thermal-mechanical analysis of ultrasonic bonding mechanism. Metallurgical and Materials Transactions B, 40(2), pp.196-207.

[13] Zhang, C.S. and Li, L., 2010. Effect of substrate dimensions on dynamics of ultrasonic consolidation. Ultrasonics, 50(8), pp.811-823.

[14] Lee, D., Kannatey-Asibu, E. and Cai, W., 2013. Ultrasonic welding simulations for multiple layers of lithium-ion battery tabs. Journal of Manufacturing Science and Engineering, 135(6).

[15] Lee, D. and Cai, W., 2017. The effect of horn knurl geometry on battery tab ultrasonic welding quality: 2D finite element simulations. Journal of Manufacturing Processes, 28, pp.428-441.

[16] Shen, N., Samanta, A., Ding, H. and Cai, W.W., 2016. Simulating microstructure evolution of battery tabs during ultrasonic welding. Journal of Manufacturing Processes, 23, pp.306-314.

[17] Li, H., Cao, B., Liu, J. and Yang, J., 2018. Modeling of high-power ultrasonic welding of Cu/Al joint. The International Journal of Advanced Manufacturing Technology, 97(1-4), pp.833-844.

[18] Li, H., Cao, B., Yang, J.W. and Liu, J., 2018. Modeling of resistance heat assisted ultrasonic welding of Cu-Al joint. Journal of Materials Processing Technology, 256, pp.121-130.

[19] Jedrasiak, P. and Shercliff, H.R., 2018. Finite element analysis of heat generation in dissimilar alloy ultrasonic welding. Materials & Design, 158, pp.184-197.

[20] Kannatey-Asibu Jr, E., 1991. Thermal aspects of the split-beam laser welding concept.

[21] Liu, Y.N. and Kannatey-Asibu Jr, E., 1993. Characteristics of elliptical laser beam preheating during laser welding. ASME PROD ENG DIV PUBL PED, ASME, NEW YORK, NY,(USA), 1993,, 64, pp.895-905.

[22] Rozzi, J.C., Pfefferkorn, F.E., Incropera, F.P. and Shin, Y.C., 1998. Transient thermal response of a rotating cylindrical silicon nitride workpiece subjected to a translating laser heat source, part I: comparison of surface temperature measurements with theoretical results.

[23] Özler, L., Inan, A. and Özel, C., 2001. Theoretical and experimental determination of tool life in hot machining of austenitic manganese steel. International Journal of Machine Tools and Manufacture, 41(2), pp.163-172.

[24] Dumitrescu, P., Koshy, P., Stenekes, J. and Elbestawi, M.A., 2006. High-power diode laser assisted hard turning of AISI D2 tool steel. International Journal of Machine Tools and Manufacture, 46(15), pp.2009-2016.

[25] Liu, X., Lan, S. and Ni, J., 2015. Thermal mechanical modeling of the plunge stage during friction-stir welding of dissimilar Al 6061 to TRIP 780 steel. Journal of manufacturing science and engineering, 137(5).

[26] Sharma, S.R., Ma, Z.Y. and Mishra, R.S., 2004. Effect of friction stir processing on fatigue behavior of A356 alloy. Scripta Materialia, 51(3), pp.237-241.

[27] Gunduz, I.E., Ando, T., Shattuck, E., Wong, P.Y. and Doumanidis, C.C., 2005. Enhanced diffusion and phase transformations during ultrasonic welding of zinc and aluminum. Scripta materialia, 52(9), pp.939-943.

[28] Yang, J. and Cao, B., 2015. Investigation of resistance heat assisted ultrasonic welding of 6061 aluminum alloys to pure copper. Materials & Design, 74, pp.19-24.

[29] Senouci, A., Zaidi, H., Frene, J., Bouchoucha, A. and Paulmier, D., 1999. Damage of surfaces in sliding electrical contact copper/steel. Applied surface science, 144, pp.287-291.

[30] Chaboche, J.L., 2008. A review of some plasticity and viscoplasticity constitutive theories. International journal of plasticity, 24(10), pp.1642-1693.

[31] Dassault Systems, 2013, "Abaqus Theory Manual (v.6.13)," Dassault Systems, Providence, RI.

[32] Hosford, W.F., 2010. Mechanical behavior of materials. Cambridge university press, pp. 79

[33] Johnson, G.R., 1985. Strength and fracture characteristics of a titanium alloy (. 06al,. 04v) subjected to various strains, strain rates, temperatures and pressures. Naval Surface Weapons Center NSWC TR, pp.86-144.

[34] Zhang, B. and Shim, V.P.W., 2010. Determination of inelastic heat fraction of OFHC copper through dynamic compression. International journal of impact engineering, 37(1), pp.50-68.

Chapter 6 Conclusions and Future Work

6.1. Conclusions

Ultrasonic welding (USW) is a favored process for battery tab joining because of its inherent advantages as a solid-state welding process effective for joining highly conductive and dissimilar materials. High battery quality and reliability requires the development of more robust welding processes and shorter process development times, especially for multi-layered weld configurations. However, limited understanding of the USW process hinders achieving consistent weld quality and process robustness. The goal of this study was to provide guidelines for improving the multi-layered ultrasonic welding process by developing a deeper understanding of the underlying physics in weld formation and the propagation of a weld in multi-layered USW. This research reveals an in-depth understanding of the multi-layered USW for similar and dissimilar materials, provides insights on how tool geometry and the interfacial weld attributes effect weld performance, and proposes a preheating method to enhance process robustness. The scientific understanding obtained from this dissertation will guide manufacturers in achieving a more robust and reliable ultrasonic welding process.

The major findings of this dissertation can be summarized in three parts:

1) *Weld formation in multi-layered ultrasonic welding of similar and dissimilar materials*

   The weld formations in 3-layered Al tabs to a Cu bus-bar (3AC) and a 3-layered Ni-coated Cu tabs to Ni-coated Cu bus-bar (3CC) were experimentally investigated. The bonding mechanisms between similar and dissimilar materials were studied using microscopy. The

evolution of the interfacial bonding and weld formation from interface to interface were related to the weld strength from lap-shear tests. The effects of process parameters were also discussed. The main conclusions are summarized as follows:

- The bonding between Ni-coated Cu sheets initiates with Ni-Ni bonding with minimum undulations, and develops into undulated Ni-Ni bonding lines as weld energy increases. With higher weld energy, the Ni-Ni bonding lines break down allowing Cu-Cu bonding. The broken Ni-Ni bonding lines distort to form mechanical interlocking and mix into base material.
- The weld propagates monotonically from the top interface to the bottom interface in USW in 3CC joints.
- The dominant bonding mechanisms among Al tabs in 3AC joints is metallic adhesion caused by dynamic recrystallization under severe plastic deformation. Bulk material mixture occurs if excessive weld energy is used.
- The bond formation between Al and Cu is governed by non-uniform interfacial diffusion enhanced by severe plastic deformation and elevated temperature. Intermetallic compounds (IMCs) can form under extreme plastic deformation.
- The weld forms sooner between Al-to-Al joints than that seen between Al-to-Cu joints, but there is insufficient evidence showing the weld formation sequence among Al tabs in the cases studied.
- Weld strength is most significantly affected by weld energy, then vibration amplitude, and is least sensitive to clamping pressure.

2) Influence of interfacial undulations on weld formation and performance

The effect of interfacial undulation on weld formation and performance was quantitatively investigated by using experiments with a fine and a coarse toothed anvil and with finite element modeling. A set of measurable weld attributes were introduced to characterize ultrasonic Al-to-Cu welds made by different anvils. The relationship between the weld attributes and their lap-shear performance was evaluated. A set of finite element models were developed to predict the interfacial bonding strength and quantitatively investigate the effect of interfacial undulations. The main conclusions are summarized as follows:

- A coarse anvil introduces more prominent interfacial undulations and thus sustains a greater post weld thickness at high weld energy. Therefore, higher lap-shear load carrying capacity with better robustness is achieved using the coarse anvil for welds made at higher weld energy.
- The interface bond density is not significantly affected by the anvil type, but the bonding strength is higher for samples made by a fine anvil in earlier stages of the process.
- Lap-shear load carrying capacity is positively affected by interfacial undulation when an interfacial failure mode is dominant, but negatively affected by interfacial undulation when the failure mode transitions to pull-out or circumferential failure.

3) Enhancement of process robustness in multi-layered ultrasonic welding by localized preheating

The effect of localized preheating on weldability and process robustness on multi-layered USW for four-layer Ni-coated Cu sheets was investigated. The enhancement of lap-shear performance at the bottom interface and the influence on the top interface over a range of weld

energies was evaluated. Two-dimensional finite element models were developed to investigate the thermal-mechanical performance during its initial 200 vibration cycles at three different preheating temperatures. The main conclusions are summarized as follows:

- Preheating improves the bottom interface strength, while it has little influence on the top interface strength.
- The effect of preheating on the bottom interface performance is most significant at lower energy levels and diminishes as weld energy increases.
- There is an optimal preheating temperature for the preheating process.
- Preheating improves weldability in multi-layered USW by expanding the required weld energy window to achieve a satisfactory weld strength at the bottom interface while avoiding an over-weld at the bottom interface. The process robustness is thereby improved.
- The optimal preheating temperature in this study was found to be 100 ºC. This temperature enabled the largest relative motion at the bottom interface without significantly sacrificing relative motion at the other interfaces.

The original contributions of this research can be summarized as follows:

1) An in-depth understanding of the bonding mechanisms for similar and dissimilar multi-layered USW has been developed. Joint propagation from interface to interface has been revealed. The improved understanding will provide guidance for further parameter optimization and process robustness enhancement. It can also help manufactures shorten the new process development time based on the guidance.
2) Quantitative relationship between interfacial undulation and the weld performance has been established. The relationship will help improve the design of the sonotrode tip and

anvil to improve the weld quality robustness. In addition, the study provides insights into weld formation and propagation in multi-layered USW where different levels of interfacial undulation co-exists at different interfaces.

3) Localized preheating is proposed as a good example of applying thermal assistance in a multi-layered USW process. It reveals that the process robustness can be enhanced by applying localized heat to a specified area.

6.2. Future Work

Multi-layered USW is a widely used technology in battery manufacturing, but continued improvement to the process by a deeper understanding and process optimization is still urgent. The following research extensions in the following directions are recommended:

1) *Multi-scale modeling of the USW process*: More sophisticated models can be developed to comprehensively predict weld formation during ultrasonic welding process, including atomic-level model for thermal dynamics of materials, micro-level for bonding mechanisms, and macro-level for thermal-mechanical performance. The model can be integrated with the weld performance simulation models to provide systematic analysis showing the relationship between process parameters and weld quality.
2) *Process monitoring with aid of neural network and deep learning technology*: The relationship between process inputs and the final weld quality, incorporated with intermediate process outputs, can be established by adopting new artificial intelligent technologies. Process input can include process parameters, material properties and geometries, and tool geometries. The intermediate outputs include

power history, weld time/energy for energy/time welding mode, and weld attributes. The weld quality may be measured by mechanical strength, electrical properties, or corrosion resistance. The relationship based on an integration of these various data can provide more precise guidance for process optimization.

3) *Innovative approach for process robustness enhancement*: Other innovative approaches, based on in-depth understanding of the multi-layered ultrasonic welding process, can be explored to enhance the process robustness. These approaches could include varying vibration amplitude, precise thermal assistance, or specifically designed weld configurations. The establishment of new method will help improve weld reliability and weldability.